UNIVERSITÁ DEGLI STUDI DI SALERNO

Dipartimento di Ingegneria dell'Informazione ed Elettrica e Matematica Applicata

UNIVERSITÁ DEGLI STUDI DI NAPOLI FEDERICO II

Dipartimento di Ingegneria Elettrica e delle Tecnologie dell'Informazione

DEGREE OF DOCTOR OF PHILOSOPHY IN PHOTOVOLTAICS

DOTTORATO DI INTERESSE NAZIONALE IN PHOTOVOLTAICS

CURRICULUM: MONITORING AND DIAGNOSIS

Design Strategies of Circuits for On-Field Monitoring and Characterization of Photovoltaic Modules

Supervisor:
Prof. Pierluigi Guerriero

PhD Program Director:
Prof. Giovanni Spagnuolo

PhD Candidate:
Monica De Riso
Mat. 8860800009

XXXVIII Cycle

2022 - 2025

Funded by the European Union

MUR
Ministero dell'Università e della Ricerca

Dottorato di Interesse Nazionale

PhD PV

Dottorato di Interesse Nazionale "PHOTOVOLTAICS"

Curricula:

- Solar cells technologies and lifecycle
- Design and integration
- Monitoring and diagnosis
- Power electronics and control
- Solar intermittency and storage
- Distributed generation and grid connection

A Vincenzo, Luca e i miei genitori.

Design Strategies of Circuits for On-Field Monitoring and Characterization of Photovoltaic Modules

Ph.D. Thesis presented
for the fulfillment of the Degree of Doctor of Philosophy
in Photovoltaics
by

Monica De Riso

November 2025

Approved as to style and content by

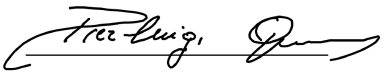

Prof. Pierluigi Guerriero, Advisor

Università degli studi di Salerno
Ph.D. Program in Photovoltaics
XXXVIII cycle - Chairman: Prof. Giovanni Spagnuolo

https://corsi.unisa.it/photovoltaics/en/home

Candidate's declaration

I hereby declare that this thesis submitted to obtain the academic degree of Philosophiæ Doctor (Ph.D.) in Photovoltaics is my own unaided work, that I have not used other than the sources indicated, and that all direct and indirect sources are acknowledged as references.
Parts of this dissertation have been published in international journals and/or conference articles (see list of the author's publications at the end of the thesis).

Napoli, November 3, 2025

Monica De Riso

Abstract

Effective monitoring and diagnostic strategies are fundamental to ensuring optimal operation and long-term reliability of photovoltaic systems. Electric monitoring methods, in particular current-voltage curve tracing and impedance spectroscopy, allow to accurately assess the performance and state of degradation of photovoltaic systems. However, state-of-the-art approaches based on module-level monitoring suffer from several limitations. Conventional current-voltage curve tracers require the shutdown of the photovoltaic plant and a long and costly string disassembly, negatively impacting the return on investment. Conversely, solutions based on impedance spectroscopy rely on bulky and expensive laboratory-grade instruments, confining this technique to indoor characterizations and hindering its applicability on-field.

This research aims to overcome these limitations by developing enhanced embedded electronic circuits capable of performing on-field and on-line electric measurements at the module level. The core objective is the design and realization of compact, low-cost hardware solutions that enable current–voltage curve tracing and impedance spectroscopy measurements under real operating conditions. Two complementary circuit topologies have been proposed and validated: a linear circuit based on bipolar junction transistors, allowing accurate current-voltage curve sweeping, and a switch-mode converter topology equipped with an energy storage system, enabling on-field impedance measurements across a wide range of frequencies.

The research further explores the modeling of both static and dynamic electrical behavior of photovoltaic modules. A detailed DC model has been formulated to reproduce current-voltage characteristics under varying irradiance and temperature conditions, with particular emphasis on bifacial technologies. The tool incorporates a novel irradiance modeling approach based on view factor analysis to account for albedo-induced mismatch losses. Additionally, a dynamic equivalent circuit model has been developed to interpret impedance data, capturing the frequency-dependent response of photovoltaic modules and enabling accurate fault identification.

Overall, this work contributes to the advancement of module-level monitoring and diagnostic methodologies by integrating innovative design strategies of

circuits with improved modeling tools.

Keywords: photovoltaic, monitoring and diagnosis, current-voltage curve tracing, impedance spectroscopy, DC model, bifacial modules, dynamic model

Sintesi in lingua italiana

Le strategie di monitoraggio e diagnostica sono fondamentali per garantire il funzionamento ottimale e l'affidabilità a lungo termine dei sistemi fotovoltaici. Le tecniche di monitoraggio di tipo elettrico, in particolare il tracciamento della caratteristica corrente-tensione e la spettroscopia di impedenza, consentono di valutare le prestazioni e lo stato di degradazione dei sistemi fotovoltaici. Tuttavia, gli approcci allo stato dell'arte basati sul monitoraggio a livello di modulo presentano ancora svariate limitazioni. I tracciatori di caratteristiche corrente-tensione convenzionali richiedono lo spegnimento dell'impianto fotovoltaico e un lungo e costoso smontaggio della stringa, causando un impatto negativo sulla redditività operativa. Al contrario, le soluzioni basate sulla spettroscopia di impedenza richiedono l'uso di ingombranti e costosi strumenti da laboratorio che ostacolano l'applicazione di tale tecnica sul campo. L'attività di ricerca svolta si propone di superare tali limitazioni attraverso lo sviluppo di circuiti elettronici avanzati in grado di eseguire misure elettriche sul campo a livello di modulo durante il funzionamento normale dell'impianto fotovoltaico. L'obiettivo principale è la progettazione e la realizzazione di soluzioni hardware compatte e a basso costo, capaci di effettuare il tracciamento della curva corrente-tensione e implementare la tecnica di spettroscopia di impedenza in condizioni operative reali. Sono state proposte e validate due topologie circuitali complementari: un circuito lineare basato su transistori bipolari per il tracciamento della curva corrente-tensione, e un circuito basato sulla topologia di convertitore a commutazione dotato di un sistema di accumulo energetico, che permette l'esecuzione di misure di impedenza in campo su un ampio intervallo di frequenze.

La ricerca approfondisce inoltre la modellazione del comportamento elettrico statico e dinamico dei moduli fotovoltaici. È stato sviluppato un modello in corrente continua in grado di riprodurre le caratteristiche corrente-tensione al variare dell'irradianza e della temperatura, con particolare attenzione alle tecnologie bifacciali. Lo strumento integra un innovativo approccio di modellazione dell'irradianza basato sull'analisi dei fattori di vista, per modellare le perdite da mismatch indotte dall'albedo. Inoltre, è stato elaborato un modello circuitale dinamico per l'interpretazione dei dati di impedenza, capace di descrivere la risposta in frequenza dei moduli fotovoltaici e consentire l'identificazione accu-

rata dei guasti.

Nel complesso, questo lavoro contribuisce all'avanzamento delle metodologie di monitoraggio e diagnostica a livello di modulo, integrando lo sviluppo di soluzioni hardware con strategie di modellazione avanzati.

Parole chiave: fotovoltaico, monitoraggio e diagnosi, tracciamento della curva corrente-tensione, spettroscopia di impedenza, modello dc, moduli bifacciali, modello dinamico

Contents

Acknowledgements

The author's work has been carried out in the framework of the PRIN (Progetti di Rilevante Interesse Nazionale) 2020 project "A Holistic Monitoring and Diagnostic Tool for Photovoltaic Generators (HOTSPHOT)" (Prot. 2020LB9TBC) and PRIN 2022 project "Enhanced Device for Online diagnosis of Photovoltaic and Storage Systems (DOGPHOSS)" (Prot. P20229FWZK) .

List of Acronyms and Symbols

The following acronyms and symbols are used throughout the thesis.

PV	Photovoltaic
EL	Electroluminescence
IR	Infrared
IRT	Infrared Thermography
IS	Impedance Spectroscopy
I–V	Current–Voltage
P–V	Power–Voltage
IVT	Current-Voltage curve Tracing
LID	Light Induced Degradation
PID	Potential Induced Degradation
UV	Ultraviolet
DC	Direct Current
AC	Alternate Current
c–Si	crystalline Silicon
UAV	Unmanned Aerial Vehichle

PR	Performance Ratio
STC	standard Test Condition
CCD	Charge-Coupled Device
MPP	Maximum Power Point
MPPT	Maximum Power Point Tracking
OP	Operating Point
I_{SC}	Short Circuit Current
V_{OC}	Open Circuit Voltage
PLA	Power Loss Analysis
IoT	Internet of Thing
ROI	Return on Investment
BJT	Bipolar Junction Transistor
TCAD	Technology Computer Aided Design
SAPM	Sandia Array Performance Model
SDM	Single Diode Mode
DDM	Double Diode Mode
3D	three-dimensional
2D	two-dimensional
RC-loop	parallel resistor-capacitor circuit
CPE	Constant Phase Element
BSF	Back Surface Field
ARC	Anti-Reflective Coating
RMSE	Root Mean Square Error
DAQ	Data Acquisition System

GUI	graphic user interface
DAC	digital to analogue converter
ADC	analogue to digital converter
PCB	printed circuit board
MCU	microcontroller
IC	integrated circuit
SNR	signal-to-noise ratio
RSD	relative standard deviation
ME	mean error value
poly–Si	Poly-crystalline Silicon
a–Si	Amorphous Silicon
HJT	Hetero-junction with Intrinsic Thin layer
mono–Si	mono-crystalline Silicon
PWM	Pulse Width Modulation
PI	Proportional-Integral
GaN	Gallium Nitride
TMR	Tunneling-Magneto Resistive

List of Figures

List of Tables

Chapter 1

Introduction

1.1 Background and Motivations

The global energy landscape has been undergoing a significant transformation in recent decades, with increasing emphasis on renewable energy sources to mitigate environmental impacts and reduce dependence on fossil fuels. Among various renewable technologies, PV systems have gained considerable traction due to their scalability, decreasing cost and adaptability to various environments. One prominent example of this trend is the ambitious solar energy strategy adopted by the European Commission in May 2022. This strategy reflects the European Union's commitment to achieving a greener energy future by setting a bold target of delivering 320 GW of newly installed PV capacity by 2025 and nearly doubling that figure to 600 GW by 2030 [12]. The rapid expansion of PV installations, from residential rooftops to large-scale solar farms, underscores the need for efficient monitoring and diagnostic tools to ensure optimal performance, reliability, and long-term durability of PV modules. Since PV systems are expected to operate outdoors, PV modules are subjected to degradation and aging phenomena, impacting their performance and efficiency over time. Common drivers are the prolonged exposure to environmental stresses, such as temperature fluctuations, Ultraviolet (UV) radiation and atmospheric pollutants. The estimated degradation rate is indeed found to vary between -0.8% and -4.9% per year, depending on the location of the PV system [13]. For instance, in many climate zones, the long-term

accumulation of dirt and debris on the modules can significantly degrade their performance. Indeed, drier climates leave significant deposits of dirt, so mechanical cleaning is necessary to maintain optimal performance [14]. This problem is not as noticeable in regions with significant rainfall because rain tends to clean the solar modules. Timely detection of faults allows for improved safety and prompt repairs, reducing maintenance costs and preventing more extensive damage that could incur higher expenses. Additionally, regular monitoring can extend the lifespan of the PV system by ensuring that all components function correctly.
Since PV is a scalable technology, the PV modules are connected in series or parallel configuration to build large power installation. Therefore, any fault or mismatch conditions among the modules negatively affect the efficiency of the overall PV system. In other words, the PV system is only as efficient as its weakest component. To this aim, central to the operation of PV systems is the ability to monitor and assess the performance at the module level. Monitoring techniques for PV systems can be broadly classified into those based on visual and imaging inspection, and those based on electric methods, consisting of measuring the voltage and current of the module under test. This latter relies on a model-based approach consisting of diagnosing the state of health of PV modules through the extraction of the equivalent model's parameters. With respect to imaging methods, electric approaches offer a more precise classification of the degradation mechanisms and quantification of the corresponding energy loss. However, a challenging issue associated with electric methods is the need to perform the measurements at the terminals of the PV module by using hardware that neither affects the PV power production nor incurs in significant cost compared to the PV module. Most diagnostic instruments available on the market are designed for string-level analysis. When employed to monitor individual modules, the accuracy of those instruments degrades because they are conceived for larger voltage range, typically up to 1000 V. Moreover, their high cost and operational constraints make them unsuitable for frequent and continuous deployment in the field. In response to these limitations, significant research efforts have been devoted to the development of low-cost hardware solutions capable of measuring voltage and current at the PV module level. Many of these designs exploit low-cost microcontrollers and sensors, often declined to Internet of Thing (IoT) applications.

For instance, [15] and [16] proposed a monitoring system based on a low-cost Arduino acquisition board, demonstrating a measurement accuracy comparable to that of laboratory-grade multimeters. However, the main limitation lies in the need for an external electronic load to span the I–V curve. Conversely, [17] presented an instrument capable of measuring I–V characteristics at string level using a LabVIEW interface combined with a mosfet-based electronic load, thereby enabling dynamic control of the operating point. Similarly, [18] developed a monitoring system employing an ATmega microcontroller and a Visual Basic interface for data acquisition and visualization. Although these approaches successfully demonstrate the feasibility of low-cost measurement hardware, they all share a common limitation: the need for the temporary shutdown of the PV plant and the disassembly of the string to perform measurements. These operational interruptions significantly impact energy production and reduce the overall Return on Investment (ROI).

Beyond diagnostic purposes, the electric DC modeling of PV modules is also fundamental for energy estimation and performance forecasting. The most common DC models describe the static I–V characteristics of the module under given irradiance and temperature conditions. These models are extensively used in both research and industry to predict energy yield and identify degradation signatures. However, accurately reproducing the I–V curve across diverse environmental and operational conditions remains a challenging task, particularly when dealing with bifacial technology. Bifacial PV modules harness irradiance not only from the front side but also from the rear, by capturing the diffused and reflected light from the ground. Consequently, accurately modeling the rear-side irradiance is essential for reliable energy and electrical performance prediction. State-of-the-art modeling approaches based on view factor method compute the irradiance as an average quantity throughout the module surface, thereby assuming a uniform irradiance distribution across all cells. An example of this approach can be found in [19], where the authors developed a model for simulating the PV power output of bifacial modules presenting an analytical equation for the computation of the rear albedo solely depending on module tilt angle. A similar approach is then adopted in [20] and later improved in [3], which corrects a theoretical flaw by including the dependence of the sky dome portion seen from the self-shaded ground. The

assumption of uniform irradiance distribution on the module's surface can be considered acceptable for monofacial technology because the contribution of ground albedo represents only a minor fraction of the total absorbed light, whereas it becomes inadequate for bifacial one because albedo constitutes the dominant component of the rear-side irradiance. Indeed, the albedo irradiance absorbed by each cell depends strongly on the module tilt, their distance from ground and their relative position with respect to module shadow. As a result, cell-to-cell irradiance nonuniformity can occur within the same module, giving rise to albedo-induced mismatch losses [21], which should be accounted for to achieve accurate energy estimation and reliable diagnostic analysis.

Recently, IS has emerged as a promising alternative electrical technique for assessing the health and performance of PV modules. Unlike traditional Current-Voltage curve Tracing (IVT), IS provides frequency-domain information about the dynamic behavior of the device, enabling the identification of degradation mechanisms that are not evident in static I–V measurements [22]. Through the analysis of the equivalent parameters derived from the impedance spectrum, IS has proven effective in identifying localized defects. As an example, [23] discovers that interconnect ribbon disconnections increase series resistance and reduce parallel resistance. Conversely, cell cracking significantly reduces the time constant, reflecting higher minority carrier recombination rates. A similar approach is adopted by [24], demonstrating the efficacy of detecting cracks and soiling through the integration of IS with machine learning schemes. Despite its potential, IS cannot yet be considered a fully established technique for PV monitoring and diagnostics, as its application remains largely confined to laboratory environments. Consequently, two major limitations currently hinder its widespread industrial adoption: the lack of portable and embedded instrumentation capable of performing on-field impedance measurements at the module level; and the absence of well-established equivalent circuit models that accurately capture the dynamic behavior of PV modules across a wide frequency range and under varying operating conditions.

Based on the challenges and research gaps highlighted above, I identified two main research directions, that constitute the foundation of this work.

i The first concerns the design and development of embedded elec-

tronic circuits capable of enabling on-line IVT and IS measurements directly on-field, thus allowing continuous and non-intrusive monitoring of PV modules.

ii The second focuses on the study and formulation of improved static and dynamic models for the accurate electrical characterization of PV modules, both for diagnostic purposes and energy estimation. Particular attention is devoted to extending these models to bifacial technologies, which are currently attracting increasing interest from the PV industry.

1.2 Research Objectives

The work presented in this dissertation aims to contribute to the advancement of module-level monitoring and diagnostic techniques for PV systems by addressing both hardware design and modeling aspects. The primary objective is the design and realization of innovative embedded electronic circuits capable of implementing two complementary electrical monitoring techniques, IVT and IS, for on-field applications. A key requirement of this research is the development of low-cost hardware that enables on-line measurements, meaning that the measurement can be performed during normal string operation without the need for plant shutdown and manual string disassembly. As a result, monitoring costs are significantly reduced because the proposed approach guarantees continuous energy production, thereby improving the overall ROI of the PV installation. To achieve this goal, two distinct circuit topologies have been investigated.

i A linear circuit based on BJTs, designed to enable controlled biasing of the PV module and precise characterization thanks to the capability of evenly distributing the operating points throughout the I–V curve, even under partial shading conditions. This feature, in particular, allows the proposed circuit to outperform standard commercial devices in terms of metrological accuracy, resolution and time duration.

ii A switching converter topology equipped with an energy storage system has been developed to bias the PV module and inject the perturbations required for performing IS measurements. Compared to

other solutions reported in the literature, this design is fully integrated and self-sufficient, providing a complete platform for on-field impedance measurements. The converter is specifically designed to operate under outdoor conditions and can perform measurements up to 50 kHz.

From a technological standpoint, in summary, this research addresses the lack of cost-effective and compact instrumentation for performing electric diagnosis directly at the module level.
In parallel with hardware design, this work focuses on the study and formulation of improved static and dynamic models for the accurate electrical characterization of PV modules. The first aspect involves the DC electrical behavior of PV modules through the development of a simulation tool capable of reproducing I–V characteristics under varying environmental conditions. The tool is optimized for bifacial modules, accounting for albedo-induced mismatch losses through a novel cell-level irradiance model based on view factor calculations. This approach enables more accurate prediction of electrical performance, addressing limitations inherent to state-of-the-art view factor-based approaches. The research further addresses dynamic modeling aimed at fault identification and diagnostic applications. Dynamic models are developed to describe the Alternate Current (AC) behavior of PV modules, allowing an accurate parameters' extraction procedure from experimental IS data. This research is devoted to perform a comprehensive analysis of the dynamic response of standard c–Si modules using simulation environments, leading to the definition of an equivalent circuit model that accurately represents the module's behavior under real operating conditions.

1.3 Thesis outline

This dissertation is organized into five chapters. The remainder of this work is structured as follows. Chapter 2 provides a comprehensive overview of monitoring techniques for the diagnosis and characterization of PV system. It sets the context and establishes the groundwork for the research approaches and methodologies presented in the subsequent chapters. It begins with a classification of faults and degradation mechanisms that affect long-term PV reliability. The chapter outlines the requirements for an

effective monitoring strategy and reviews the state-of-the-art approaches, divided into imaging and electric methods. Particular emphasis is placed on IVT and IS, which represent the techniques explored in this thesis. The chapter provides an extensive literature analysis to underline the advantages and limitations of existing methods, motivating the need for a hybrid monitoring strategy that combines imaging inspection with electrical measurements at the module level. Chapter 3 focuses on the modeling of PV modules, aiming to accurately describe the static and dynamic electrical behavior for fault diagnosis and energy prediction purposes. It first introduces conventional DC models used to represent the static I–V characteristics and subsequently presents an *innovative circuit-based tool embedding a cell-level irradiance model for bifacial modules*, which improves the accuracy of energy prediction by accounting for albedo-induced mismatch losses. The analysis then extends to *dynamic models* capable of describing the frequency-dependent response of PV modules. Chapter 4 presents the design and development of a *portable wireless I–V curve tracer* specifically tailored for module-level monitoring. The proposed I–V tracer incorporates a variable load based on a linear circuit topology and an innovative disconnecting circuit that enables on-line I–V curve measurements without interrupting the normal operation of the PV string. The chapter provides a comprehensive description of the methodology adopted for the design of both the hardware and the control algorithm. The performance of the proposed I–V tracer is validated through extensive indoor and outdoor tests and benchmarked against a commercial instrument. Chapter 5 is devoted to the design and validation of a *switched-mode impedance analyzer* for on-field IS measurements of PV modules. The chapter discusses the main design challenges associated with converter-based impedance analyzers, including the accuracy of small-signal excitation injection, the impact of switching ripple and system's dynamics on the IS procedure. The developed prototype is experimentally validated through outdoor tests. The chapter concludes with a discussion of the main challenges encountered during development and outlines future directions. Finally, in Chapter 6, the conclusions are drawn.

Chapter 2

Monitoring Techniques for Diagnosis and Characterization

2.1 Introduction

The long-term reliability of PV systems is significantly affected by faults and degradation mechanisms that occur during operation. When exposed to outdoor conditions, PV modules experience numerous electrical, mechanical, and environmental stress factors that can progressively reduce efficiency or cause complete failure. Therefore, effective monitoring, diagnosis, and characterization of PV modules have become essential to ensure optimal energy yield and prevent unexpected outages. This chapter provides an overview of monitoring techniques for the diagnosis and characterization of PV modules. It begins with a classification of the main PV faults followed by a discussion of the requirements for an effective monitoring system. Subsequently, the chapter presents a comprehensive review of the widely adopted monitoring approaches, which can be grouped into two main categories:

- Imaging-based techniques, such as visual inspection, IRT and EL, primarily used to detect and localize physical defects;
- Electrical-based techniques, which rely on the module's electrical re-

sponse, including IVT and IS, to assess performance and identify degradation mechanisms.;

Through an extensive literature review, the chapter analyzes the operating principles, advantages, and limitations of these state-of-the-art approaches. Emphasis is placed on I–V curve analysis and IS, which represent the core diagnostic tools explored in this thesis. Finally, the chapter introduces the motivation for developing a hybrid monitoring strategy that combines imaging inspection with module-level electrical characterization, aiming to overcome the limitations of existing methods and provide a more complete and reliable diagnostic framework. The insights gained from this literature review form the foundation for the research activities presented in the following chapters, which focus on the development of enhanced circuit designs for on-field and on-line monitoring of PV modules.

2.2 Overview of faults in photovoltaic modules

PV systems may experience a range of faults affecting components belonging either on the DC or AC sides of the PV system [25]. DC side faults affect PV modules, cables, switches, bypass diodes and DC-DC converters. On the AC side, faults consist of grid outage and total blackout, often caused by inverter damage and lighting events. This section classify the faults affecting the performance of PV modules and also outlines the key requirements for an ideal monitoring approach.

2.2.1 Photovoltaic faults classification

PV faults can be broadly defined as malfunctions or defects that (i) degrade the module power output or (ii) comprise the operational safety of the PV system. PV faults are generally categorized into three temporal classes: infant failures, midlife failures and wear-out-failures. Infant failures occur in the early stages of a PV module's operating life. They are often attributed to manufacturing defects and improper handling during installation. Since flawed PV modules fail quickly, they dramatically impact on the costs of the module manufacturer and installer because they are responsible for replacement under warranty. Examples of infant failures include glass breakage, frame detachment and contact failure in the string

interconnection. Another common failure occurring right after installation is the Light Induced Degradation (LID), a phenomenon that causes a drop in the relative efficiency of 4%-6% [26] in c–Si modules when exposed to sunlight. Midlife failures appear during the normal operation of the module and are usually linked to environmental stresses, such as temperature fluctuations, humidity, UV radiation and harsh weather conditions (*i.e.,* snow and hailstorms). Finally, wear-out failures are those occurring at the end of the working lifetime of PV modules, ideally beyond the warranty period. In reality, the end of the useful life is often defined as the point at which the PV power drops below 70%-80% of the initial nominal rating [27], and it is estimated that approximately 21% of the installed modules reach the end of their useful life before the manufacturer's warranty [28]. A detailed classification of the common PV faults occurring in the life cycle of a PV module is shown in Figure 2.1.

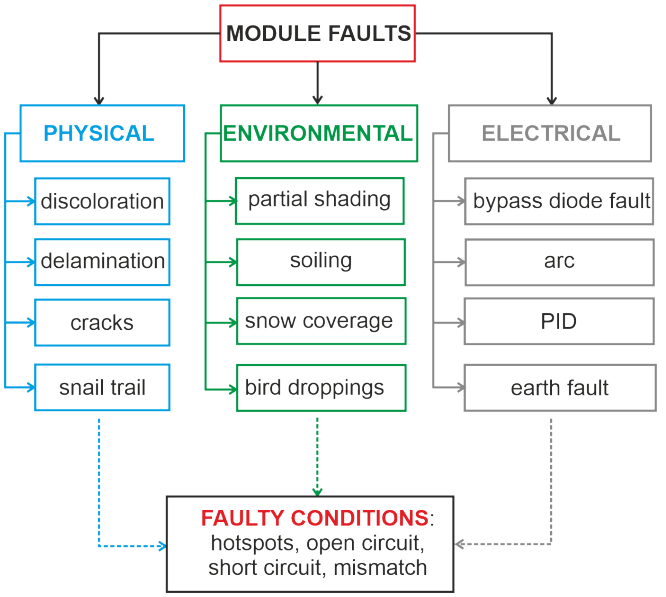

Figure 2.1. Classification of module faults based on their nature. Physical faults are depicted in blue, environmental faults are indicated in green whereas electrical faults are sketched in grey. The resulting faulty conditions are also reported.

PV faults can also be classified according to their severity. Electrical faults that cause short- and open circuit conditions are called acute as they abruptly disrupt the module operation, leading to complete and permanent shutdown. Other examples of acute and permanent faults are those affecting the material and internal structure of the PV module (*i.e.,* physical faults) such as cracks and micro-cracks. They may occur during module manufacturing, handling, and transportation or after harsh weather conditions because they are the result of mechanical strain and heat-induced stress. Cracks can significantly reduce power output due to the formation of inactive cell area [29]. On the other hand, environmental faults, such as partial shadings, are called chronic faults because they are temporary and the effect is often reversible. Partial shading, for istance, occur when objects cast shadows on the PV module. In this case, the solar irradiance incident on the module surface is not uniform, causing the shaded cells to limit the overall output current since the series connection of the module forces all the cells to operate with the same current. The excess power generated by the unshaded cells is dissipated in the shaded cells, which are forced into reverse bias operation. The reverse-bias operation generally occurs whenever the cells within a module operate under different operating conditions, *i.e.,* mismatched cells. If the reverse bias exceeds the cell breakdown voltage, the affected cell experiences a thermal breakdown that leads to the formation of hotspots, localized regions of elevated temperature that may exceed 100°C. Hotspots not only accelerate material degradation but can also cause irreversible structural damage and, in extreme scenarios, pose fire risks. Prompt detection and resolution of PV faults is essential both to mitigate the long-term impact of temporary faults and to prevent permanent damage. To this end, the development of efficient and cost-effective monitoring and diagnosis techniques is of paramount importance.

2.2.2 Monitoring techniques

An effective monitoring and diagnostic strategy should be able to guarantee the following features: (i) *fault detection*, (ii) *fault localization*, (iii) *fault classification*, and (iv) *energy loss quantification*. Traditional monitoring methods can be classified in those based on imaging solutions and those based on the acquisition of electrical quantities [30]. Methods based on imaging solutions guarantee (i)-(iii), even though a precise fault clas-

sification strongly depends on the camera setup, such as shot angle and its distance from the PV module [31], and weather conditions, *i.e.,* air temperature and humidity [32]. Unfortunately, imaging methods cannot quantify the energy loss and not all of them are suitable for on field and real-time monitoring. Better results can be achieved with electric methods. These latter are model-based approaches which generally use an analytical model to extract both DC electrical and physical parameters of the PV system. By monitoring those parameters, various malfunctions can be identified. An extensive discussion on PV models is provided in Chapter 3. The electric methods can be also classified depending on the "level of granularity" [33]. "Low granularity" methods are performed at string, array and sub-plant level, thus allowing a quick and low-cost estimation of the power losses. Nevertheless, "low granularity" methods cannot identify the location of the fault, especially in medium/high power plants where the number of modules can rise to many thousands. A "high granularity" method can tackle this issue because it consists of monitoring individual PV modules within a string.

2.3 Imaging Techniques

Image-based monitoring techniques are versatile approaches for the assessment of PV modules. By employing tools such as digital cameras, drones and UAVs, these techniques can capture detailed visual and thermal data from PV modules under real operating conditions. The captured image can then be analyzed to detect surface anomalies, hot spots, shading effects, and early signs of material degradation. In the scientific literature, three main approaches have been widely reported, namely visual inspection and visible image acquisition, IRT and EL. In the following subsections, an extensive overview of the above-mentioned techniques is given.

2.3.1 Visual inspection and visible image acquisition

Visual inspection method is the most straightforward and cost-effective method to find defects in a PV module. As non-invasive approach, it provides direct evidence of anomalies often visible on the module surface such as glass breakage, delamination, surface soiling and encapsulant browning

[34]. Figure 2.2 shows different faulty PV modules available at the Department of Electric Engineering and Information Technologies, namely affected by glass breakage (see Figure 2.2a) and encapsulant browning (see Figure 2.2b).

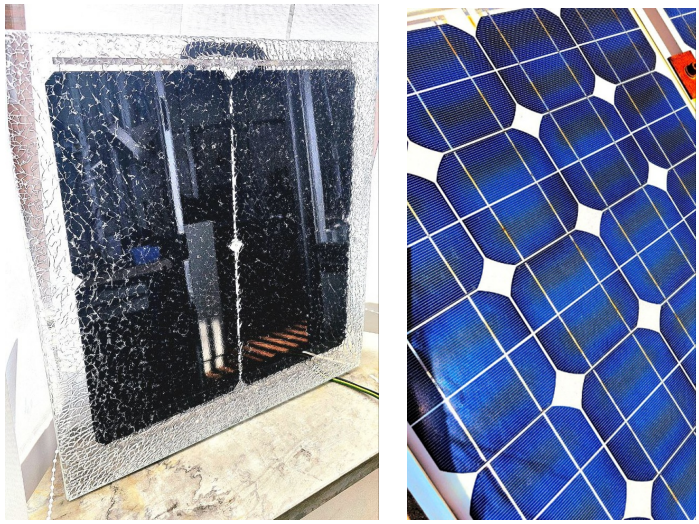

(a) **(b)**

Figure 2.2. Types of faults detectable through visual inspections and visible image acquisition: **(a)** glass breakage, **(b)** encapsulant browning.

The visual inspection method is formally integrated into international testing standards, such as IEC 61215 [35] and IEC 61646 [36], where inspection is performed before and after a group of 8 identical modules have undergone accelerated aging tests. These tests include thermal cycling, humidity-freeze cycling, damp heat exposure, UV irradiation and hail impact. In this context, the standards require an illumination of more than 1000 lux during the inspection and only defects detectable with the bare eye are considered, such as bubble formation, backsheet cracking and junction box detachment [27]. In on-field applications, visual inspection is performed manually by operators walking along PV rows. Since this approach is time consuming, especially for utility-scale solar farms, UAVs equipped with high resolution cameras are increasingly employed. UAV imaging

platforms [37, 38, 39] allow for programmed regular inspections, thereby creating time-series datasets that can be used for degradation trend analysis. However, it must be highlighted that UAVs are very expensive, thereby increasing the cost of the operation and maintenance, and cannot be used in extreme weather conditions, which often results in blurry images.

2.3.2 Infrared Thermography

IRT is a contactless technique that exploits the infrared radiation emitted by the module surface to map the temperature distribution across PV cells and interconnections. The working temperature of a cell is the result of a power balance, in which the input solar power is partitioned in three contributions: the electrical power generated by the cell, the thermal power associated to the heat flux moving horizontally between adjacent cells and the thermal power associated with the heat flux moving vertically between cells and the ambient [40]. Under uniform operating conditions, cells within a module share similar power balances, resulting in a relatively uniform temperature distribution across the module surface. In presence of mismatch, however, the power balance is altered giving rise to local temperature rises. As a result, the temperature distribution across the module surface is non-uniform. IR provides a direct means to reconstruct the thermal map of the PV module, where hotspots, shunts, soldering failures and faulty bypass diode appear as temperature anomalies. An illustrative example of a thermal image is reported in Figure 2.3. The image was acquired using FLIR E96 [41] thermal camera on roof-mounted PV modules installed at the Laboratory of Photovoltaics, University of York. Figure 2.3 reveals the presence of hotspot, with the cell working at elevated temperature (*i.e.*, above 100°C).

Along with visual inspection, a significant advantage of IRT is its compatibility with in-situ and on-line monitoring. Unlike laboratory-based techniques that require module disassembly and special biasing conditions, IRT can be performed during normal operation of the PV system under natural sunlight. Furthermore, when mounted on UAVs, IR cameras enable the rapid inspection of large-scale solar farms [42, 43] and roof-mounted PV systems with limited access [44, 45]. This scalability has made IRT one of the most widely adopted field diagnostic tools for large PV plants, where manual module-by-module inspection would be imprac-

Figure 2.3. IRT image using FLIR E96 for hotspot detection on roof-mounted PV modules installed at the Laboratory of Photovoltaics, University of York, York, U.K.

tical. Despite its strengths, IRT shows some limitations. The accuracy of the thermal map strongly depends on environmental conditions such as irradiance, wind speed, and ambient temperature, which can influence the measured surface temperatures. Direct sunlight may affect the quality of images due to glare from the sun, causing measurement errors [31]. In addition, IRT imaging provides only indirect evidence of defects; it identifies thermal symptoms but not always the root cause of the anomaly. For instance, a hotspot may arise from different causes such as partial shading and microcracks. Since these faults produce similar thermal signature, IRT cannot unambiguously identify their origin, and consequently a complementary diagnostic method must be employed.

2.3.3 Electroluminescence

EL exploits the radiative interband recombination of excited charge carriers in solar cells for investigating electrical inhomogeneities caused by intrinsic defects, such as grain boundaries and shunts, and extrinsic defects such as cell cracks and corrosion. Compared to visible and infrared

imaging, EL imaging provides a much finer diagnostic resolution and can reveal defects that are otherwise invisible [31]. During EL test, the solar cell operates in a dark environment as a light emitting diode supplied by an external excitation current. A typical EL setup is schematized in Figure 2.4.

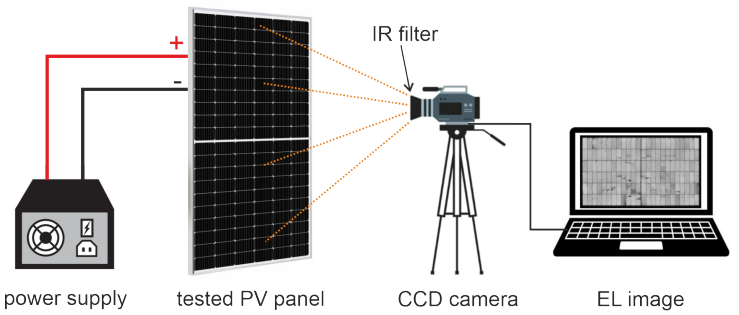

Figure 2.4. Schematic representation of a typical EL setup. During EL image acquisition, the PV module is biased by a DC power supply under completely dark conditions. The CCD camera must be equipped with a specific IR sensor to properly capture the light emissions from the tested module. Reproduced from my own work [1].

An EL test begins with the PV module subjected to an electric bias provided by a suitable DC power supply under completely dark conditions. Since the semiconductor materials of the PV cells have emission spectra in the IR region of the electromagnetic spectrum (in the range 900–1300 nm) rather than the visible one, a professional CCD camera is equipped with a specific IR sensor to capture the resulting light emissions. EL images detail insights into the internal structure of the module and enable accurate defects identification. The primary application of EL is the detection of cracks [46, 47]. Figure 2.5 shows the EL image of a c–Si PV modules tested at the Laboratory of Photovoltaics, University of York. The module was subjected to mechanical load before the test. The EL image is obtained biasing the PV module with a DC current 10% above its I_{SC}. The dark area indicates inactive area, meaning that the cell does not generate photo-current when exposed to sunlight. The presence of inactive areas and micro-cracks dramatically reduces the power output. Despite being an accurate tool for the detection of localized cracks, EL is only suitable for

laboratory diagnosis due to the following reasons: (i) the need for bulky DC power supply and (ii) the need to conduct the tests in dark because the intensity of the EL signal is several orders of magnitude lower than sunlight [48]. An attempt to adopt EL imaging on-field was presented in [49], where EL images were acquired by means of drone under sunlight. However, the study demonstrated that the camera detector suffered from a reduced sensitivity and signal-to-noise ratio (SNR), thereby compromising the identification of cracks.

Figure 2.5. EL image of a c–Si PV module tested at the Laboratory of Photovoltaics, University of York, York, U.K., using the setup sketched in Figure 2.4. The image highlights the presence of micro-cracks and inactive area.

2.4 Electric Techniques

This section focuses on monitoring techniques based on electric measurements. These approaches consist of acquiring electrical quantities, namely the current and voltage, directly from the PV field and then processing them to extract diagnostic information about the health and performance of the system. The principle behind these techniques is that faults and degradation mechanisms alter the electric behavior of the PV system. By analyzing these variations, it is possible to detect anomalies and, in some cases, infer their root causes. Compared to imaging-based approaches, electrical methods provide a clear fault classification and energy loss quantification. A classification of the common state-of-the-art electric methods is provided in the following subsections, covering Power Loss Analysis (PLA), methods based on the acquisition of few PV voltage

and current (V/I) points, IVT and IS.

2.4.1 Power loss analysis and voltage/current measurement

As previously mentioned, the electric methods can be classified depending on the level of granularity. The lowest level corresponds to the monitoring of the PV field as a whole, by measuring the instantaneous output power and converting it into the energy yield. The standard IEC 61724 [50] defines the Performance Ratio (PR), a performance metric used to quantify the system's efficiency and expressed as follows.

$$PR = \frac{P_i}{P_{nom}} \frac{G_{STC}}{G_i} \tag{2.1}$$

where P_i is the measured instantaneous output power, P_{nom} is the nominal power of the PV system, G_i is the measured irradiance and G_{STC} is the irradiance at the STC.

If PR is lower than 1, the PV field is underperforming and might be affected by faults. The PR gives a general idea about power loss. Methods based on the analysis of the PR cannot provide a fault localization nor a fault classification. A similar approach is proposed in [51, 52], based on the analysis of the data used by the Maximum Power Point Tracking (MPPT) algorithm. The main advantage is the minimal impact on the system because it does not require the disruption of the PV power production. However, this solution is only sensitive to a limited number of faults, and it does not prove the location of the fault, unless expensive microinverters are employed. As a result, inverter-level monitoring methods have the drawback of not being suitable for identifying faulty components. A more refined approach consists of increasing the level of granularity, such as measuring V/I, at string level rather than inverter level, as proposed in [53]. In their work, Chen and Wang [53] detected faults calculating the time correlations between the faulty signals measured at each string output and using autoregression models. In [54], a fault is detected comparing the stored data of a string with all other strings, in order to immediately identify the underperforming one. An improved fault location capability is attained by pushing the monitoring at the individual module level. Consequently, a pervasive sensor network is needed, increasing the cost and

complexity of the system. In [55, 56], each PV module within a PV string is equipped with wireless and self-powered sensor capable of measuring the OP, the I_{SC} and the V_{OC}. Although they remain an attractive solution for performing a precise fault localization and energy loss quantification, solutions based on the above-discussed methods cannot give a complete and comprehensive estimation of the state of health of PV modules. In fact, these methods enable the acquisition of few points of the I–V characteristics, *i.e.*, the OP, I_{SC}, V_{OC}, that are not sufficient to calibrate reliable models for diagnosing degradation mechanism.

2.4.2 Current–Voltage curve tracing

IVT is a standardized method for PV module diagnosis and characterization defined in IEC 60904-9 [57]. It consists of measuring the set of DC operating points spanning from the V_{OC} to the I_{SC}. The I–V curve provides the static characteristic of the PV module under given irradiance and temperature conditions. When measured in outdoor conditions, the I–V curves must be corrected employing the standard procedures defined in IEC 60891 [58]. The corrected I–V curves are then compared with the reference for the identification of PV faults. The type and severity of the faults significantly affect the degree of change of the I–V characteristics. Figure 2.6 provides an overview of the possible fault patterns occurring in the I–V curve. Curve 1 exhibits a rounder knee compared to the reference I–V curve, possibly due to light mismatch among cells or as effect of the Potential Induced Degradation (PID). PID, however, degrades the overall performance of the module causing a reduction of the nominal V_{OC}, as represented by curve 4. Similar effects is obtained in case of LID and shorted bypass diode. Modules affected by interconnect corrosion and slack joints exhibit a lower curve slope around the V_{OC} (see curve 2) whereas the presence of shunted cells may result in a decrease in the curve slope around the I_{SC}, similar to curve 3 in Figure 2.6. In case of uniform soiling or glass breakage, the amount of light absorbed by the module, and therefore the photo-current, is reduced, thereby resulting in curve 5. Finally, the ladder-shape curve (see curve 6) is obtained in case of partial shading conditions or heavy mismatch in modules protected by bypass diodes. A complete fault classification based on the deviations between the measured and expected I–V curves is reported in [27].

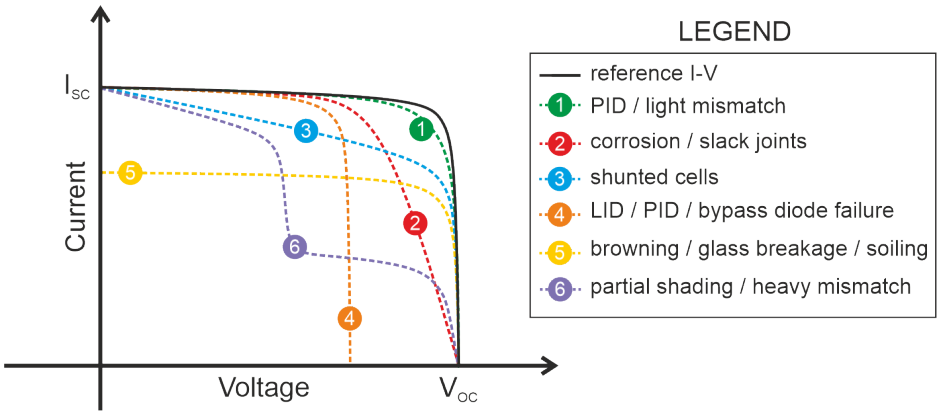

Figure 2.6. Examples of I–V curves under different faulty conditions.

Several studies proposed the implementation of algorithms for fault identification relying on data acquired at inverter/string level. In [59], Spataru et. al presented a method for detecting partial shading, PID and contact degradation using fuzzy logics. In [60], the faults are identified by comparing the I–V curve of normal strings to those of faulty strings whereas in more recent studies [61, 62], machine learning is employed to detect and classify faults in PV array using I–V data with accuracy up to 99%. A more sophisticated approach is proposed in [63], consisting of identifying PV modules degradation by extracting solely the series resistance. In this case, only the I–V curve region around the MPP is used. The partial acquisition of the I–V curve significantly reduces the measurement time as well as lowering the impact on the MPPT algorithm but at a cost of a reduced diagnostic capability. In the above-mentioned approaches, the I–V curves are measured by employing either inverters with I–V sweeping capability, or dedicated instruments, namely I–V curve tracers. The former can perform the measurement on-line, *i.e.*, during normal field operation, since they automatically disconnect the PV field during the measurement time. This approach eliminates the need for highly qualified operators to shut down the system and manually perform the measurement. It must be remarked that the primary function of the inverters is power conversion and therefore their design is not optimized for achieving the same metrological performance of dedicated I–V curve traces. These

latter, however, require direct access to the terminals of the tested PV field, which implies system shutdown and operator intervention. While this makes the monitoring procedure time-consuming and disruptive to normal operation, it ensures higher accuracy compared to inverter-based measurements. Since neither inverter-level nor string-level IVT allows to localize the faulty modules, the best performing option consists of measuring the entire I–V curve of each PV module within a string. This solution is relatively simple to implement in distributed conversion systems, thanks to the adoption of microinverters and DC power optimizers. However, it is worth stressing that these devices, similar to inverters, are conceived for power conversion rather than measurement instruments, thus impairing the I–V curve measurement. Examples of studies adopting dedicated I–V tracer for module-level diagnosis are presented in [64, 65]. As mentioned, the main limitations of state-of-the-art module-level approaches is the necessity to shutdown the PV field and perform a long and costly string disassembly. Since I–V tracers represent a central topic of this thesis, a detailed discussion of the limitations of the current state of the art, together with a proposed solution to this issue, is extensively presented in Chapter 4.

2.4.3 Impedance Spectroscopy

IS is a well-established technique to characterize electrochemical devices in the frequency domain. This technique consists of injecting small-signal perturbations, either voltage or current, at various frequencies superimposed to the system DC operating point and measuring the corresponding electrical response. In order to guarantee a valid IS measurement, the system must satisfy the following conditions: (i) linearity, (ii) time invariance and (iii) causality. Linearity, in particular, implies that the system obeys the superposition principles, meaning that the response to multiple AC perturbations is the linear combination of the response to each individual perturbation. In practical applications, this assumption can be considered valid only if the perturbation is sufficiently small, such that the current-voltage relationship can be locally approximated as linear (see Figure 2.7a). Under the assumptions (i)-(iii), the system response at a given frequency f can be described in terms of complex impedance:

$$\bar{Z}(j2\pi f) = \frac{\bar{V}(j2\pi f)}{\bar{I}(j2\pi f)} \tag{2.2}$$

where j is the the imaginary unit, $\bar{V}$ and $\bar{I}$ are, respectively, the voltage and current signals in the frequency domain.

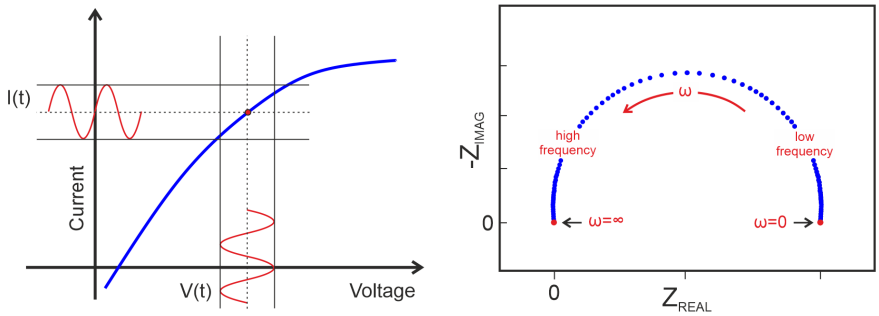

Figure 2.7. **(a)** In IS, if a non-linear system is excited with a perturbation sufficiently small, its current-voltage relationship can be locally approximated as linear. **(b)** Qualitative illustration of a complex impedance plotted in a Nyquist diagram, where the impedance is expressed as function of the angular frequency ω. The *x-axis* reports the real part of the impedance whereas the *y-axis* reports the imaginary part of the impedance. The red arrow indicates the direction of increasing ω points.

A common graphical representation of the complex impedance in the frequency domain is through the Nyquist plot, in which the real part of the impedance is reported on the *x-axis* and the imaginary part on the *y-axis*. A qualitative illustration of a Nyquist diagram is reported in Figure 2.7b, where the impedance is expressed as function of the angular frequency $\omega = 2\pi f$. The Nyquist diagram provides an intuitive way to assess system dynamics, since the impedance spectrum can be typically subdivided into contributions arising at low frequencies and contributions at high frequencies, each associated to different physical phenomena occurring inside the device under test. Impedance spectroscopy has been extensively used in biomedical studies, corrosion tests, and for the characterization of electrochemical storage devices, such as batteries. The increasing popularity of IS

is due to the capability of providing in-depth information about the internal processes of the tested device. More recently, impedance spectroscopy has been investigated as a tool for fault detection and characterization in PV modules. Although its application to PV modules is still in its early stages, encouraging preliminary results have highlighted the potential of IS for advanced monitoring and diagnostics. In particular, IS has demonstrated the capability to capture degradation mechanisms that are often difficult to identify using conventional electric methods. For example, in [22], the authors showed that the electrical signatures of microcracks induced by mechanical stress were more pronounced in the impedance response than in the I–V characteristics. This observation underscores the sensitivity of IS to localized defects that may otherwise remain undetected by other electric methods. Beyond cracks, other studies have revealed the correlations between PV impedance and interconnect ribbon disconnection [66, 22], and PID [67, 68, 69]. The main limitation of these studies lies in their restricted applicability under real operating conditions, as most results have been obtained indoors, under controlled irradiance and temperature conditions. An attempt to apply IS for on-field identification of PID is reported in [70], although the measurements were carried out exclusively under dark conditions. Similarly, Guejia-Burbano *et al.* in [71] demonstrated the potential of IS for detecting contact degradation through on-field measurements. However, the measurements were conducted by means of a bulky and costly frequency response analyzer. Finally, it is worth remarking that state-of-the-art approaches are limited to laboratory tests due to the lack of dedicated instrumentation capable of conducting impedance measurements on-field. This gap has motivated my research activity, resulting in the proposal of an innovative IS-based solution for on-field PV diagnostics. A comprehensive discussion of the limitations of state-of-the-art approaches and the proposed solution is presented in Chapter 5.

2.5 The proposed monitoring approach

This section provides a comprehensive summary of the state-of-the-art monitoring techniques reviewed in the previous sections. Building upon these findings, it proposes a hybrid monitoring strategy designed to address

the identified limitations of existing solutions. The proposed approach emphasizes the need for a dedicated portable device capable of performing on-field and on-line electrical measurements at the module level, thereby defining the main direction of the present research activity.

2.5.1 Summary of the reviewed state-of-the-art approaches

Table 2.1 summarizes the reviewed monitoring techniques by grouping the references according to the main adopted technique. For each study, the table reports the type of inspected system, the test conditions, specifically indicating whether the measurements were performed on-field or indoor, *i.e.*, in laboratory environment, and also specifies whether the method required offline operation, causing a complete shutdown of the PV system and string disassembly, or it has been applied on-line, *i.e.*, during normal PV system operation. For approaches based on electrical methods, the level of granularity is also highlighted, distinguishing between module-level, string-level, and inverter-level analysis. In addition, the table indicates the type of faults detected by each approach, and whether an auxiliary monitoring method was required to complete the diagnostic process. Finally, the limitations are summarized, providing a concise overview of their constraints in practical applications. Table 2.1 highlights the following aspects.

- Imaging methods are suitable for on-field and on-line testing, as they do not require any disruption of the inspected PV system, with the sole exception of EL. A similar advantage is provided by electric methods based on PLA and approaches exploiting inverters with I–V sweeping capability.
- The studies employing IRT can only identify faulty operating conditions, mainly hotspots, open and short circuits. They cannot provide information about the root causes of faulty conditions.
- The solely use of imaging methods does not enable the quantification of the energy loss associated with the fault. As a result, imaging approaches are often coupled with electric methods, which provide complementary capabilities in terms of fault classification and energy loss quantification.

- Electric methods applied at inverter and string level enable global performance evaluation but are unable to localize underperforming modules. Only module-level methods can directly identify the faulty or degraded module. Current module-level approaches, however, require the shutdown of the PV plant and a long and costly string disassembly. The measurements are therefore performed offline, on stand-alone modules that have been previously disconnected from the string.

- Among electrical methods, IVT is a standardized and widely used tool for on-field testing, whereas IS remains mostly confined to indoor characterization, due to the lack of portable frequency response analyzers.

2.5.2 Why module–level strategy

Based on the outcome of the literature review presented in the preceding subsection, it can be concluded that no single monitoring technique fully satisfies the requirements for effective PV monitoring and diagnostics. From a diagnostic perspective, the most comprehensive approach would consist of monitoring all PV modules within a field. However, this solution becomes impracticable in utility-scale PV plants, where the number of installed modules can reach several thousands. A more convenient solution is illustrated in Figure 2.8, where a hybrid monitoring strategy combining imaging inspection with a module-level electric method, is suggested. In the first instance, a UAVs equipped with a thermal camera performs a scan of the PV plant as a whole, enabling fault detection and fault localization module by module. Subsequently, once the faulty module has been identified, a module-level monitoring device, based on an electric method, such as IVT or IS, can be plugged into the terminals of the faulty module. The data provided by the monitoring device allow to perform the remaining steps of the diagnosis, namely fault classification and energy loss quantification. The proposed hybrid strategy offers a favorable trade-off between diagnostic accuracy and system cost and complexity, since it does not require the installation of dedicated hardware on every module. Instead, hardware is only needed for the module identified as potentially

faulty by the imaging survey. Moreover, the module-level device should be designed to temporarily disconnect the PV module from the string while providing an alternative path to the string current, thereby minimizing the impact of the monitoring procedures on the overall system operation.

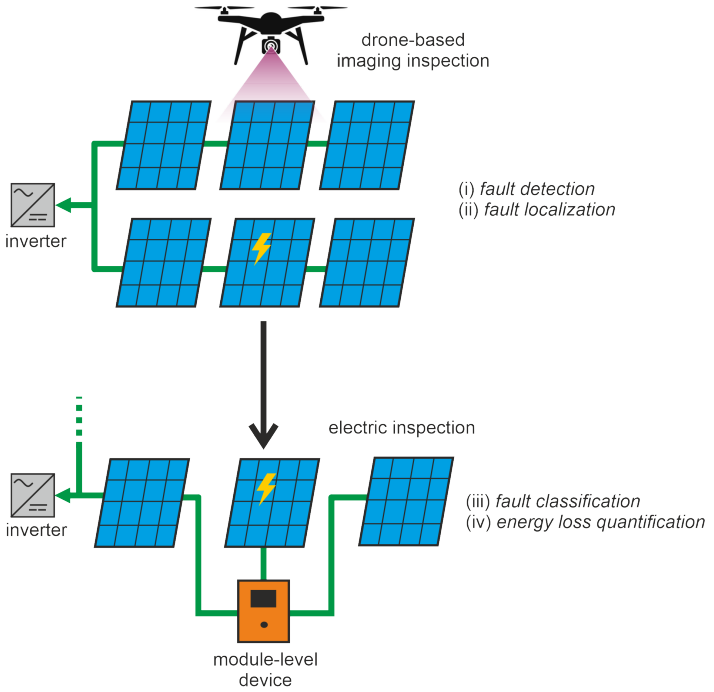

Figure 2.8. Proposed hybrid monitoring approach, based on the combination of imaging inspection and module-level electric method. As a first step, a UAV equipped with a IRT camera scans the PV field as a whole, for detecting possible faults and localizing the faulty module. Subsequently, the faulty module is connected to a monitoring system ("module-level device") for fault classification and energy loss quantification. The proposed module-level device must guarantee the normal operation of the string, *i.e.*, on-line diagnosis.

In this context, the present thesis proposes innovative solutions for on-field, module-level diagnostics, leveraging IVT and IS .

2.6 Conclusions

This chapter provided a comprehensive overview of the state of the art in PV monitoring techniques and established the motivations behind the adoption of module-level monitoring in this dissertation. The literature review highlighted the strengths and limitations of both imaging- and electric-based approaches. Imaging methods offer the advantage of on-field and on-line operation without disrupting system performance, with the exception of EL. However, while imaging can detect faulty conditions, it often cannot identify the root causes of these faults nor quantify the associated energy losses. Consequently, imaging techniques are frequently combined with electric methods, which provide complementary diagnostic capabilities, including fault classification and energy loss quantification. Electric monitoring approaches applied at the string or inverter level allow for global performance evaluation but cannot localize underperforming modules. Module-level monitoring is essential to identify degraded or faulty modules; however, current solutions typically require offline operation, involving plant shutdown and string disassembly, which is time-consuming and costly. Among these methods, IVT is a widely standardized tool for on-field testing, while IS remains largely confined to laboratory environments due to the complexity and size of conventional equipment. The literature review underscores that no single monitoring technique fully satisfies the requirements for accurate and cost-effective PV diagnostics. In utility-scale installations, where thousands of modules may be deployed, a comprehensive monitoring strategy consisting of equipping all modules with an instrument is impractical. To address this challenge, this chapter introduced a hybrid monitoring strategy combining imaging inspection with module-level electrical diagnostics. In this approach, a thermal camera mounted on a UAV scans the PV plant to detect and localize potential faults. Subsequently, a module-level device employing an electric method is temporarily connected to the identified module to perform fault classification and energy loss quantification. This strategy provides a favorable trade-off between diagnostic accuracy and system cost, as dedicated hardware is required only for modules flagged as potentially faulty. Moreover, the device can be designed to maintain string current flow during measurements, minimizing the impact on the system operation.

Table 2.1. Summary of the reviewed state-of-the-art monitoring techniques.

Monitoring Technique	Reference	Inspected PV system	Other techniques	Level	Test	Identified faults/faulty conditions	Limitations
Visual Inspection	[34]	1.1 kW PV plant	IRT, PLA	-	On-field/On-line	Snail trails, bird dropping, frame corrosion, discoloration	Time consuming for large PV plants
IRT	[44]	Stand alone PV module	PLA, V/I	-	On-field/Off-line	-	-
	[45]	Grid-connected PV plant	PLA	-	On-field/On-line	Hotspots, PID, Open circuit, Short circuit	-
	[42]	1 MW PV plant	-	-	On-field/On-line	Hotspots	Sunlight reflection errors
	[43]	115.36 MW PV plants	-	-	On-field/On-line	Hotspots, partial shading, module breakage	-
EL	[49]	Stand alone PV module	V/I	-	On-field/Off-line	Cracks, micro-cracks	Sunlight reduces crack identification
	[46]	Solar cells	IVT	-	Indoor/Off-line	Cracks, micro-cracks	Only small cells tested
	[47]	Solar cells/PV modules	PLA	-	Indoor/Off-line	PID	Cannot be performed on-field
PLA	[51]	1.98 kW PV plant	-	Inverter	On-field/On-line	-	Cannot classify faults
	[52]	9.6 kWp PV plant	-	Inverter	On-field/On-line	Inverter disconnection, partial shading	Cannot localize faults

Continued on next page

Monitoring Technique	Reference	Inspected PV system	Other techniques	Level	Test	Identified faults	Limitations
IVT	[61]	4 kW PV plant	-	Inverter	On-field/On-line	Shading, Open circuit, Short circuit	-
	[59]	0.9 kW PV string	-	String	On-field/-	Shading, PID, contact degradation	Cannot localize faults
	[64]	250 Wp module	-	Module	On-field/Off-line	Partial shading	Bulk electronic load limits on-field use
	[62]	-	-	String	Indoor/-	Partial shading	-
IS	[22]	Solar cell	IVT	Cell	Indoor/Off-line	Cracks, degradation, PID, ribbon disconnection	Not validated on PV modules
	[67]	Solar cell/PV module	-	Module	Indoor/Off-line	PID	-
	[71]	PV module	IVT	Module	On-field/Off-line	Contact degradation	Bulky lab-grade impedance analyzers makes use on-field impractical
	[68]	PV module	EL	Module	Indoor/Off-line	PID	-
	[69]	PV module	EL, IVT	Module	Indoor/Off-line	PID, degradation	-

Chapter 3

Advanced Modeling for Fault Diagnosis and Estimation of Energy Production

3.1 Introduction

In this chapter, my research activity on the modeling of PV modules is presented, with the aim of describing both their static (*i.e.*, DC) and dynamic (*i.e.*, AC) electric behavior. Accurate modeling of PV devices plays a dual and complementary role in the field of fault diagnosis and energy prediction. On one hand, PV models are indispensable for *parameter extraction*, which is essential for evaluating the health status and performance degradation of modules over time. As discussed in Chapter 2, electrical monitoring techniques inherently rely on the accurate definition of such models to identify fault conditions and degradation mechanisms. On the other hand, PV models serve as fundamental tools for *estimating energy production*, enabling the prediction of system performance under diverse irradiance and temperature conditions and contributing to the optimization of the system's design. The models analyzed and developed in this chapter are conceived to simulate the behavior of silicon-based PV modules, which remain the technological backbone of the solar industry. c–Si technology, in particular, stands as benchmark for PV deployment at large-scale, offering consistent performance over time at relatively low production costs,

and long-term stability compared to alternative PV technologies such as thin film and emerging perovskite solar cells [72]. Furthermore, the modeling approaches discussed here can be readily extended to bifacial modules, which are gaining interest due to their ability of producing more energy compared to conventional mono-facial counterparts.
This chapter is structured around the progressive development of *circuit-based models*, addressing both diagnostic and predictive challenges. It begins with an in-depth discussion of the conventional DC models used to describe the static I–V behavior of PV devices. Based on circuit-based DC models, an innovative tool for energy prediction is proposed. This tool embeds a novel cell-level irradiance model specifically designed for bifacial modules, but readily adaptable to monofacial technology. The proposed tool aims to account for albedo-induced mismatch losses, neglected in existing view factor approaches. Finally, the analysis gradually extends to dynamic models capable of capturing the frequency-dependent response of PV modules.

3.2 DC electrical models

The DC electrical output of PV systems can be described through a range of mathematical models, each providing different levels of accuracy and computational complexity. These models offer predictive capabilities under varying operating conditions, primarily as functions of solar irradiance, ambient temperature and wind speed. The available modeling approaches can be generally categorized into simplified models, semi-empirical models and physics-based models. Simplified models, like PVWatts developed by NREL [73], estimate the DC power output based on the system's nameplate DC rating, the plane-of-array irradiance and, and the ambient temperature. These models are computationally efficient and useful for large-scale energy yield assessments. However, this simplicity limits their applicability to PLA, as they do not reproduce the full I–V characteristics of the PV system. Advanced models, such as the semi-empirical Sandia Array Performance Model (SAPM) [74], are capable of estimating the entire I–V curve. The SAPM model combines both physical parameters, such as the diode ideality factor and reverse saturation current, and empirical performance coefficients to accurately fit the

shape of the I–V curve. These empirical coefficients are obtained through regression analysis on experimental I–V data. Although this approach provides high accuracy, the coefficients themselves lack physical meaning and therefore do not offer insights into the degradation mechanisms or state of health of the PV module. Physics-based models,such as the SDM, employ equivalent electrical circuits to reproduce the I–V characteristics of PV cells and modules. These models simplify the complex semiconductor physics into a set of lumped electrical elements (e.g., current source, diode, series and shunt resistances), allowing for both analytical and simulation-based studies. Importantly, the extracted parameters retain clear physical interpretation, making it possible to relate them to specific material degradation phenomena and performance losses over time. In this section, the SDM is introduced to describe the static I–V characteristics of PV cells and modules. The discussion is first developed at the cell level, and then extended to the module level, highlighting the scaling effects and parameter aggregation that occur when individual cells are interconnected.

3.2.1 Single diode model

The commonly used model is the SDM, also known as the five-parameter model. The SDM can be classified as a compact circuit model because, as previously mentioned, it reproduces the I–V behavior of a physical device using a small number of lumped electrical elements. A schematic representation of the SDM is sketched in Figure 3.1.

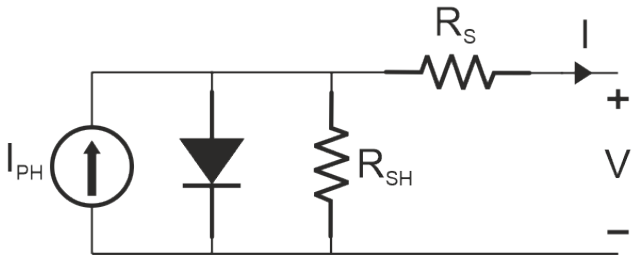

Figure 3.1. Schematic representation of the SDM, comprising a current source I_{PH}, representing the photo-current generated under solar irradiation, a diode, a series resistor R_S and a shunt resistor R_{SH}. V and I are, respectively, the output voltage and current of the solar cell.

In this formulation, the solar cell is modeled as a current source I_{PH}, representing the photo-current generated under solar irradiation, in parallel with a diode that accounts for the p-n junction behavior in dark condition. The parallel diode is described by the ideality factor n and it is used to simulate the polarization phenomenon and the reverse saturation current I_0. A series resistor R_S and a shunt resistor R_{SH} are also introduced to simulate ohmic and current leakage losses [75]. The analytical formulation of the SDM is reported in the following.

$$I = I_{PH} - I_0 \left[\exp\left(\frac{V + R_S \cdot I}{n \cdot V_T} \right) - 1 \right] - \frac{V + R_S \cdot I}{R_{SH}} \tag{3.1}$$

where V_T is the thermal voltage, V is the output voltage and I is the output current of the solar cell. V_T is given as follows.

$$V_T = \frac{k \cdot T}{q} \tag{3.2}$$

where k is the Boltzmann constant, T is the cell temperature and q is the electron charge. The photo-current depends on the incident irradiance and it can be expressed as follows.

$$I_{PH} = \frac{G}{G_{STC}} I_{SC,STC} \tag{3.3}$$

Where $I_{SC,STC}$ is the short circuit current at STC, G_{STC} is the irradiance at STC and G is the incident irradiance .

Depending on the particular case study, the SDM offers a good trade-off between simulation accuracy and computational complexity. However, under low irradiance conditions, the SDM may not accurately model the results, due to the effect of the recombination current in the space-charge region [76]. Consequently, the SDM can be extended including an additional parallel diode, *i.e.*, Double Diode Mode (DDM), to model the recombination current, at the cost of increased parameter complexity. Few studies [77] increased the model accuracy adding more than 2 diodes in the equivalent electrical circuit, resulting in a complex matrix of diodes to finely simulate the electric behavior of heterojunction solar cells. The definition of such models is highly specialized for multi-structured solar cells and therefore falls outside the scope of this thesis. In this research

activity, the modelled PV modules were assumed to operate under real operating conditions, *i.e.*, exposed to sunlight. Consequently, since the PV modules are not expected to work under low level of irradiance, the SDM is considered sufficiently accurate to describe the static behavior of the PV module under test.

3.2.2 Bifacial technology

Recent literature proposes an extended version of the SDM for the description of bifacial solar cells. Since they can harness reflected and diffused sunlight on the rear side, the increment of PV current due to light absorbed at the rear side can be accounted for adding another current source ($I_{PH,r}$) in parallel with the one representing the front side ($I_{PH,f}$). The modified analytical equation is reported in the following.

$$I = I_{PH,f} + I_{PH,r} - I_0 \left[\exp\left(\frac{V + R_S \cdot I}{n \cdot V_T} \right) - 1 \right] - \frac{V + R_S \cdot I}{R_{SH}} \tag{3.4}$$

The values of $I_{PH,f}$ and $I_{PH,r}$ are determined from the front (G_F) and rear irradiance (G_R), and calculated as follows.

$$\begin{aligned} I_{PH,f} &= \frac{G_F}{G_{STC}} I_{SC,STC} \\ I_{PH,r} &= \frac{G_R \cdot \varphi}{G_{STC}} I_{SC,STC} \end{aligned} \tag{3.5}$$

where φ is the bifaciality factor.

3.2.3 From solar cell to photovoltaic module

In PV modules, the solar cells are interconnected in series and parallel configurations to achieve the desired voltage and current ratings. When N cells are connected in series to form a sub-module, the total sub-module voltage corresponds to the sum of the voltages of the individual cells, while all cells within the sub-module share the same current. Conversely, when M sub-modules are connected in parallel, the module current is obtained as the sum of the currents of the parallel branches, whereas the module

voltage is equal to the voltage of each sub-module. Assuming that all cells are identical and operate under uniform conditions in terms of incident irradiance and working temperature, the equivalent electric circuit for a monofacial PV module can be expressed as a straightforward extension of the SDM, obtained by appropriately scaling the five parameters [78].

$$\begin{aligned} I_{PH,mod} &= N \cdot I_{PH,cell} \\ I_{0,mod} &= N \cdot I_{0,cell} \\ n_{mod} &= N \cdot n_{cell} \\ R_{S,mod} &= \frac{N}{M} \cdot R_{S,cell} \\ R_{SH,mod} &= \frac{N}{M} \cdot R_{SH,cell} \end{aligned} \tag{3.6}$$

This relation also holds for larger PV structures, such as string and arrays, where multiple modules are interconnected. In this context, the entire I–V curve can be obtained simply by multiplying the current by M and the voltage by N. The main advantage of this approach is that it allows the behavior of large-scale PV systems to be accurately described using a compact and computationally efficient model. In case of mismatched conditions, e.g., partial shading, defective and faulted cells, the I–V curve is altered, and therefore the scaling approach of Equation (3.6) is no longer valid. To this end, a more comprehensive cell-level model that (i) describes each cell with a SDM and (ii) includes the model of bypass diodes, must be employed to appropriately describe the behavior of the PV module.

Let us consider a mono-facial PV module comprising 3 sub-modules, each protected by a bypass diode, and N cells within a sub-module. Each cell is described by a SDM. The complete equivalent electric circuit of the PV module is shown in Figure 3.2. To demonstrate the potential of the proposed cell-level model, a SPICE simulation is carried out under mismatch conditions. Specifically, it is assumed that one cell in submodule 1 of Figure 3.2 is partially shaded, generating a reduced photocurrent (3.5 A) compared to the unshaded cells (their photo current is 5 A).

As can be seen from Figure 3.3a, as the module current increases beyond 3.5 A, the bypass diode protecting submodule 1 is activated, thereby excluding the shaded submodule from the current path. As a result, the

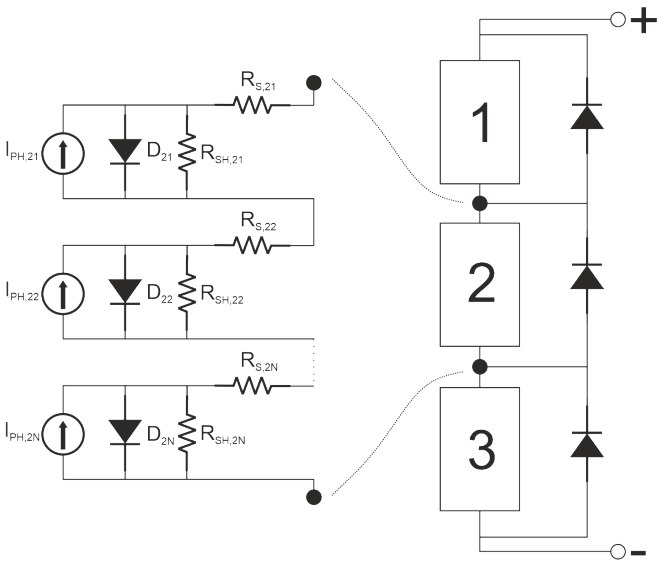

Figure 3.2. Cell-level equivalent electric model of a PV module including the bypass diodes. In this example, the modules comprises 3 sub-modules, each containing N solar cell. Each solar cell is described by means of the SDM.

I–V curve of the PV module exhibits a stepped behavior compared to the reference curve , which is instead obtained under uniform conditions. It is worth noting that a cell-level model accurately reproduces the difference in the I–V curves of each sub-module, that are otherwise hidden in low granularity models. As can be observed in Figure 3.3a, the sub-modules differ not only in their I_{SC} but also in the roundness of the knee around MPP, which appears sharper for the shaded sub-module and smoother for the unshaded ones. Beyond a qualitative description of the I–V curve, the cell-level model is also a powerful tool for investigating fault-related mechanisms, such as hotspot. As shown in Figure 3.3b, at certain operating points (*e.g.*, yellow marker), the shaded cell is forced to operate in reversed bias, thereby dissipating current rather than transferring power to the output. This phenomenon leads to local increase of temperature that may trigger hotspot formation.
Even though the scaled version of the SDM of Equation (3.6) provides an adequate description of the I–V curve of mono-facial PV modules under

uniform operating conditions, this approach cannot be extended to bifacial modules. In bifacial technology, the rear side of the module receives irradiance primarily from the ground albedo. The amount of albedo collected by the cell depends on its position on the module and its distance from the ground. In practice, bifacial solar cells operate under mismatch conditions due to the nonuniform distribution of the albedo impinging on the rear. This leads to unequal photo-currents generated among cells. Existing bifacial models based on the view factor method neglect the albedo-induced mismatch by assuming that all cells generate the same photo-currents, thereby adopting the simplified module-level formulation presented in Equation (3.6). Although computationally efficient, this simplification does not capture the real operating behavior of bifacial modules. To capture this effect, a cell-level modeling framework becomes necessary. The implications of albedo-induced mismatch in bifacial PV technology are discussed in the following section.

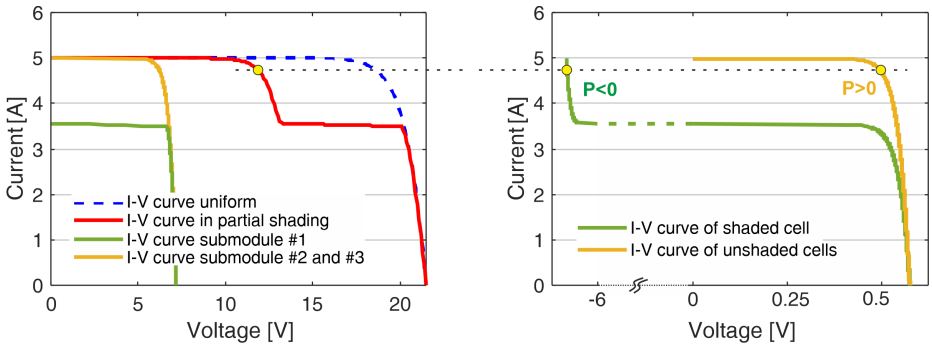

Figure 3.3. **(a)** I–V curve of the simulated PV module under uniform conditions (blue dashed line) and stepped I–V curve obtained in case one cell is partial shaded (red solid line). The green solid curve is the I–V curve of submodule 1, whereas the yellow solid curve is the I–V curve of submodule 2 and 3. **(b)** In green the I–V curve of the shaded cell whereas in yellow the I–V curves of the unshaded cell within the module. When the module is bypassed, the shaded cell works in reverse mode, thereby dissipating power (P<0) rather than transferring power to the output (P>0), as in the case of unshaded cells.

3.3 A tool for the estimation of energy production

The availability of reliable tools devoted to the estimation of power production plays a crucial role in the monitoring and diagnosis of PV faults. As introduced in Chapter 2, electric methods often rely on the identification of deviations between the measured energy output and the expected production. The degree of deviation serves as early indicators of system degradation, mismatch and other failure mechanisms. To be effective, those tools require accurate computation of the incident irradiance. The emerging of bifacial technology poses a challenge in the accurate estimation of the incident irradiance under different operating scenarios, because of the need to model the light absorption on the rear side [79]. The methods for the estimation of the incident irradiance in bifacial PV systems can be classified into those based on ray-tracing [80, 80, 81, 82] and those based on view factor [20, 21, 3, 4, 2]. Ray tracing simulates the path of light rays and their interaction with objects in a scene surrounding the bifacial PV module. The main advantage of this approach is the ability to account for nonuniform light reflection, varying albedo and nearby objects that can cause partial shading on the module under investigation, enabling an accurate irradiance estimation at cell level. However, ray tracing suffers from a high computational burden, and simulations can take a long time to complete. To tackle these limitations, view factor-based methods are preferred. Such approaches require less computational resources, making them suitable even for large PV installations.
In existing view factor-based models, the solar irradiance hitting the front and rear of the bifacial PV module is assumed to be uniform because it is computed at module level. Instead, in real-world conditions, light nonuniformity might affect both the front and rear, thus leading to mismatch losses [81]; in particular, the rear can suffer from a nonuniformity in the albedo reflection. The front and rear irradiances are used to calculate the photo-currents on both the module sides according to Equation (3.5). Consequently, in module-level approaches, potential mismatch losses among cells are disregarded since the front and rear photo-currents are uniform even in absence of partial shadings. To address this gap, this section presents an original contribution developed during my research activity: a novel 3D circuit-based modeling framework for bifacial PV mod-

ules. Unlike conventional view factor-based approaches, the proposed tool computes the incident irradiance at cell granularity, accounting for spatial nonuniformities on both the front and rear surfaces. This allows for a more accurate estimation of the generated photo-currents and, consequently, of energy production, while also capturing the effect of albedo-induced mismatch losses that are overlooked by state-of-the-art methods.

3.3.1 Cell-level irradiance model

The proposed tool is sketched in Figure 3.4, and it can be divided into (i) a Matlab [83] script for the evaluation of the irradiance hitting the cells both on front and rear side and (ii) a circuit-based model implemented in LTSPICEXVII [84] for the simulation of the I–V curves and produced power. With regard to (ii), the circuit-based model creates a netlist where the PV systems is described as the series connection of N cells, each described by the SDM of Equation (3.4), and sub-modules protected by bypass diodes.

The input of the irradiance model implemented in (i) includes data regarding the geographic location (latitude and longitude), the total irradiance G_{toth} and diffuse irradiance G_{dh} on the horizontal plane, which can be retrieved from the PVGIS database [85] for an average day of the month, the installation parameters (tilt angle β, module azimuth γ, elevation from ground E_P, and ground albedo ρ_g), as well as the geometrical dimensions of the PV module, namely, the height H_m, width W_d, thickness d_m, and width of the metal frame d_f. A cell-level 3D scenario of the PV installation is created in Matlab for the calculation of the beam, diffuse, and albedo components of the irradiances on each cell both on the front and rear of the module. The global irradiance hitting the *i-th* solar cell on the front $G_{F,i}$ is computed as the sum of beam, diffuse, and albedo components (*transposition model*) [86], *i.e.*,

$$G_{F,i} = G^F_{b,i} + G^F_{d,i} + G^F_{a,i} \tag{3.7}$$

with

$$G_{b,i}^F = G_{bh} \cdot R_{b,i}^F \tag{3.8}$$

$$G_{d,i}^F = G_{dh} \cdot F_{sky,i}^F \tag{3.9}$$

$$G_{a,i}^F = G_{toth} \cdot F_{ugnd,i}^F \cdot \rho_g + G_{dh} \cdot \rho_g \cdot \sum_{j=1}^{N} F_{sgnd,ij}^F \cdot F_{gsky,j} \tag{3.10}$$

where the superscript F refers to the front side, $G_{b,i}$ is the beam irradiance, G_{bh} is the beam irradiance on the horizontal plane calculated as $G_{toth} - G_{dh}$, $G_{d,i}$ is the diffuse irradiance, $G_{a,i}$ is the albedo component of

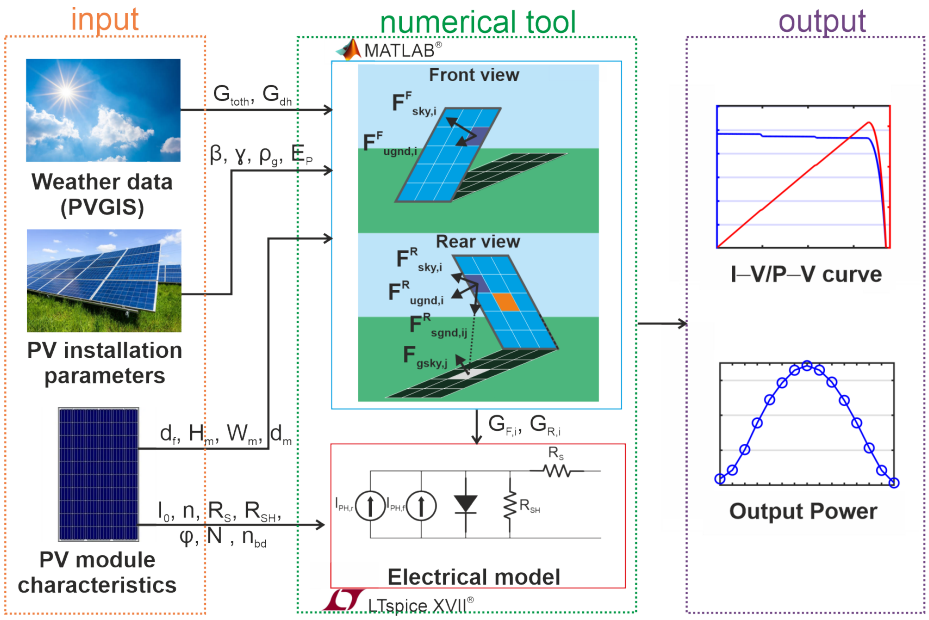

Figure 3.4. Framework of the proposed numerical tool. The tool consists of a Matlab script that computes the irradiance received by each cell included in the simulated PV module, based on input parameters such as weather data obtained from PVGIS database, electrical and mechanical parameters of the PV module and installation parameters. The script generates the Spice netlist of the PV module. The tool outputs the I–V/P–V curve and the generated power for each time instant of the day .

the irradiance, $R_{b,i}$ is the ratio of tilted irradiance to horizontal irradiance, $F_{sky,i}$ is the view factor of the solar cell to the sky, $F_{ugnd,i}$ is the view factor of the solar cell to unshaded ground, $F_{sgnd,ij}$ is the view factor of the *i-th* solar cell to the shadow cast by the *j-th* solar cell, and $F_{gsky,j}$ is the view factor of the shadow cast by the *j-th* solar cell to the sky, first introduced in [3]. The ratio of the titled and horizontal irradiance is calculated as follows:

$$R_b^F = \begin{cases} \frac{cos\theta}{sin\alpha}, & \gamma - \frac{\pi}{2} \leq \omega \leq \gamma + \frac{\pi}{2} \\ 0, & \omega < \gamma - \frac{\pi}{2} \text{or} \omega > \gamma + \frac{\pi}{2} \end{cases} \tag{3.11}$$

where θ is the incidence angle of the Sun rays on the front side, α is the solar altitude, and ω is the hour angle.

Similarly, the global irradiance impinging on the rear is obtained as follows.

$$G_{R,i} = G_{b,i}^R + G_{d,i}^R + G_{a,i}^R \tag{3.12}$$

with

$$G_{b,i}^R = G_{bh} \cdot R_{b,i}^R \tag{3.13}$$

$$G_{d,i}^R = G_{dh} \cdot F_{sky,i}^R \tag{3.14}$$

$$G_{a,i}^R = G_{toth} \cdot F_{ugnd,i}^R \cdot \rho_g + G_{dh} \cdot \rho_g \cdot \sum_{j=1}^{N} F_{sgnd,ij}^R \cdot F_{gsky,j} \tag{3.15}$$

where the superscript R refers to the rear side. The ratio of the titled irradiance and horizonal irradiance is calculated replacing θ with $180 - \theta$ in (3).

$$R_b^R = \begin{cases} 0, & \gamma - \frac{\pi}{2} \leq \omega \leq \gamma + \frac{\pi}{2} \\ -\frac{cos\theta}{sin\alpha}, & \omega < \gamma - \frac{\pi}{2} \text{or} \omega > \gamma + \frac{\pi}{2} \end{cases} \tag{3.16}$$

The view factor F defines the portion of radiation striking a surface. Figure 3.5 depicts an illustrative representation of all view factors involved.

The view factor between the *i-th* and *j-th* surfaces $F_{i,j}$ is calculated according to the following formula.

$$F_{i,j} = \frac{1}{A_i} \int_{A_i} \int_{A_j} \frac{cos\phi_i \cdot cos\phi_j}{\pi s^2} \, dA_i \, dA_j \tag{3.17}$$

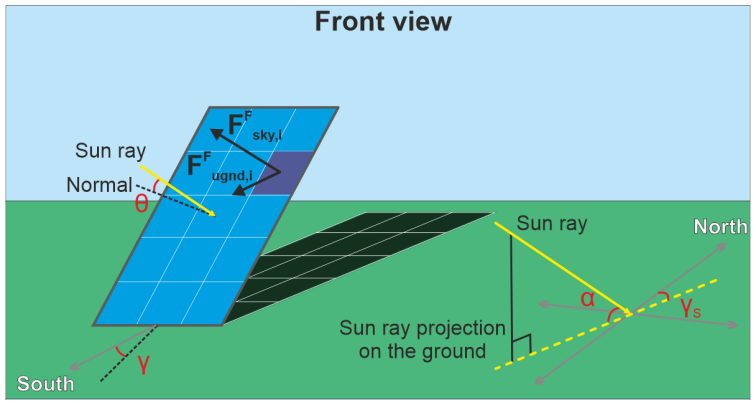

(a)

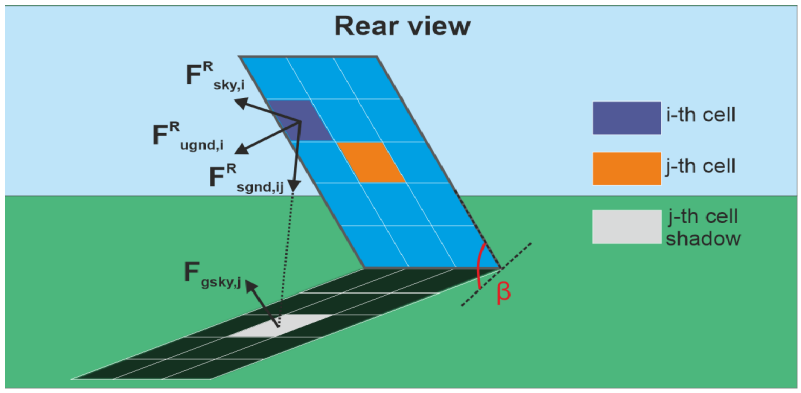

(b)

Figure 3.5. Schematic of the solar cell view factors computed for both **(a)** the front and **(b)** the rear of the module.The *i-th* cell is highlighted in dark blue, the *j-th* cell is highlighted in orange, whereas the shadow cast by the *j-th* cell onto the ground is highlighted in light grey. The position of the sun is defined by the solar altitude α and the solar azimuth γ_S, while the orientation of the module is defined by the azimuth angle γ and the tilt angle β. The incidence angle between the Sun rays and the module normal is denoted as θ.

where A is the area, ϕ is the angle of the normal to the surface, and s is the Euclidean distance between the two surfaces. The view factor is numerically computed using the adaptive quadrature algorithm. It is worth noting that the proposed irradiance model accounts for the presence of the metal frame on the rear, which partially reduces the view between solar cells and ground. The proposed irradiance model can be easily extended to the case of monofacial technology imposing $G_{R,i} = 0$.

3.3.2 Comparison with other approaches

To assess the performance and accuracy of the proposed cell-level approach, we present a detailed comparative simulation analysis with the commonly used module-level approaches as well as the state-of-the-art ones. The comparison is performed under ideal conditions, specifically in the absence of partial shading and malfunctioning cells, ensuring that any discrepancies with respect to other approaches are solely dictated by the albedo-induced nonuniformity on the rear. The comparative analysis is carried out on the Suntech STP430S-C54 bifacial module in half-cut technology [87], whose main specifications are reported in Table 3.1. Such a module is assumed to be located in Naples, Italy, under clear-sky conditions, and oriented South with a tilt angle β of 30° to maximize the collection of solar irradiances hitting the front surface during the year.

Table 3.1. Bifacial PV module specifications

Parameter	Value
Number of cells	108 (6×18)
Number of bypass diodes	3
Dimensions	1722 mm × 1134 mm × 30 mm
Metal frame dimensions	30 mm × 30 mm
Bifaciality factor	80%
P_{MAX} @ STC	430 W
V_{OC} @ STC	38.25 V
I_{SC} @ STC	14.17 A

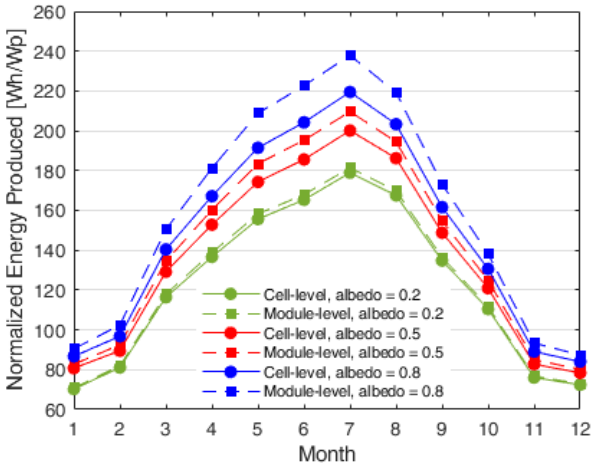

Figure 3.6. Energy produced by a South-oriented 30° tilted bifacial module normalized to peak power throughout a year, at different albedo values, namely 0.2 (green curves), 0.5 (red curves) and 0.8 (blue curves). The dashed lines and square symbols refer to the traditional module-level approach whereas the solid curves and round symbols refer to the proposed cell-level strategy.

Comparison with a traditional module-level approach

First, the power production of the module under test is simulated in different configurations and at various albedo values with the proposed cell-level approach, and then the results are compared with those obtained using a traditional module-level strategy. The latter was implemented using the same workflow shown in Figure 3.4, where the view factors were calculated considering the PV module as a single and unified surface, that is, all the cells embedded in the front receive the same irradiance, and all the cells belonging to the rear share the same irradiance. Figure 3.6 shows the energy production over one year normalized to the peak power at various albedo values, as estimated by the proposed cell-level approach and a traditional module-level strategy. From Figure 3.6, it can be observed that the traditional module-level approach overestimates the energy yield with respect to the proposed cell-level approach.

In module-level approach, the irradiance impinging on the module rear is uniformly distributed, meaning that all solar cells receive the same

albedo component reflected from ground and consequently share the same photo-current. By contrast, the proposed cell-level approach accurately describes the spatial nonuniformity of the albedo incident on the rear, allowing each cell to receive a different irradiance value based on its position relative to the ground. Since the cells are electrically connected in series, the overall power output of the module is limited by the cell that receives the lowest irradiance due to less favorable positioning with respect to ground. The irradiance mismatch among cells becomes more significant at higher albedo and during summer months, where the amount of solar irradiance impinging on the rear side can reach up to 30% of the total irradiance collected by the module. Figure 3.7a illustrates the scenario of the bifacial module on June 15$^{\text{th}}$ at 14:00. The Sun is located due South, thus projecting the shadow of the module on the back.

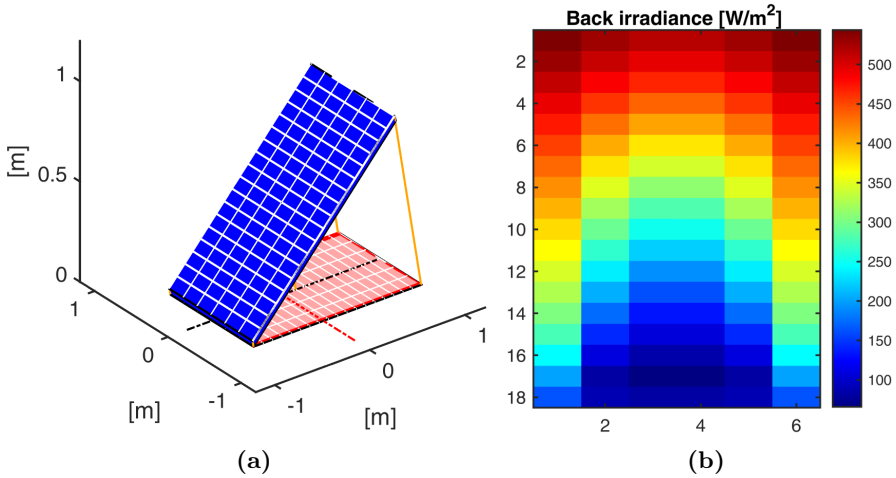

Figure 3.7. **(a)** 3D scenario of a South-oriented 30° tilted bifacial module (depicted in blue) on June 15$^{\text{th}}$ at 14:00. The corresponding shadow projected by the Sun rays (solid orange lines) onto the ground is depicted in red. **(b)** Irradiance distribution over the rear of the module.

The I–V and P–V characteristics of the bifacial module in this case study are reported in Figure 3.8. The figure shows that the module-level strategy overestimates the MPP by 8% compared to the proposed approach. This overestimation arises from the assumption that all rear cells

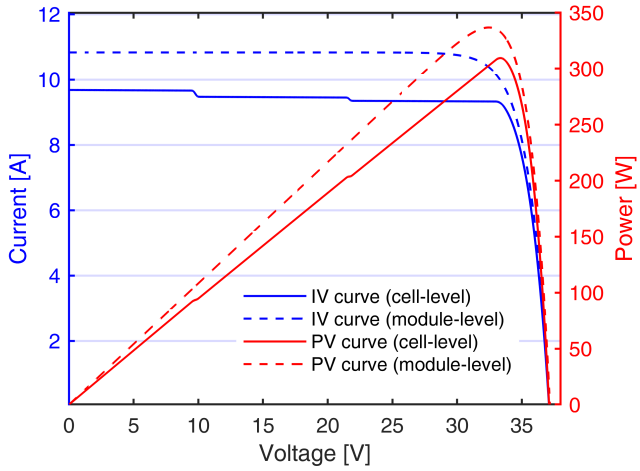

Figure 3.8. I–V (in blue) and P–V (in red) characteristics of a South-oriented 30° tilted bifacial module on June 15$^{\text{th}}$ at 14:00 with $\rho_g = 0.8$ obtained using the cell- (solid lines) and module-level (dashed) approaches.

receive identical irradiance, neglecting the spatial nonuniformity in albedo reflection. In practice, the solar cells located close to the ground receive less irradiance than those located on the top side of the module (see Figure 3.7b). The nonuniform irradiance distribution across the cells leads to current mismatch, resulting in an I–V curve with multiple steps. This stepped profile leads to a lower global MPP compared to the one predicted by the module-level approach.

Comparison with state-of-the-art approaches

The proposed approach is also compared with two state-of-the-art counterparts: the tool presented in [4], which uses the analytical irradiance modeling strategy outlined in [3] and the open-source library pvlib [2]. The irradiance model presented in [3] is based on the following assumptions: (i) all the cells embedded in the front side share the same irradiance; (ii) all the cells belonging to the back side share the same irradiance; (iii) the albedo component is determined from a two-dimensional (2D) representation of the Sun-module-shadow scenario, where the Sun is always seen by

the module front, the position of the Sun and the direction of the solar rays are solely defined by the altitude α, and the position of the module is only defined by the tilt angle β; as a result, the rear-ground view factors only depends on α and β and are calculated using the Hottel cross-string rule [20], [88]. Concerning the cell-level circuit simulation tool in [4], once the temperature dependence on irradiance is deactivated, it coincides with that proposed in this work. Conversely, the irradiance model presented in [2] relies on the following assumptions: (i) all the cells in the front share the same irradiance; (ii) all the cells belonging to the rear share the same irradiance; (iii) the evaluation of the albedo component is based on a quasi-3D geometric representation; although the position of the Sun with respect to the module is defined by α and γ_s, the view factors are calculated considering a 2D representation of the Sun-module-shadow scenario. In this case, the view factors are computed using the *pvfactors* engine, a matrix-based approach for solving the radiosity equations for each surface over time [89]. Regarding the estimation of the generated power, [2] implements the NREL power model [73]. Figure 3.9 shows the total irradiance collected by the module during June 15^{th} considering $\rho_g = 0.2$ as determined by the proposed approach, [4], and [2].

Let us first compare the irradiances determined by the three approaches. In Figure 3.9, the blue dots represent the mean value of the set of cell irradiances calculated through the proposed irradiance model at chosen time instants on June 15^{th}, while the bars indicate the maximum and the minimum irradiance collected by each of them. As shown in the figure, the irradiance discrepancy between the cells, quantified by the length of the blue bars, reaches the peak (106.9 W/m2) around noon and tends to decrease in the early morning and late evening. It can be easily inferred that both the approaches in [3] and [2] underestimate the collected irradiance with respect to the mean value of the irradiance calculated by the proposed model. The origin of the irradiance discrepancy shown in Figure 3.9 lies in the different Sun-module-shadow scenario adopted for the albedo calculation. Let us remind that the albedo model implemented in this work relies on a full 3D approach, where the *finite-length* module casts a *finite-length* shadow onto the ground and the Sun describes a 3D path in the sky, as sketched in Figure 3.10a. In [2], although the Sun describes a 3D trajectory in the sky, the view factors are computed with a 2D strategy.

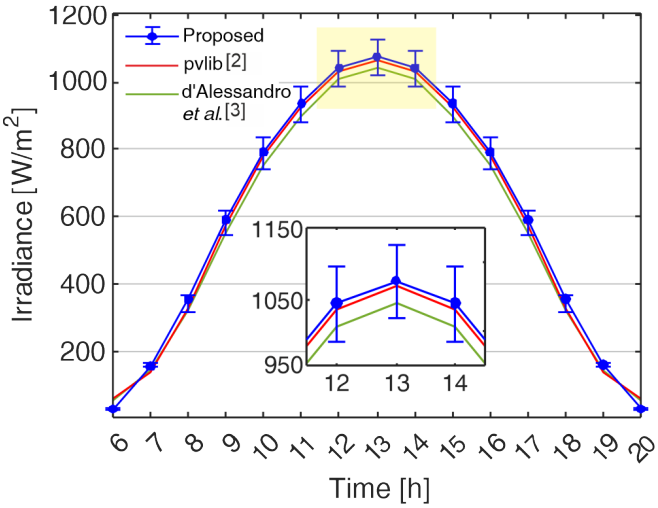

Figure 3.9. Collected irradiance of a South-oriented 30° tilted module located in Naples on June 15$^{\text{th}}$. In red the irradiance simulated in [2], in green the irradiance calculated using the irradiance model proposed by [3], and in blue the irradiance determined using the proposed approach. The blue dots represent the mean value of the set of cell irradiances whereas the blue bars indicate the maximum and the minimum values for each set.

This is equivalent to considering a 3D scenario in which the module has a *laterally-infinite length*, thereby casting an *infinite-length* shadow onto the ground (see Figure 3.10b). Therefore, the portion of shaded ground seen by the rear is larger than the realistic one predicted by our model. In [3], the direction of the Sun rays is solely defined by α and the view factors are computed in 2D. This is equivalent to considering a 3D scenario in which the Sun path is constrained within a vertical segment in front of the module and the module has an infinite length. As a result, the module tends to cast an even larger *infinite-length* shadow compared to [2] (see Figure 3.10c), further reducing the portion of unshaded ground seen by the rear.

It is worth clarifying that in the proposed 3D approach, the effect of the *finite-length* shadow plays a key role in determining the amount of albedo received by the rear. When the shadow is not aligned with the module vertical axis of symmetry, the cells receive a nonuniform albedo. In

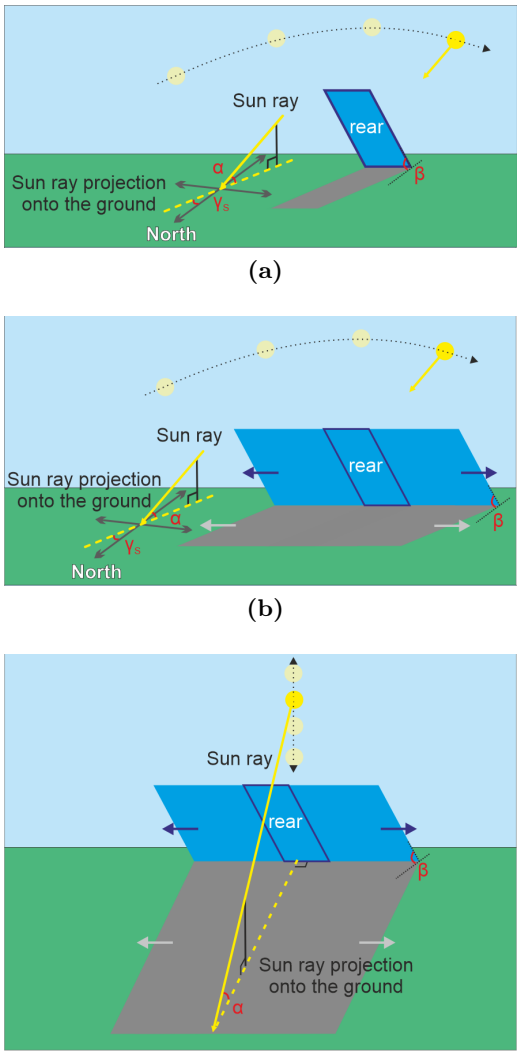

Figure 3.10. Schematic representation of the Sun-module-shadow scenario adopted by **(a)** the proposed approach **(b)** [2] and **(c)** [3] for the albedo calculation.

particular, the cells located at the edge of the module, on the side closer to

the shadow, receive less irradiance than those located at the opposite edge because they see a smaller portion of unshaded (illuminated) ground. This effect can be even extended at string level. When the shadow is not aligned with the vertical axis of symmetry, the module located at the edge, closer to the shadow side, experiences a lower albedo compared to the module at the opposite edge. Conversely, the modules located in the middle of the string receive a uniform albedo. This phenomenon is referred to as *edge effect* because it primarily affects the cells (or modules) located at the edges. A clear illustration of the edge effect can be found in Figure 3.14.
To examine the effect of the different irradiance modeling approaches on the estimation of the maximum power point, the irradiances produced by the three models are used to feed the tools for the evaluation of the I–V characteristics of the module. To perform the comparison under fair conditions, it is assumed that the module is not affected by partial shading and malfunctioning cells; this means that in [4] and [2] all the cells in the front share the same irradiance and all the cells in the rear share the same irradiance. The I–V (and thus the P–V) characteristics were simulated at different time instants along June 15^{th}. Figure 3.11 shows the generated peak power throughout the day. It is inferred that the power estimated by the proposed tool is lower than that calculated by [2] since the total output power of the module is realistically limited by the cell that receives the lowest irradiance. Conversely, the power estimated by the proposed tool is higher than the one computed by [4] thanks to the larger portion of unshaded ground seen by the rear of the PV module throughout the day. Nevertheless, the discrepancies between the proposed approach and those presented in [4], and [2] are marginal, that is, all methods provide comparable results in terms of both collected irradiance and generated power. In specific applications where the limitations of [4] and [2] have a negligible impact, these approaches remain valuable due to the lower computational cost in irradiance evaluation. For example, we suggest using [2] for simulating long PV rows in scenarios where cell-level discretization is unnecessary, such as in the absence of shadows and/or defective cells. The approach proposed in [4], thanks to its cell-level circuit-based tool, enables an accurate simulation of partial shading effects and faulty cells. Nevertheless, it should be employed only in PV installations involving long rows, where the edge effect is negligible. In scenarios involving an

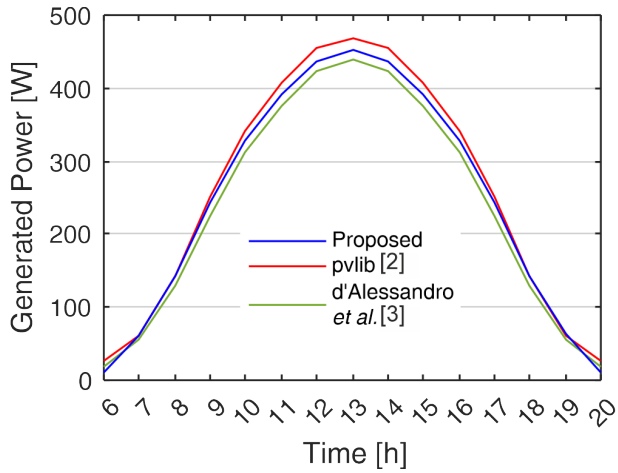

Figure 3.11. Generated power of a South-oriented 30° tilted module located in Naples on June 15$^{\text{th}}$. In red the power simulated in [2], in green the power calculated using the tool proposed by [4] and in blue the power computed by the proposed approach.

individual PV module or short PV rows, where the edge effect plays a major role, a marked albedo nonuniformity on the rear is expected, and localized shadows and/or defective cells may occur, the use of the proposed 3D tool is recommended.

3.3.3 Effects of albedo-induced mismatch on bifacial modules

In this section, simulation results aimed at evaluating the impact of albedo-induced irradiance mismatch in different bifacial installation configurations are presented. The configurations considered are the following:

1. South-oriented with $\beta = 30°$ tilt angle (S-30).
2. West-oriented with $\beta = 90°$ tilt angle (W-90).
3. Est-oriented with $\beta = 90°$ tilt angle (E-90).

The vertical configuration is widely adopted in agrivoltaics, where the bifacial module can benefit from receiving solar irradiance on both sides

throughout the day, as demonstrated in [90]. The analysis demonstrates that E-90 and W-90 configurations are inherently less sensitive to nonuniform rear-side albedo, resulting in reduced mismatch losses compared to inclined configurations. The mismatch loss is calculated as follows [**?**].

$$M_{loss}[\%] = 1 - \left(\frac{P_{cell-level}}{P_{module-level}} \right) \% \tag{3.18}$$

where $P_{cell-level}$ is the power estimated through the proposed cell-level approach and $P_{module-level}$ is the power estimated through the module-level approach defined in in the previous subsection. Figure 3.12 compares the mismatch losses of the module under study in different configurations.

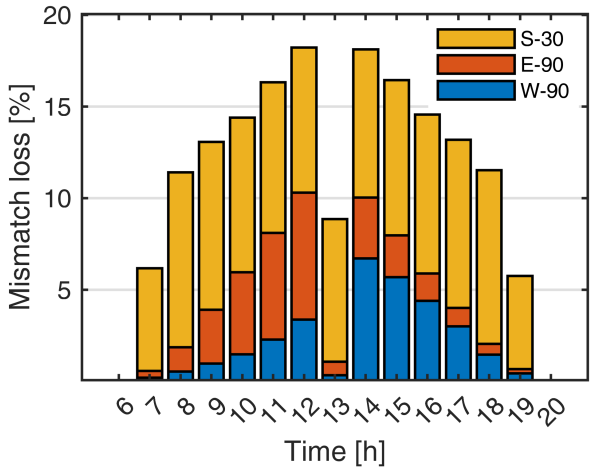

Figure 3.12. Hourly mismatch loss along a day in June for 3 different module configurations: 30° tilted south oriented module in yellow (S-30), vertical East-oriented module in red (E-90) and vertical West-oriented module in blue (W-90).

As can be seen, S-30 is affected by constant albedo-induced mismatch loss throughout the day, with a peak around noon due to the edge effect. In this condition, the cells positioned on the bottom side of the module receive only a little portion of the reflected light from the ground due to the presence of the shadow, whereas the cells positioned on the top side of the module can benefit from a larger view of the unshaded ground and

diffuse light coming from the sky. By contrast, the vertical East- and West-oriented module perform better because they benefit from a larger portion of unshaded ground throughout the day. Around noon, the module shadow is projected towards North, lying outside the module field of view. In this scenario, F_{sgnd} is negligible whereas F_{ugnd} increases, thus maximizing the albedo component of the irradiance. As highlighted in Figure 3.12, E-90 experiences significant irradiance nonuniformity in the morning, when the Sun is located due Est and the shadow is cast on the module rear. The same conditions apply for W-90, experiencing a higher mismatch loss in the afternoon.

3.3.4 Experimental validation

This section presents the experimental validation of the proposed cell-level strategy. A monofacial module has been used to emulate the rear of an inclined bifacial module with an ideally-obscured front. The experimental campaign has been carried out at the Department of Electrical Engineering and Information Technology at the University of Naples Federico II, Naples (Italy). The setup comprises a 50 W monofacial PV module ET-M54050 embedding 20 solar cells and 2 bypass diodes [91]. The PV module was mounted with the front side (*i.e.*, the emulated rear) oriented North, and tilted by β=150°, thereby facing ground as depicted in Figure 4.17. To reproduce a high-albedo scenario, a reflective white sheet was placed on the ground. The experiment was carried out by measuring the PV module I–V curves during the day through the I–V curve tracer proposed in Chapter 4. The measurements were performed on January 23^{rd}, 2025, under clear sky conditions at three different times, namely, 10:30, 12:00 and 13:30, thus resulting in different shadow configurations, as shown in Figure 3.14.

The measured I–V curves were compared to those obtained with our tool by deactivating the generated photo-currents on the front in Equation 3.4 and imposing $\varphi = 1$. As can be seen from Figure 3.14b, at 12:00 the shadow is vertically aligned with the central axis of the module. The bottom-centered cells receive less irradiance than those at the top corners due to the limited view factors to the unshaded ground, leading to an irradiance distribution similar to the one depicted in Figure 3.7b. Consequently, the I_{SC} of the entire module is limited to the photo-current generated by the least irradiated cell. It is worth noting that the two

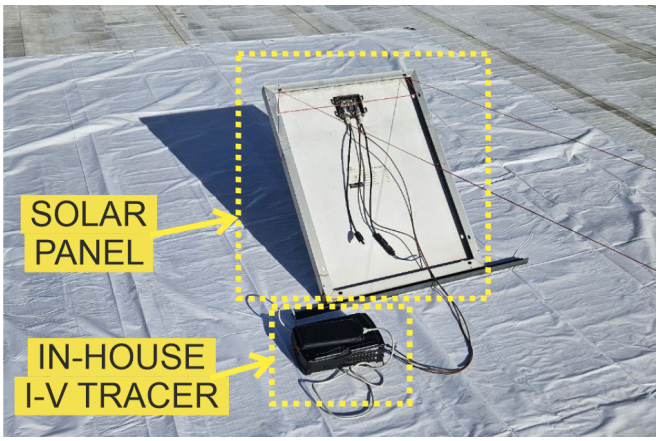

Figure 3.13. The experimental setup consists of a mono-facial PV module tilted by $\beta = 150°$ and oriented due North ($\gamma = 180°$) placed on a reflective white sheet to increase the albedo. The I–V curves are measured by means of a curve tracer prototyped in-house.

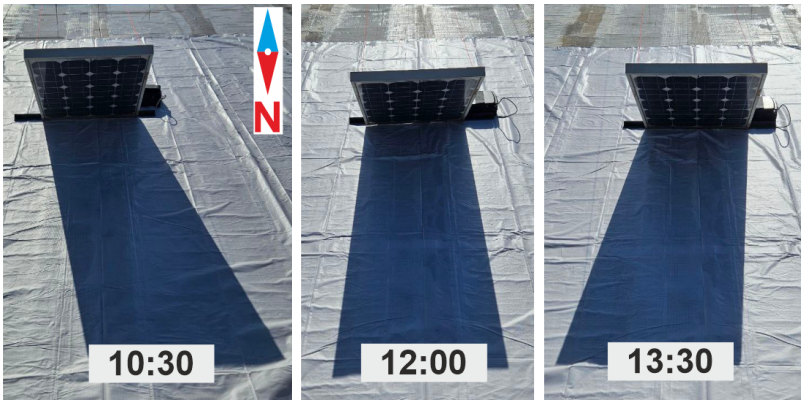

(a) **(b)** **(c)**

Figure 3.14. Shadow projections of the PV module at different times, namely **(a)** 10:30, **(b)** 12:00 and **(c)** 13:30.

submodules experience symmetrical irradiance distribution, and the I–V curve does not exhibit the typical ladder-shape occurring in case of current

mismatch between submodules and due to the action of the bypass diodes. In the early morning (see Figure 3.14a) and in the afternoon Figure 3.14c, the shadow is not aligned with the axis of symmetry of the module. In this condition, the two submodules experience a different irradiance distribution. In particular, the submodule located close to the shadow has a larger number of less-irradiated solar cells. As a result, the bypass diode protecting the weakest submodule is activated, leading to the occurrence of a ladder-shape in the I–V curve. As shown on Figure 3.15, the curves corresponding to 10:30 and 13:30 exhibit two regions at different slopes.

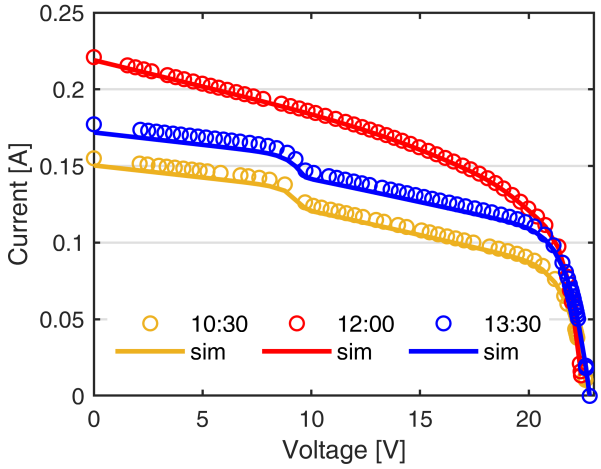

Figure 3.15. Experimental I–V curves (marked by circles) obtained at different times, namely 10:30 (yellow), 12:00 (red), and 13:30 (blue), along with the corresponding I–V curves obtained through the proposed cell-level approach (solid lines).

It is worth mentioning that the slope of the I–V curve close to the I_{SC} corresponds to the R_{SH} of the least-irradiated cell [92]. Additionally, in a module affected by mismatch, the slope of the I–V curve becomes less pronounced when the number of less-irradiated cells decreases. Accordingly, the region 0 V – 10 V corresponds to the submodule with a high number of more irradiated cells whereas the region 10 V – V_{OC} corresponds to the submodule with a small number of less irradiated cells. Simulation results show a good agreement with experimental data, with the error being lower

than 3%.

3.4 AC electrical models

The modeling of PV modules in the frequency domain has received limited attention in literature, especially when compared with the extensive body of work on individual solar cells. In this context, the impedance of a silicon solar cell is typically derived from the AC small-signal model of a p–n junction, which is well established in semiconductor device physics. The junction can be represented, in its simplest form, by a single RC-loop accounting for the junction capacitance and the associated recombination resistance [93]. Building on this foundation, most of previous studies model the ac behavior of a silicon solar cell either as a single RC-loop or a combination of multiple RC-loops, ideally an RC-loop for each material interface, to fit experimental data and capture more complex dynamic phenomena. When moving from the cell to the module level, however, the literature does not provide clear guidelines on how to scale the impedance model. State-of-the-art approaches [71, 94, 95] attempted to fit experimental data utilizing the Constant Phase Element (CPE), which introduces an experimental coefficient to represent impedance responses deviating from the one obtained considering one RC-loop. While providing mathematical flexibility, the CPE lacks clear physical interpretation because its empirical coefficient merely acts as an additional degree of freedom to fit experimental data, without any direct correlation to the physical mechanisms occurring within the solar cell. Motivated by this limitation, my research activity has focused on the development of a physically meaningful AC model for PV modules. The results presented in this section are the results of my work and have been published in [7, 5, 6].

3.4.1 Derivation of the impedance model

The dynamic behavior of a solar cell resides in the physical phenomena occurring in its structure. A standard c–Si-based solar cell typically contains a phosphorus n+ doped emitter, a boron p-doped base, a p+ doped Back Surface Field (BSF) region to reduce surface recombination, and metalized contacts on the front and back surfaces made, respectively,

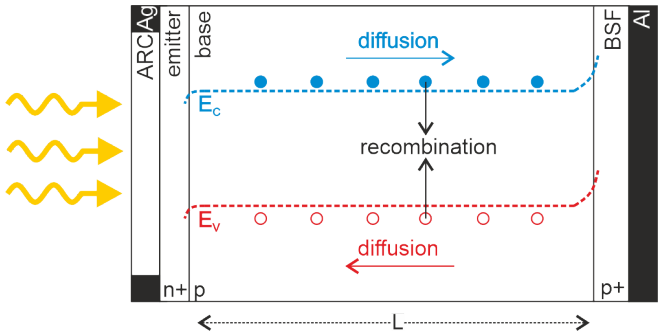

Figure 3.16. Simplified schematic representation of recombination-diffusion process in a c–Si solar cell. E_c and E_v are, respectively, the lower and upper bound of the conduction and valence bands. Reproduced from my own work [5].

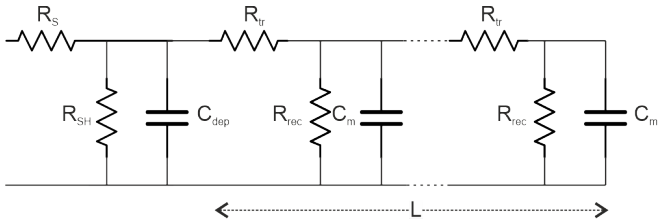

Figure 3.17. Equivalent circuit configuration of a solar cell by means of transmission line. Reproduced from my own work [5].

of silver (Ag) and aluminum (Al). The front surface of the solar cell is passivated with Anti-Reflective Coating (ARC) to reduce reflectivity. The main process governing the dynamics of a solar cell is the minority carriers' diffusion and recombination. Figure 3.16 gives a qualitative visualization of the charges' transport and bulk recombination when the cell is forward biased.

According to Bisquert [96], the process described in Figure 3.16 can be modelled by means of a transmission line with reflective boundary condition since the back contact is considered blocking. As it can be seen in Figure 3.17, the parameters R_{tr}, R_{rec}, C_m and C_{dep} are respectively, the transport resistance, the recombination resistance, the chemical capacitance, and the depletion capacitance.

From the physics of semiconductors, the following equations are derived [97]:

$$R_{tr} = \frac{L}{\sigma_n} \tag{3.19}$$

$$R_{rec} = R_{tr}\left(\frac{L}{L_n}\right)^2 \tag{3.20}$$

$$C_m = \frac{\tau_n}{R_{rec}} \tag{3.21}$$

$$C_{dep} = \frac{C_{j0}}{\sqrt{1+\frac{V+R_S \cdot I}{V_j}}} \tag{3.22}$$

where σ_n is the conductivity of the solar cell, L_n is the diffusion length, C_{j0} is the depletion capacitance at zero voltage, V_j is the built-in voltage, τ_n is the lifetime and V and I are, respectively, the voltage and current of the solar cell. The parameters R_S and R_{SH} represented in Figure 3.17 are, respectively, the series resistance and the shunt resistance. In case of long diffusion length ($R_{tr} << R_{rec}$), the model presented in Figure 3.17 is reduced to the equivalent circuit presented in Figure 3.18a. Therefore, the impedance is equivalent to a single RC-loop (see Figure 3.18b) where R_P is the parallel combination of R_{SH} and R_{rec} and C_P is the parallel combination of C_{dep} and C_m since they cannot be distinguished.
The equivalent circuit configuration presented in Figure 3.18b can be also derived from the linearization of the SDM in a specific OP, employing the SPICE model of the diode. More in detail, the resistive part accounts for the differential resistance R_D offered by the diode and it is expressed by the following equation.

$$R_D = \frac{1}{\frac{d}{dV_D}\left[I_0\left(\exp\left(\frac{V_D}{nV_T}\right)\right)-1\right]} \tag{3.23}$$

with

$$V_D = V + R_S \cdot I \tag{3.24}$$

where V_D is the voltage drop across the diode. The capacitive part is

the sum of the diffusion capacitance C_D, *i.e.*, previously defined as C_m, and the junction capacitance of the diode C_j, *i.e.*, previously defined as C_{dep}.

$$C = C_D + C_j = \frac{\tau_n}{R_D} + \frac{C_{j0}}{\left(1 - \frac{V + R_S I}{V_j}\right)^M} \tag{3.25}$$

where M is the junction coefficient ($M = 1/2$ in case of abrupt junction).

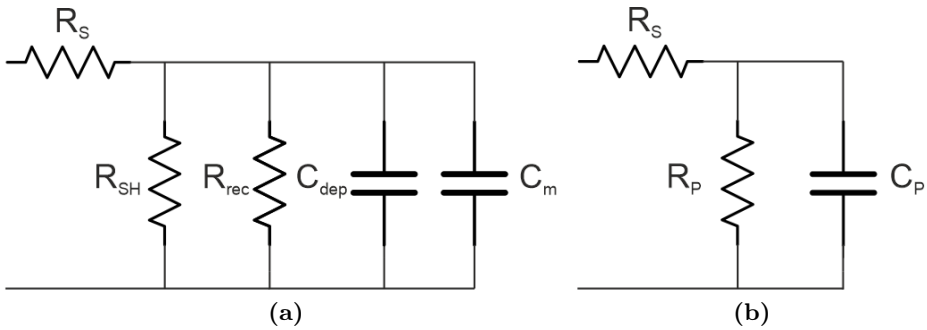

Figure 3.18. **(a)** Equivalent circuit configuration of a solar cell describing the impedance of a solar cell. **(b)** Compact model. Reproduced from my own work [5].

The generated photo-current does not depend on the frequency, therefore the current source modeling I_{PH} in Figure 3.1 can be neglected. From Figure 3.18b, the analytical expression of the complex impedance in the angular velocity domain (ω) can be expressed as follows.

$$Z(\omega) = R_S + \frac{R_P}{1 + (\omega R_P C_D)^2} - j\omega \left[\frac{C_D R_P^2}{1 + (\omega R_P C_D)^2}\right] \tag{3.26}$$

In a Nyquist diagram, Equation (3.26) is represented by a semi-circular waveform lying on the first quadrant, with a radius equal to $R_P/2$ and the center located in $(R_S + R_P/2, 0)$, as depicted in Figure 3.19.

It is useful pointing out that the derivation shown above only considers the basic structure of a solar cell and does not take into consideration

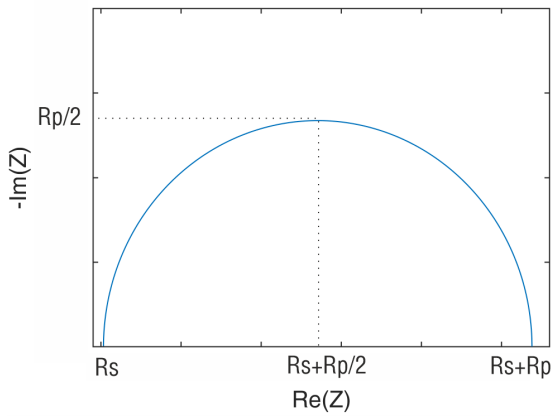

Figure 3.19. Nyquist diagram of the impedance described in Equation 3.26. Reproduced from my own work [6].

any inductive effect coming from the metallic fingers, as it is considered negligible with respect to the rest of the circuit. To prove the obtained result, the frequency response of standard c–Si based solar cell is obtained by means of a simulation environment, namely Sentaurus [98]. Sentaurus is an advanced Technology Computer Aided Design (TCAD) simulator by Synopsis providing a real description of electric devices in terms of their physical structure. The physical parameters used to simulate the solar cell is reported in Table 3.2.

Table 3.2. Doping concentration and thickness of the PV cell layers

Layer	Doping Concentration [cm^{-3}]	Thickness [µm]
Emitter (n^+)	10^{18}	0.3
Base (p)	10^{16}	180
BSF (p^+)	10^{19}	0.1

The solar cell has a surface area of 225 cm^2. Figure 3.20 report the I–V and P–V curve obtained under illuminated conditions, considering $G = 1000\ W/m^2$, global air mass of $AM = 1.5G$ and $T = 300\ K$. The AC analysis is performed in specific OP indicated by the yellow star points in Figure 3.20 using the sinusoidal voltage stimuli of 1 mV in a logarithmic-

spaced frequency range between 1 mHz and 1 GHz. As can be seen from Figure 3.21, when the DC bias is less than the maximum voltage point (see Figures 3.21a-3.21d), the impedance pattern consists of a single RC-loop, associated to the recombination mechanism, whereas as soon as the DC bias increases towards V_{OC} (see Figures 3.21e-3.21f), the impedance shows an additional arc in the high-frequency portion due to the diffusion mechanism. The transition between the recombination arc and the diffusion arc is marked by a red dashed line.

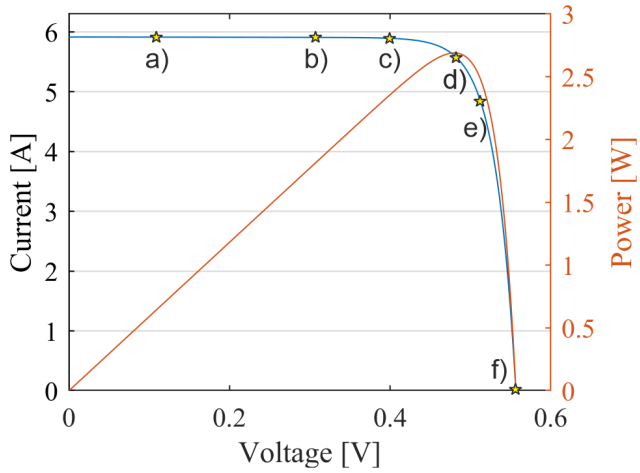

Figure 3.20. I–V curve (in blue) and the P–V curve (in red) of the illuminated solar cell. The yellow star points indicate the bias points where the Nyquist spectra are measured. Reproduced from my own work [5].

From the monitoring point of view, the MPP can be considered the best OP for the measurement of the Nyquist spectrum for the following reasons. The model that fits the experimental impedance measured in the MPP is simple because it contains only one RC-loop. The Nyquist spectrum measured towards V_{OC} presents an additional arc in the high frequency region of the spectrum, which may be mistakenly attributed to faulty conditions.

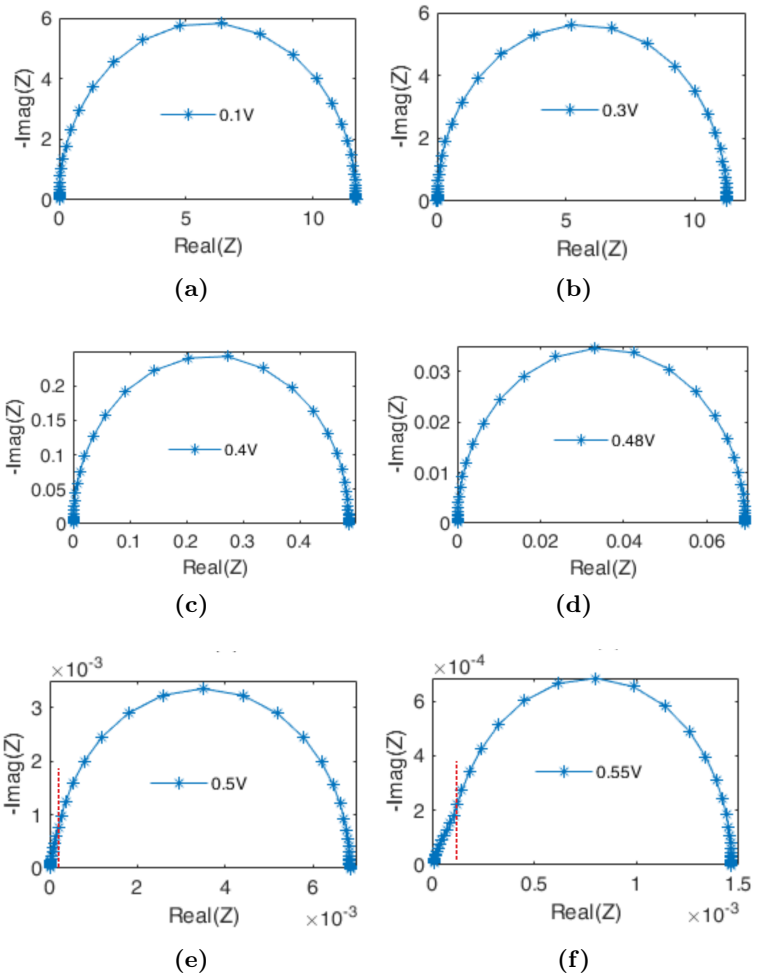

Figure 3.21. Nyquist spectra of the illuminated solar cell simulated in Sentaurus at different operating conditions: **(a)** 0.1 V, **(b)** 0.3 V, **(c)** 0.4 V, **(d)** 0.48 V, **(e)** 0.5 V and **(f)** 0.55 V. The transition between the recombination arc and the diffusion arc is marked by a red dashed line. Reproduced from my own work [5].

3.4.2 From solar cell to photovoltaic module

In a PV module made of M sub-modules with N cells each, the complex impedance is obtained as the composition of the impedances of $M \cdot N$ solar cells and M bypass diodes, leading to the following expression.

$$Z_{MOD}(\omega) = \sum_{m=1}^{M} \left[\left(\sum_{n=1}^{N} Z_{n,m}(\omega) \right) || Z_{D,m} \right] \tag{3.27}$$

where $Z_{n,m}$ is the impedance of the *n-th* cell in the *m-th* sub-module and $Z_{D,m}$ is the impedance of the bypass diode in the *m-th* sub-module. Under the assumptions that all the cells are identical and working in the same operating conditions (*i.e.*, irradiance and temperature), Equation 3.26 is still valid but the RC parameters modify as follows.

$$\begin{aligned} R_{D,mod} &= MNR_{D,cell} \\ R_{SH,mod} &= MNR_{SH,cell} \\ R_{S,mod} &= MNR_{S,cell} \\ C_{mod} &= \frac{C_{cell}}{NM} \end{aligned} \tag{3.28}$$

where the subscript *mod* indicates the global parameter while the subscript *cell* indicates the parameter corresponding to the individual cell. Moreover, since the analysis is performed on uniform irradiated PV modules, the bypass diodes protecting each sub-module are supposed to be reverse-biased, thus not substantially affecting the Nyquist spectrum. Therefore, their contribution to the overall impedance can be neglected. Based on the simulation results obtained with Sentaurus, a cell-level electric model of the PV module under test was developed in LTSPICE XVII [84] following the approach described in the previous section. The SPICE parameters of each cell were calibrated using the parameter extraction procedure applied to both the I–V curve and the impedance spectra derived from Sentaurus. For the bypass diodes, a generic Schottky diode available in the SPICE library was employed. The PV module under investigation comprises 72 series-connected cells and 3 bypass diodes. The PV module is simulated in three case studies:

(a) The PV module is healthy, *i.e.*, all the cells are identical, and it is uniformly irradiated.

(b) The PV module is healthy and partially shaded, *i.e.*, one cell within the module is shaded.

(c) The PV module is faulted, *i.e.*, one cell within the module is shunted, and uniformly irradiated.

All the spectra are measured in the global MPP.

Case (a)

When the PV module is uniformly irradiated and no mismatch is present, all the solar cells work in the same OP in terms of voltage and current. By applying Equation 3.27 and since all the bypass diodes are reverse biased, the Nyquist spectrum of the module in MPP is semicircular and it corresponds to the spectrum of Figure 3.21d multiplied by 72 (the number of solar cells embedded in the simulated PV module) (see Figure 3.22a). This corresponds to the Nyquist spectrum of a fully efficient PV module in the ideal working condition.

Case (b)

In case of partial shading, the pattern of the Nyquist spectrum is still a semicircle but with a reduced radius due to the activation of the bypass diode (see Figure 3.22d). This situation is well represented by the I–V curve of Figure 3.22c, corresponding to the presence of a small shadow partially covering a cell within the module, such as a leaf or bird dropping. In this condition, the bypass diode protecting the *m-th* shaded sub-module is active, and the following condition applies.

$$\left(Z_{D,m} || \sum_{n=1}^{N} Z_{n,m} \right) \approx Z_{D,m} = R_{D,on} \tag{3.29}$$

$$Z_{MOD} = \sum_{j=1}^{M} \left(\sum_{n=1}^{N} Z_{n,j}(\omega) \right) + R_{D,on} \tag{3.30}$$

with $j \neq m$.

Since the *m-th* bypass diode works in deep conduction mode, it shunts the impedance of the shaded sub-module. The on resistance of the bypass diode ($R_{D,ON} = 30m\Omega$) causes a horizontal shift of the PV module spectrum along the real axis. Moreover, as it can be seen from Figure 3.22d, the radius of the Nyquist spectrum is 2/3 of the Nyquist spectrum of the fully irradiated PV module, because the solar cells still work in their MPP.

Case (c)

Figure 3.22e and Figure 3.22f depicts the case of a fully irradiated PV module affected by a low shunted cell, occurring for instance in case of crack [99]. As clearly shown in Figure 3.22e, this type of fault cannot be detected on the I–V characteristics of the PV module. By contrast, the Nyquist spectrum is significantly affected, thus showing a double time constant behavior. More in detail, the simulated experiments of Figure 3.22f consists of a low shunted cell biased at 0.3 V whereas the rest of the cells are biased in their maximum operating point (0.48 V). Therefore, since the bypass diode is deactivated, the Nyquist spectrum is characterized by a low frequency arc corresponding to the low shunted cell and a high frequency arc corresponding to the rest of cells.

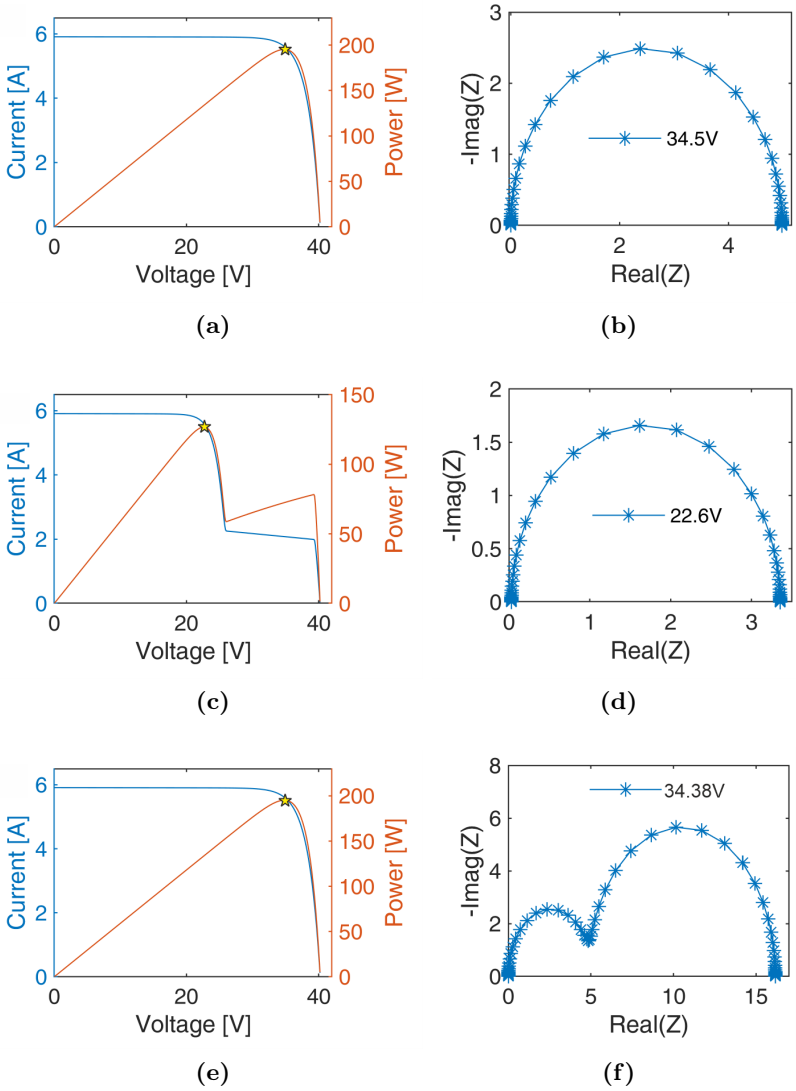

Figure 3.22. I–V curves and Nyquist spectra measured in the MPP (yellow star marker). **(a)**, **(b)**: the module is uniformly irradiated and all the cells are identical. **(c)**, **(d)**: the module is partial shaded and all the cells are identical. **(e)**, **(f)**: the module is uniformly irradiated condition and one cell is shunted. Reproduced from my own work [5].

3.4.3 Experiments

An experimental campaign has been conducted to assess the validity of the proposed impedance model. The test has been conducted on 52 W c–Si PV module [100] at the University of Salerno, employing the setup shown in Figure 3.23. The number of points acquired for measuring the impedance is 51, ranging between 10 Hz and 50 kHz.

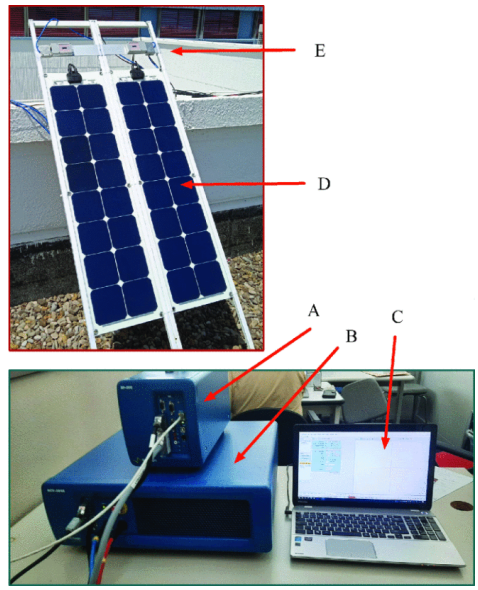

Figure 3.23. Picture of the setup arrangement, comprising SP-200 Potentiostat (A), HCV-3048 amplificator (B), EC-Lab® Software for IS (C), PV modules (D) and irradiance and temperature sensors (E). Reproduced from my own work [7].

The instruments are accommodated in a room close to a terrace where the PV module (D) is installed. The IS setup comprises the following instruments:

- Biologic SP-200 Potentiostat IS instrumentation module (A).
- Biologic HCV-3048 amplification module for high current/high voltage stimulation (B).

- Biologic EC-Lab® Software for IS for test configuration and data visualization (C).

Irradiance and the back side temperature of the module are also measured (E). The IS is performed in potentiostatic mode, which means that the measurement is based on the control of the voltage across the PV module under test, and a biased voltage equal to the MPP. The experimental campaign has provided spectra at three different levels of irradiance, namely [245 W/m^2, 535 W/m^2, 906 W/m^2] (see Figure 3.24b), and the corresponding I–V curves, depicted in Figure 3.24a. As expected, the radius of the impedance decreases with the increase of the irradiance. The IS spectrum measured under the larger level of irradiance will be indicated as curve #3.

The data are used to extract the parameters of the model proposed in Equation (3.27) solving the analytic equations describing the model, and therefore taking into consideration the minimum number of points of the spectrum. In principle, in a scenario where the IS analysis is implemented in on-board devices, this approach requires that the measurement is performed only in a few frequency points, thus allowing a reduced measurement time interval to ensure constant irradiance and temperature. As a first attempt, the measured spectrum is described considering the single RC model of Equation (3.26). In that case, the analytical procedure requires only 3 data points. The following frequency points can be chosen: $Z(\omega_0)$, $\mathrm{Z}(Z(\omega_{MAX}))$ and $Z(\omega_1)$, where ω_0 corresponds to the quasi-DC condition (*i.e.*, $\omega_0 \to 0$), ω_{MAX} is the frequency corresponding to the maximum in the imaginary part and $\omega_1$to the frequency at which the Nyquist curve reaches the zero crossing (*i.e.*, the imaginary part is null). Therefore, the analytic procedure involves the following system of equations:

$$\begin{cases} R_S + R_P \approx Z(\omega_0) \\ R_S = Z(\omega_1) \\ C_D = \frac{1}{\omega_{MAX} R_P} \end{cases} \tag{3.31}$$

The fitting curve obtained by resolving Equation (3.31) for curve #3 is reported in Figure 3.25. As it can be seen, the curve does not fit the behavior of the experimental data in the middle frequencies, and in the fourth quadrant due to the lack of the inductive part.

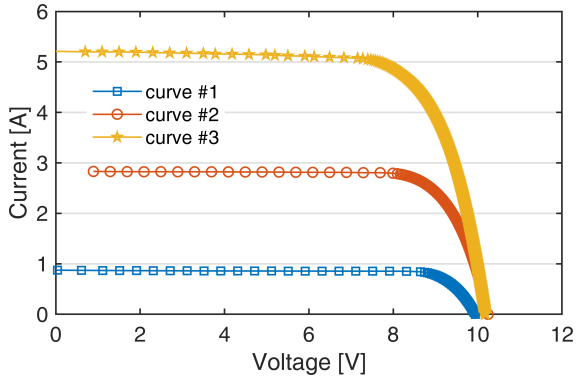

(a)

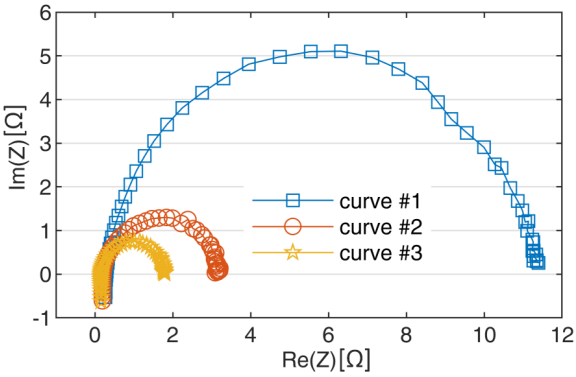

(b)

Figure 3.24. **(a)** I–V curves (reproduced from my own work [7]) and **(b)** impedance spectra measured in the MPP. Curve #1 is obtained under 245 W/m^2, curve #2 under 535 W/m^2 and curve #3 under 906 W/m^2.

This latter issue is easily solved by modeling the behavior of the cables with a constant inductance. Therefore, an additional equation must be considered:

$$L_C = \frac{C_D R_P^2}{1 + (\omega_1 R_P C_D)^2} \tag{3.32}$$

As it can be seen from Figure 3.26, the model attempts to describe the

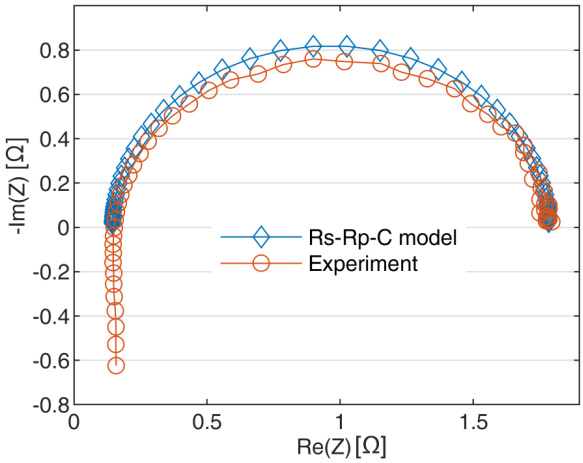

Figure 3.25. RC model fitting using analytic approach. Reproduced from my own work [7].

high frequency behavior. It is worth pointing out that the contribution of the cables is described by a constant inductance while the resistive contribution can be embedded in R_S.

Unfortunately, due to skin effect, the intrinsic resistance of the cables increases with frequency, thus not allowing the model to properly describe the experimental behaviour. For this reason, to mitigate this effect, the parameters' extraction should be performed only on a reduced frequency range. In other words, the points lying in the fourth quadrant should be discarded. A more accurate model is reported in Figure 3.27, where a double RC-loop has been considered. In fact, it is reasonable to assume that the PV module under test is made of mismatched solar cells. In this case, the analytic procedure implies the use of two additional frequency points, for a total number of 5.

The Root Mean Square Error (RMSE) between the experimental and the calculated impedance modulus is 0.02 Ω. In Table 3.3, the parameters of the proposed double RC-loop model are extracted for the three different experimental spectra, measured at three different levels of irradiance. In addition, Table 3.3 reports the temperature and level of irradiance of the PV module under test.

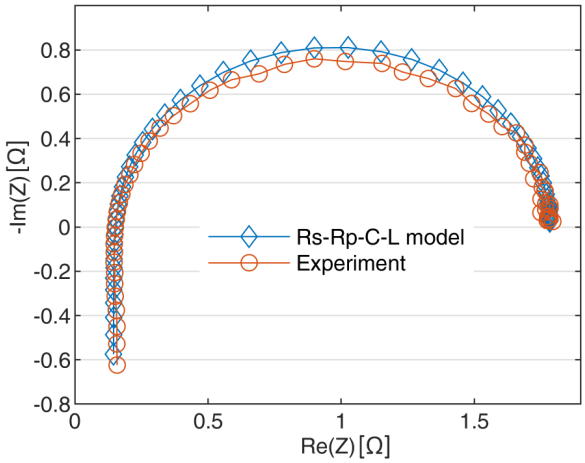

Figure 3.26. RC-L model fitting using analytic approach. Reproduced from my own work [7].

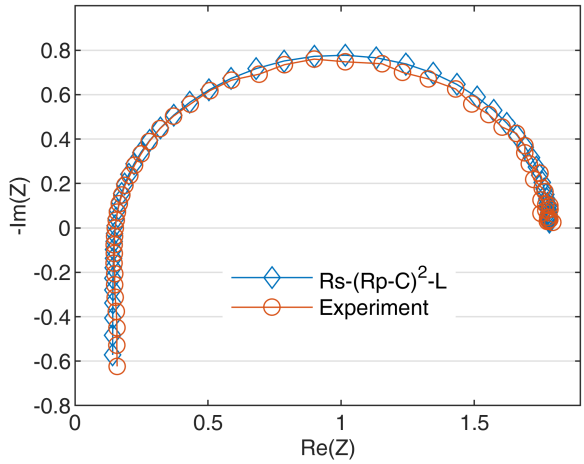

Figure 3.27. Double RC-L model fitting using analytic approach. Adapted from my own work [7].

Table 3.3. Parameters extracted using the double RC-loop impedance model.

Parameter	**Curve #1**	**Curve #2**	**Curve #3**
G [W/m^2]	245	535	906
T [°C]	23	31	42
R_S [Ω]	0.29	0.19	0.14
R_{P1} [Ω]	3.6	1.9	0.8
C_{D1} [μF]	163	189	558
R_{P2} [Ω]	7.4	1.0	0.83
C_{D2} [μF]	29	94	195
L_C [μH]	1.7	1.9	1.89

Results and discussion

The experimental results demonstrate that the dynamics of the PV module are well described by a double RC-L model. This structure provides sufficient degrees of freedom to capture the mismatch among groups of cells within the module. Although, in principle, the model could be extended to a higher number of RC-loops (ideally a RC-loop for each cell as indicated by Equation (3.27)), the results show that two loops are sufficient to achieve accurate fitting. This indicates that the module effectively behaves as if it were composed of two groups of cells operating under mismatch conditions. Furthermore, the analytical parameter extraction method, which is based on acquiring only a limited number of frequency points, enables faster IS measurements and reduces the risk of performing on-field impedance characterization while the operating conditions (irradiance and temperature) are changing. Nevertheless, this method is more sensitive to noise. A more advanced approach could exploit an optimization algorithm, *e.g.*, the differential evolution algorithm, which is capable of iteratively comparing various solutions till the optimum is found. Despite the optimization algorithm guarantees better accuracy in terms of fitting, it requires a larger number of data points to converge to the global optimum, and therefore a longer acquisition is needed. The use of the optimization algorithm for the parameters' extraction procedure is further discussed in [7, 101].

It is also important to note that the measurement accuracy is strongly affected by the influence of cables and connectors, which primarily intro-

duce a parasitic inductance. This inductive contribution becomes particularly significant at higher frequencies and can distort the impedance spectrum, giving rise to misleading features that are not related to the intrinsic behavior of the PV module. Therefore, special care must be taken in preparing the IS setup, ensuring that cable lengths are minimized. While the parasitic inductance contributes noticeably to the overall impedance response, it does not provide useful diagnostic information about the health or degradation state of the module, and should thus be carefully mitigated or compensated during measurement and data analysis.

3.5 Conclusions

This chapter presents my research work about the study and validation of DC and AC models for the description of the electric behavior of PV modules. With regard to DC modeling, I have proposed an enhanced circuit-based tool for the estimation of the energy production. The tool is based on a full 3D cell-level model for the accurate estimation of the solar irradiance, particularly optimized for the irradiance received by bifacial PV modules. This approach addresses the main limitations of existing view factor-based methods, which neglect the irradiance nonuniformity induced by the ground albedo. The cell-level circuit-based tool computes the I–V characteristic at selected time instants. It has been shown that a traditional module-level model overestimates the energy yield, as it does not account for realistic albedo-induced mismatch losses occurring on the rear side of the module. An extensive simulation comparison against state-of-the-art approaches leads to the conclusion that the proposed approach is the preferred choice when the following conditions coexist: (i) standalone modules or short row configurations, (ii) pronounced albedo-induced irradiance nonuniformity on the rear side, and (iii) localized shading and/or faulty cells. The simulation outcomes have further revealed that the mismatch loss due to albedo on the rear in tilted South-oriented bifacial modules can reach up to 8% in Summer and for high albedo values. An experimental campaign has been conducted to verify the accuracy of the proposed approach. With regard to AC modeling, an equivalent electric ac model for the characterization of c–Si based PV modules is proposed. The model is derived considering the SDM, useful for the description of a

single solar cell and confirmed by TCAD simulations. The TCAD analysis further demonstrate that from the diagnostic standpoint, the MPP is the best operating point for the measurement of the Nyquist spectrum. This analysis has been then extended to a PV module working under different realistic conditions. The AC model's parameters extraction is performed and validated on experimental data measured by a lab-grade impedance analyzer in potentiostatic mode under 3 levels of irradiance. The experimental results show that the dynamics of the PV module under test is well-described by a double RC-loop impedance.

Chapter 4

A Linear Variable Load for On-field and On-line module-level Current–Voltage curve tracing

4.1 Introduction

An I–V curve tracer is a circuit connected to the electrical terminals of the PV module to force its OP to sweep across the entire I–V characteristics, from I_{SC} to V_{OC}. In its basic form, an I–V tracer is composed of two main elements:

i. a power stage, *i.e.*, a circuit that biases the PV module, and

ii. a Data Acquisition System (DAQ) to record the PV voltage and the PV current at each OP.

The power stage is implemented through a variable load, as schematically shown in Figure 4.1a. The OP is given as the intersection between the I–V curve and the load curve ($I_{PV} = V_{PV}/R$), as graphically depicted in Figure 4.1b. By varying the value of R ideally from 0 to infinite, the entire I–V curve can be reconstructed.

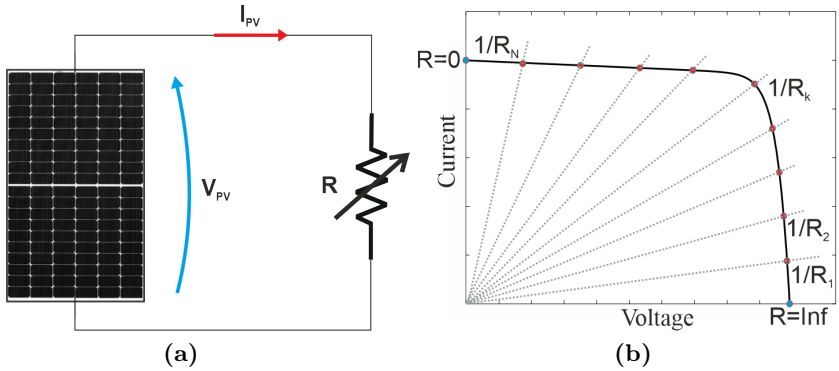

Figure 4.1. Principle of operation of an I–V curve tracer. **(a)** The PV module is connected to a variable load. **(b)** The sweeping of the OPs along the characteristics is given as the intersection between the I–V curve (solid line) of the PV module and the load curves (dotted lines) obtained with N discrete values of R, ideally ranging from 0 to ∞. Adapted from my own work [8].

In practice, the design of the variable load must meet stringent requirements to ensure meaningful and reproducible measurements. Specifically, an effective I–V tracer for outdoor testing should provide the following features:

i. quasi-static or static measurements [102],

ii. high measurement speed at controlled rate: not too fast to avoid dynamic effects, not too slow to avoid irradiance and temperature changes [103]

iii. even distribution of the points throughout the I–V curve regions to adequately capture regions at different slopes, such as in case of partial shadings,

iv. good measurement accuracy,

v. reliable operation, ensured through adequate thermal management in passive load, which must safely dissipate the power produced by the PV module during the measurement.

This chapter introduces the design and development of a portable wireless I–V curve tracer specifically tailored for module level monitoring. The system is conceived to support the fault classification and energy loss quantification tasks outlined in Chapter 2, by overcoming the shortcomings of existing solutions. The proposed I–V curve tracer embeds a variable load based on linear circuital topology and it is equipped with an innovative *disconnecting circuit* for enabling on-line I–V curve measurements, *i.e.*, the PV module is tested without interrupting the normal operation of the PV string. This chapter provides a comprehensive description of the system architecture, covering both the hardware and the control algorithm developed to handle the measurement procedure. The hardware section focuses on the implementation of the linear variable load, the disconnecting circuit, the communication module and the control unit. The control algorithm, implemented as a state machine in the control unit, appropriately sweep the OP along the I–V curve according to a decision-making logic. The performance of the proposed I–V curve tracer is then assessed through an extensive set of indoor and outdoor tests, including a direct comparison with a commercial solution used as industrial benchmark.

The work presented in this chapter is the result of my research activity carried out in collaboration with both the University of Naples "Federico II", within the framework of the PRIN 2020 research project, and the University of York. The outcomes of this work have been disseminated in the following publications [9, 1, 8].

4.2 Literature review

The variable load has been implemented in literature through different circuital approaches. They can be clustered in the following categories:

1. resistive load,
2. capacitive load,
3. active load based on DC-DC converters,
4. active load based on linear circuits (transistor-based).

In the following, the above-mentioned approaches are described in detail.

4.2.1 Resistive load

In the approaches based on variable resistive loads, the PV generator is loaded by a configurable matrix of resistors. Each configuration corresponds to a specific global resistance value and forces the PV generator in a different OP. The proper tuning of the load configuration allows to collect OPs along the whole I–V curve. As matter of example, [104] proposes a low cost I–V curve tracer based on the parallel combination of 48 different resistors and mechanical relays. Unfortunately, the number of matrix configurations are limited, and the values of the global resistance are fixed. Consequently, the IVT results in a small number of points which are not uniformly located along the I–V characteristic. Nevertheless, the approach based on variable resistance is widely used because it guarantees static and high-speed measurements. The solutions provided in [105] and [106] are indeed capable of sweeping the entire I–V curve taking each OP in 1 ms. However, an important aspect to consider is that each resistor has to be rated for the maximum PV generator power, thus resulting in an increase of the system dimension and weight. For this reason, the I–V curve tracers based on variable resistance are employed only on small power rated PV modules.

4.2.2 Capacitive load

As an alternative, [107, 108, 109, 110] proposed a simple and effective approach to perform the IVT of a PV generator, which exploits a capacitive load instead of a pure resistive one. Initially a fully discharged capacitor is connected to the generator terminals, acting as a current source (*i.e.*, it provides the I_{SC}). As the capacitor charges, the operating voltage increases while the charging current decreases. The measurement is concluded as the charging current falls to zero and the OP reaches the V_{OC}. This approach is typically implemented in commercial portable I–V tracers, thanks to its good features in terms of scalability and low specific volume and weight. This feature, in fact, permits commercial devices, such as DS-1000 [111] and PV200 [112], to measure the I–V curve of PV generators up to 100 kW . However, the amount of energy that the capacitive load stores during the measurement time interval must be dissipated on a resistive load afterward, affecting the minimum time interval between

two consecutive measurements. The capacitor charging time mainly depends on irradiation. Therefore, the capacitance must be sized to meet the standard requirements in terms of time duration [103] even in case of low irradiation level. Moreover, the capacitive approach does not ensure a static IVT since the load voltage continuously changes during the measurement, thus being affected by hysteretic effects [102]. In addition, it is not possible to reach a uniform distribution of the points along the I–V curve because, as mentioned above, the voltage slope depends on the charging current.

4.2.3 Active load based on DC-DC converters

An active load can be used instead of the above-mentioned passive ones. In particular, a DC-DC converter could be exploited to change the input resistance as function of the duty-cycle, as well explained in [113]. More in detail, the boost converter is able to show an input resistance lower than the load resistance, while the buck converter is able to increase the input resistance with respect to the load. A combination of these two features can be easily accomplished using a DC-DC converter based on buck-boost topology. The results shown in [114], demonstrate that an I–V curve tracer based on boost converter is not capable of sweeping the portion of I–V curve near the short circuit condition. By contrast, the solutions provided in [115] and [116], based respectively on Ćuk and SEPIC converters, solve this issue. Since a DC-DC converter can reach and remain in a desired OP in the I–V curve, it guarantees a quasi-static measurement. Additionally, its high dynamic behavior ensures a fast-sweeping time. On the other hand, the power switching leads to an inherent ripple in the operating voltage and current degrading the measurement accuracy. The reduction of the ripple typically requires the oversizing of reactive elements, thus affecting the size and weight of the overall system, and even the dynamics. It should be considered that DC-DC converters devoted to MPPT could be exploited to periodically perform the IVT (voltage sweep), without requiring any additional circuitry. Indeed, voltage sweep is typically implemented in commercial inverters to improve the MPPT in case of multiple maxima in the P–V curve due to mismatch. Nevertheless, the adoption of this technique for diagnostic purposes impacts on converter design. Those converters are designed to operate close to the MPP, thus

they typically exhibit a stable operation for a limited input voltage range (MPPT range) and can experience stability issues when are forced to operate in the flat region of the I–V curve. As a consequence, without a specific design [117], they merely provide incomplete [118] and not static [119] I–V curve measurement. In the last decades, several MPPT approaches have been proposed, including both low (*i.e.*, centralized and string inverters) and high (*i.e.*, distributed MPPT by means of power optimizers) granularity level techniques. As remarked in Chapter 2, only the high granularity approach is able to match all the requirements of an effective monitoring and diagnostic system. Unfortunately, optimizers are not exempt from the above-mentioned issues, likely affecting the performance in terms of classification and energy losses quantification.

4.2.4 Active load based on linear circuits

The I–V curves of a PV module can be alternatively obtained using an electronic load based on transistors operating in linear region. The solutions presented in [120, 121, 122, 123, 124] are based on the exploitation of transistors as electronic load, such as mosfet and BJT. The working point is given by the intersection between the I–V curve of the solar module and the load curve that corresponds to the I–V characteristic of the transistor at a given gate to source voltage V_{GS} [120] in case of mosfet and base to emitter voltage V_{BE} in case of BJT [122]. This solution has the great advantage of a high-speed measurement that is done in static conditions because the device can quickly modify its resistance. Unfortunately, the dependence of the operating resistance exhibited by the transistor on the control signal (*i.e.*, V_{GS} and V_{BE}) dynamically changes during the measurement time interval, thus not favoring a uniform distribution of the points along the I–V curve. To tackle this issue, a proper feedback network for the set-points in current and voltage can be employed, as presented in [124]. Moreover, it should be noted that the entire power produced by the module is dissipated by the transistor, thus requiring the need for additional heat-sinks.

4.2.5 Limitations of existing approaches

A summary of the main differences among the surveyed approaches listed in the previous subsection is reported in Table 4.1.

The table highlights the following aspects:

- most of the surveyed solutions do ensure static measurement, with the exception of those based on capacitive load;
- only the capacitive load can measure long PV strings and/or small PV array, but at cost of a significant dynamic variation in the I–V curve sweeping.
- even though the approaches based on configurable resistive matrix do ensure static measurements, they are suitable only for small power-rated PV module, *i.e.* up to 50 W, and only few points on the I–V curve can be measured;
- none of the mentioned solutions has the capability of performing on-line measurements, meaning that the IVT does require the shut-down of the PV plant and the string/array disassembly;
- the majority of the considered I–V curve tracers randomly distribute the measurement point along the I–V curve, thus reducing the detectability of partial shading events and potential faults.

4.3 Methodology and system design

Based on the outcomes of the comparative analysis presented in the previous section, the most suitable approaches for implementing a reliable I–V curve tracer are the programmable DC-DC converter and linear circuits. These two solutions exhibit static or quasi-static behavior and allow a fine control over the OP during the sweep process. However, from a metrological standpoint, linear circuits offer better performance compared to their switching-mode counterparts, mainly in terms of measurement accuracy, due to the absence of switching noise, and stability, enabling operation even on the flat region of the I–V curve. Even though the main drawback is the poor power handling capability, this aspect is far less critical since a module-level approach is adopted. In this section, the design of

Table 4.1. Comparison among different variable load approaches

Approach	Reference	Static Measurement	Sweeping Time	On-line Measurement	Power Management
Resistive Load	[104]	Yes	-	No	50 W
	[105]	Yes	1 ms/pt	No	5 W
	[106]	Yes	-	No	50 W
Capacitive Load	[107]	No	5 ms	No	235 W
	[108]	No	100 ms	No	250 W
	[109]	No	14.32 s	No	900 W
	[110]	No	20 ms	No	1.5 kW
	[111]	No	1–10 s	No	50 kW
DC/DC Converter	[114]	Yes	-	No	120 W
	[115]	Yes	208 ms	No	94 W
	[116]	Yes	1 s	No	300 W
Linear Circuit	[120]	Yes	-	No	190 W
	[121]	Yes	-	No	120 W
	[122]	Yes	-	No	51 W
	[123]	Yes	0.9 s	No	30 W
	[124]	Yes	4–10 min	No	322.5 W

a novel I–V tracer based on a linear variable load is presented. The circuit is tailored to typical PV specifications:

- Maximum $P_{\mathrm{MPP}} = 300$ W
- Maximum $V_{\mathrm{OC}} = 50$ V
- Maximum $I_{\mathrm{SC}} = 10$ A

The proposed design aims to overcome the limitations of existing approaches, thereby including innovative features:

i. it allows on-line measurement, meaning that the circuit electrically disconnects the PV module under test during the measurement whereas providing an alternative path to the string current. As a result, it guarantees continuous power flow without open-circuiting the PV string. Once the measurement is completed, the circuit automatically re-connects the PV module, restoring the normal operation of the string.

ii. The measurement time interval lasts less than 1 s, making the instrument suitable for on-field application.

iii. The circuit evenly distributes the measured points along the characteristics, improving the homogeneous data acquisition all along the curve, by means of ad-hoc control algorithm.

In the following, a detailed description of the circuit, as well as the other system components are given.

4.3.1 Linear variable load

The linear variable load allows to impose a variable current to the PV module. The amount of current that is forced to flow through the module is linearly controlled by an external variable voltage source. To better understand its working principle, consider the circuit reported in Figure 4.2. The circuit is made of two BJTs (Q_1 is PNP whereas Q_2 is NPN), a load resistor R and a pull-up resistor R_{BIAS}.

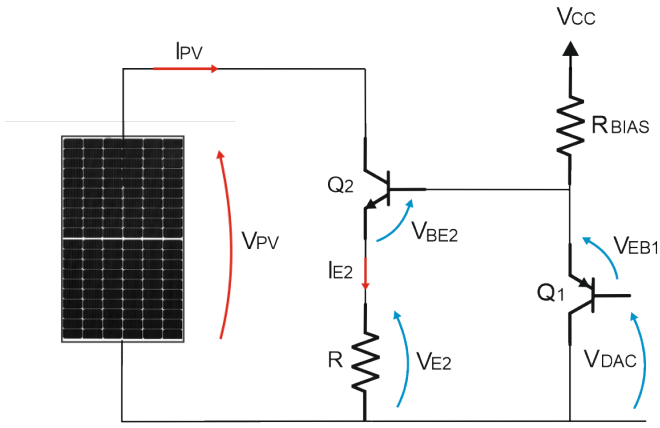

Figure 4.2. Variable load based on BJTs (Q_1 is PNP whereas Q_2 is NPN), a load resistor R and a pull-up resistor R_{BIAS}. Reproduced from my own work [9].

The current generated by the module, I_{PV}, depends on the base-collector voltage applied to Q_1, which is equal to V_{DAC}, according to Equation (4.1) obtained from the Kirchhoff voltage law.

$$V_{E2} = V_{DAC} + V_{EB1} - V_{BE2} \tag{4.1}$$

where V_{E2} is the emitter voltage of Q_2, V_{BE2} is the base-emitter voltage of Q_2 and V_{EB1} is the emitter-base voltage of Q_1.

Assuming that all the transistors are identical and working in forward active region, the voltage V_{BE2} can be considered equal to the voltage V_{EB1}. Therefore, the following equations can be inferred.

$$V_{E2} = V_{DAC} \tag{4.2}$$

$$I_{E2} = \frac{V_{E2}}{R} = \frac{V_{DAC}}{R} \tag{4.3}$$

Supposing that the forward current gain α_F is closer to 1, the emitter current can be considered equal to the collector current. Hence, the current that is forced to flow through the module (*i.e.*, I_{PV}) is linearly controlled by applying the external voltage V_{DAC}. It should be clarified that the BJTs do

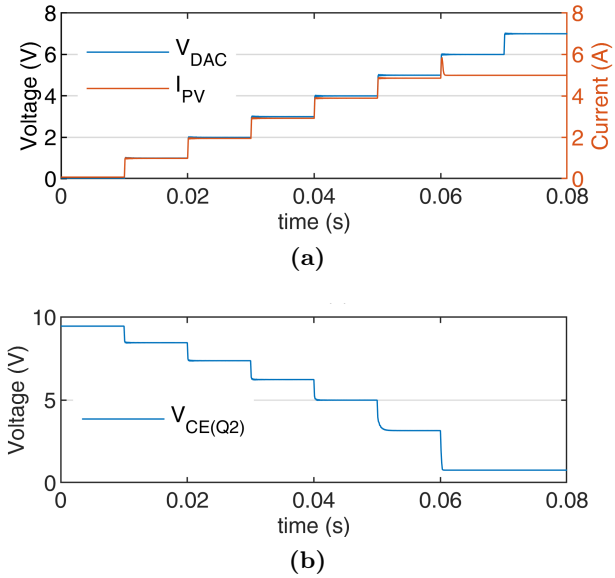

Figure 4.3. Spice simulation of the variable load shown in Figure 4.2. **(a)** The external voltage applied to the active load V_{DAC} is depicted in blue, whereas the photovoltaic current (I_{PV}) is depicted in red. **(b)** collector-emitter voltage of the NPN transistor (see Q_2 in Figure 4.2). Adapted from my own work [9].

not always work in forward active region during the I–V curve sweeping. To better explain this aspect, Figure 4.3 report the SPICE simulation results of the variable load depicted in Figure 4.2, where the BJTs are replaced with Darlington transistors due to their capability of providing higher current gain and higher input impedance. It is assumed that the PV module is uniformly irradiated with $V_{OC} = 9.6V$ and $I_{SC} = 5A$.

The load resistor R is set equal to 1Ω. In Figure 4.3a, the blue curve depicts the external voltage V_{DAC} applied to the base-collector of Q_1, whereas the red curve depicts the PV current. V_{DAC} is stepped from 0V to 7V to sweep the I–V characteristic in 8 OPs from V_{OC} to I_{SC}. In V_{OC}, Q_1 works in the active forward region whereas Q_2 is in cut-off. As V_{DAC} increases, the OP moves towards the short circuit condition and both Darlington transistors are forced to work in forward active region. As can be seen in Figure 4.3a, V_{DAC} and I_{PV} match according to Equation (4.3)

as long as V_{DAC} is less than 5V. For larger voltage, Q_2 is pushed to work within the saturation region. This condition is well shown in Figure 4.3b, where the collector-emitter voltage of Q_2 saturates at 0.768V.

As it can be deduced from Equation (4.3), the sensitivity of the proposed circuit (*i.e.*, dI_{PV}/dV_{DAC}) depends on the resistance value R. In particular, supposing that the increment in the external control voltage (ΔV_{DAC}) is constant, a high resistance value results into a small current perturbation, whereas a low resistance value corresponds to a larger current variation. To better understand how the sensitivity of the circuit proposed in Figure 4.2 impacts on the IVT, consider the black solid curve reported in Figure 4.5. This curve is a typical I–V characteristic arising from a uniform irradiated module. It consists of a vertical branch, where small voltage increments correspond to large current increments, and a horizontal branch, where large increments in the voltage result into small increments in current. Consequently, the number of measured points (red dots in Figure 4.5) could be either insufficient for scanning the horizontal branch or overabundant in the case of the vertical branch.

This is the main drawback of using the circuit in Figure 4.2. For such reasons, the circuit can be improved by incrementing the number of BJT branches, each containing a different resistance value such that I_{PV} is finely adjusted by the combination of multiple current steps. The schematic of the active load proposed in this study is reported in Figure 4.4a. As can be seen, it is formed by two Darlington branches. The I_{PV} is composed by the sum of the current that flows through Branch A (the current term I_1) and through Branch B (current term I_2). With reference to Figure 4.5, if R_1 is larger than R_2, the current steps resulting from a constant voltage increment ΔV_{DAC1} (ΔI_1) can be used to trace the vertical portion of the I–V curve, whereas the current steps imposed by ΔV_{DAC2} (ΔI_2) can be used to trace the horizontal portion. The correct operation of this circuit requires the recognition of the knee, evaluated as the slope of the I–V curve in the MPP. In fact, when the slope of the I–V curve is larger than the knee, the point to be measured lies on the vertical branch, establishing an increase of V_{DAC1}. On the contrary, when the slope of the I–V curve is smaller than the knee, V_{DAC2} must be increased whereas V_{DAC1} must be kept constant. In addition to the Darlington branches, the circuit in Figure 4.4a contains a third branch made of a single transistor T_1 for

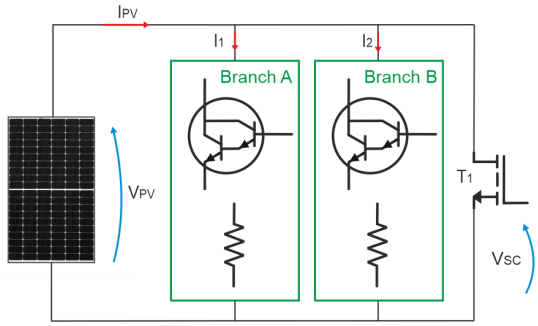

(a)

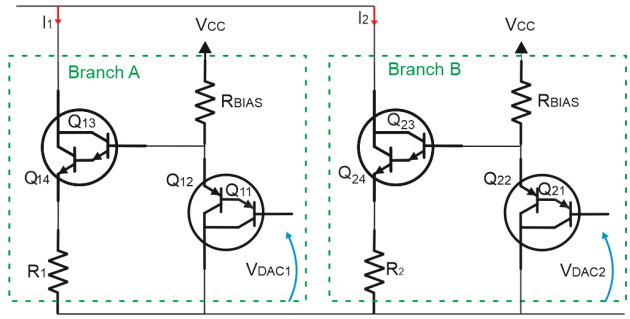

(b)

Figure 4.4. **(a)** High-level schematic circuit of the proposed variable load. It is composed of two Darlington branches, namely *Branch A* and *Branch B*, and an additional parallel branch comprising the mosfet T_1 for imposing the short circuit condition. **(b)** Breakdown of *Branch A* and *Branch B* reported in **(a)**. Reproduced from my own work [9].

the short circuit measurement. In fact, it is to be remarked that the Darlington branches reported in Figure 4.4b are not able to impose the short circuit condition due to the presence of the saturation voltage across Q_{24}. Therefore, T_1 is activated whenever the short circuit measurement must be performed.

Since the active load is a linear circuit, the entire PV power is dissipated by the circuit during the measurement time interval. The amount of power to dissipate might become concerning as the PV module rated

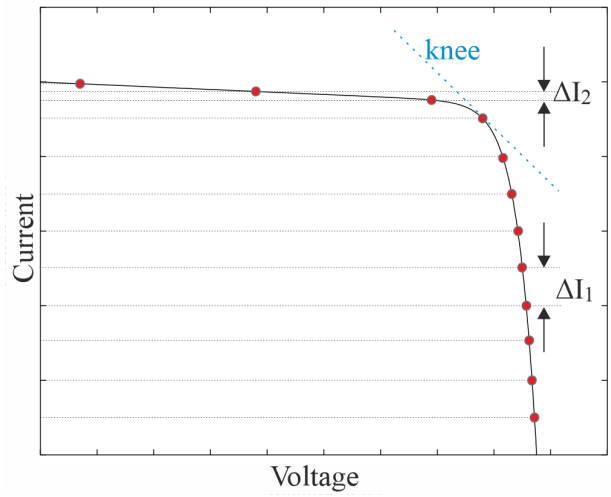

Figure 4.5. Qualitative description of the distribution of the measured OPs (red dots) acquired by the proposed I–V curve tracer. The black solid line is the I–V curve of a generic uniformly irradiated PV module. ΔI_1 is the current step imposed by *Branch A* (see Figure 4.4b), used to trace the vertical portion of the curve, whereas ΔI_2 is the current step imposed by *Branch B* (see Figure 4.4b) to trace the horizontal portion. *knee* defines the transition between the vertical and horizontal side of the I–V curve. Reproduced from my own work [9].

power increases, inducing the Darlington transistors to work outside their Safety Operating Area (SOA). A solution can be to exploit the modularity of the circuit. A single Darlington branch can be split into multiple branches whose global resistance value is equal to the desired one. As matter of example, assume a Darlington branch with $R = 1\Omega$. This latter can be obtained by parallelizing two identical Darlington branches with $R = 2\Omega$, each dissipating half of the power. This feature makes the proposed variable load a scalable solution, allowing the I–V curve tracer to handle even higher power dissipation. Nevertheless, the main drawback is the increased weight and occupied area.

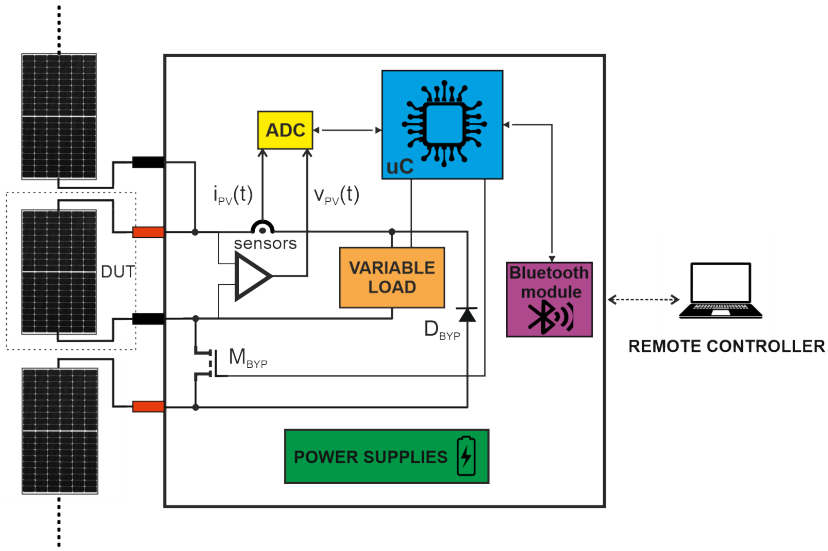

Figure 4.6. Schematic diagram of the proposed portable I–V curve tracer. The tool embeds a current and voltage sensors for measuring the PV current and PV voltage, a control unit based on MCU, a Bluetooth module, a disconnecting circuit comprising the transistor M_{BYP} and the diode D_{BYP} and a power supply section. The PV current and PV voltage are acquired by a ADC. The MCU communicates wirelessly to a remote controller. Adapted from my own work [9].

4.3.2 System architecture

The variable load under investigation is enclosed within a portable embedded tool. The tool embeds a sensing section, a control unit, a communication module, a disconnecting circuit and a power supply section. The detailed description of each section is given in the following. The system architecture of the tool is depicted in Figure 4.6.

Disconnecting circuit

Since the PV module must be disconnected from the string during the measurement, the I–V curve tracer is provided with a specific disconnecting circuit, comprising a mosfet switch M_{BYP} and a bypass diode D_{BYP}. The principle of operation is illustrated in the following. During the normal

operation (Figure 4.7a), M_{BYP} is ON, guaranteeing that the PV module under test is electrically connected to the string. In this phase, M_{BYP} acts as an almost ideal short circuit, because its ON resistance is in the order of few $m\Omega$ and both D_{BYP} and the variable load are inactive, guaranteeing that I_{PV} is equal to the string current I_S. At the start of the measurement, the control unit turns OFF M_{BYP} to electrically isolate the PV module, thus forcing the activation of D_{BYP} (Figure 4.7b). The bypass diode prevents the interruption of the I_S by creating an unimpeded path around the isolated PV module. During this period, the string keeps producing power, which is only reduced by the bypassed module's contribution. The amount of energy lost during the module disconnection depends both on the duration and the frequency of the measurement. Since the proposed I–V tracer must require less than 1 s and the number of measurements over the day is limited, the energy loss can be considered negligible. In addition, even though the activation of the disconnecting circuit causes the MPPT to run additional cycles, it does not affect the stability of the power system.

In order to prove the effectiveness of the proposed disconnecting circuit, an experimental setup has been arranged on a 1 kW PV array available at the Department of Electrical Engineering and Information Technology at the University of Naples Federico II. The tool has been connected to the terminals of the PV module under test and the terminals of the PV string as shown in Figure 4.6. The PV string has been indeed connected to a ZS electronic load. The string current I_S and the enabling signal V_D, which turns ON/OFF the disconnecting circuit, are measured by means of digital oscilloscope Tektronix DPO3034. The experiment shows that I_S, depicted in blue in Figure 4.8, keeps flowing thanks to the activation of the internal bypass diode.

The red curve, instead, represents the disconnecting signal V_D which is in charge of disconnecting the PV module under test when set to the logic low level. Finally, the green curve is the current flowing through the PV module under test, I_{PV}. As it can be seen, it reproduces the transient behavior from the open circuit condition to the short circuit condition, whereas it is equal to I_S outside the measurement window. This experiment clearly demonstrates that the proposed monitoring tool is capable of performing the IVT in less than 1 s. As already mentioned,

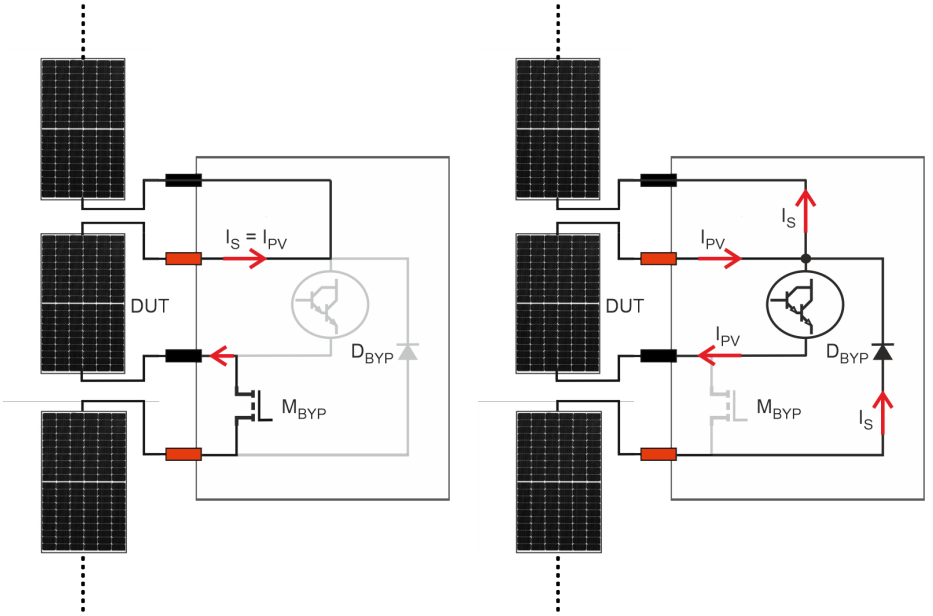

(a) **(b)**

Figure 4.7. Working principle of the disconnecting circuit. The grey color indicates the inactive components and the branches where no current is flowing. **(a)** Normal operation of the PV module embedded into the string, *i.e.*, the disconnecting circuit is inactive. In this scenario, M_{BYP} is ON, and the PV current I_{PV} corresponds to the string current I_S **(b)** During the measurement phase, the disconnecting circuit is active. M_{BYP} is turned off, thereby causing the activation of D_{BYP}. Reproduced from my own work [8].

.

this feature is required by the standard [103] to assume constant irradiance and temperature conditions.

Communication module

The wireless communication is implemented through a low-power Bluetooth module, enabling long distance communication of up to 1000 m at 18 dBm [125]. The range capability makes the proposed I–V curve tracer employable even in large PV installations. This module allows the I–V

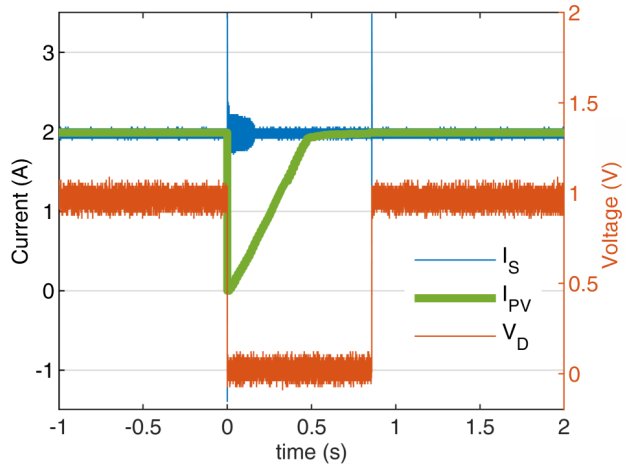

Figure 4.8. Experimental curves of the disconnecting circuit. The blue curve depicts the string current I_S, in green the PV module I_{PV} under test current is represented, whereas the red waveform is the disconnecting signal V_D. When $V_D = 1$, the disconnecting circuit is OFF and $I_{PV} = I_S$. When $V_D = 0$, the disconnecting circuit is ON, guaranteeing the continuous flow of I_S, whereas I_{PV} is forced by the variable load. Reproduced from my own work [9].

tracer to communicate with a remote controller through an ad-hoc user-friendly graphic user interface (GUI) implemented in Matlab R2022a. The Bluetooth communication is established as serial port, with a data buffer size of 1024 byte per acquisition. From the GUI, the user can establish the Bluetooth communication with the instrument, set the measurement parameters, start the measurement, visualize the data in real-time and eventually store the data either in *.m* or *.csv* format for offline processing. Optionally, the user can set the number of acquisitions for repetitive measurements and the time interval between the two consecutive acquisitions.

Control unit

The control unit is based on a MCU in charge of handling the measurement process.

1. It receives the command *start of the measurement* from the remote

controller.

2. It enables the disconnecting circuit.

3. It provides the proper signals (V_{DAC1} and V_{DAC2}) to drive the variable load using a multichannel digital to analogue converter (DAC).

4. simultaneously acquire the current sensor and voltage sensor outputs through two independent 12-bits ADCs with a sampling rate of 7 MS/s.

5. At the end of the measurement, it sends the data to a remote controller. The data are digitally filtered to remove the noise and partially processed on-chip to assure that they are acquired in static conditions.

4.3.3 Control algorithm

An innovative algorithm has been developed in order to guarantee an even distribution of the measured points along the I–V characteristic. The flowchart of the algorithm is depicted in Figure 4.9.

The proposed algorithm performs the following steps:

1. Prior measurement of I_{SC} and V_{OC}.

2. Calculation of the distance between the points along the vertical branch as

$$\Delta I_{DIST} = \frac{I_{SC}}{N/2} \tag{4.4}$$

and along the horizontal branch as

$$\Delta V_{DIST} = \frac{V_{OC}}{N/2} \tag{4.5}$$

where N is the total number of points to acquire, given as input parameter by the user. This step is performed assuming a square-shaped trace.

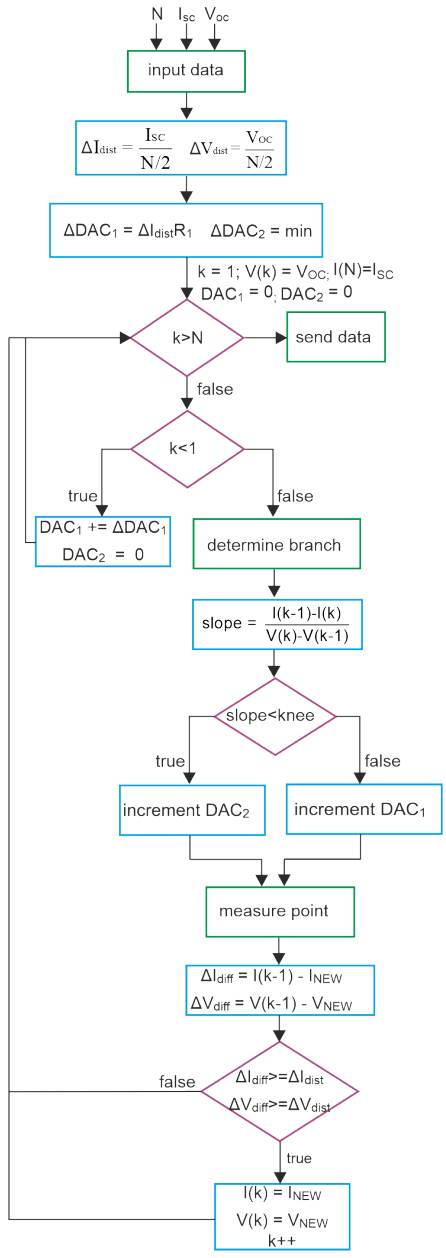

Figure 4.9. Flowchart of the control algorithm implemented in the proposed I–V curve tracer. Reproduced from my own work [1].

3. Evaluation of the voltage steps ΔV_{DAC1} corresponding to ΔI_{DIST} and imposing ΔV_{DAC2} equal to the minimum step increase.

4. Acquisition of the second measured point ($k = 2$) corresponding to $V_{DAC1} = \Delta V_{DAC1}$ and $V_{DAC1} = 0$ with the assumption that it lies on the vertical branch of the I–V characteristic. In fact, V_{OC} is stored as $k = 1$, whereas I_{SC} is stored as $k = N$.

5. Identification of the I–V branch. When a new point is acquired, it is needed to identify which Darlington branch must be increased. This task is performed by calculating the slope at the actual working point as

$$slope = \frac{I(k-1) - I(k)}{V(k) - V(k-1)} \tag{4.6}$$

where $[V(k-1), I(k-1)]$ is the data point acquired in the *(k-1)-th* iteration and $[V(k), I(k)]$ is the data point acquired in the *k-th* iteration. The slope is then compared to the value of the slope obtained at the MPP. This latter is calculated as [126]

$$knee = \frac{I_{SC}}{V_{OC}} \tag{4.7}$$

6. If *knee* is greater than *slope*, the working point lies on the horizontal curve and V_{DAC2} must be incremented, otherwise, the working point lies on the vertical curve and V_{DAC1} must be incremented.

7. Calculation of the distance between the actual point and the last one acquired. If the distance in voltage or current is less than the thresholds evaluated in point 2 (ΔI_{DIST}, ΔV_{DIST}), the point is discarded.

8. If the number of points acquired reaches N ($k = N$), the measurement procedure ends, and the control unit sends the data.

As explained, the first step of the algorithm consists in the measurement of I_{SC} and V_{OC}. The former is performed by enabling the transistor T_1 (see Figure 4.4a). On the other side, the V_{OC} is measured when

$V_{DAC1} = 0$, $V_{DAC2} = 0$ and T_1 is OFF. The measurement procedure terminates when the number of points acquired reaches the number of points N set by the user. Moreover, in case of partial shading condition, the proposed algorithm is able to detect multiple knees, assuming that the slopes are equal to the one obtained in case of uniform light condition, as calculated in Equation (4.7).

4.3.4 Prototype

The prototype of the proposed I–V curve tracer has been realized on PCB, shown in Figure 4.10a, embedded in a small plastic enclosure rated IP67, depicted in Figure 4.10b. The MCU employed in the prototype is 70 MHz clock-speed dsPIC33EP by MICROCHIP, supporting two independent 12-bit ADC modules used for the simultaneous acquisition of the PV current and PV voltage. The circuit can measure PV voltage up to 50 V employing a specific resistive voltage divider, whereas the PV current is sensed by means of a Hall-effect sensor integrated circuit (IC) placed in series with the current path of the PV module. The Hall-effect current sensor has been selected among other current sensing topologies, such as calibrated shunt resistors, because it is suitable for a wide current range (the maximum sensed current is 10 A) without introducing significant power loss, and it benefits from galvanic isolation, thus preventing signal noise as well as ground loop feedback. The data acquired by the ADC channels are digitally filtered during the acquisition thanks to a real-time moving average filter comprising 16 consecutive points, thus enhancing the SNR, and partially processed on-chip to assure that they are acquired in static conditions. The prototype is battery-powered by a 3.7 V 2050 mAh Li-Ion battery. The main components used in the prototype are listed in Table 4.2. As highlighted in Table 4.3, the total cost of the board is approximately EUR 355, and it is expected to diminish in the case of mass production. Table 4.3 clearly demonstrates the cost-effectiveness of the proposed board with respect to commercial devices, which typically rely on bulky and expensive load capacitors. All the prices are up to date as of the time of publication of this work.

Table 4.2. Key components used in the prototype of the proposed I–V curve tracer

Description	Specification	Model
MCU	16-bit, 70 MHz clock speed	DSPIC33EP256GM604-I-PT
Current Sensor	Hall-sensor IC	LEM HY 15-P
Voltage Sensor	Resistive voltage divider	-
DAC	12-bit double-channel	MCP4822-E/MS
NPN Darlington Leg 1	90 V, 50 A	MJ11032G
NPN Darlington Leg 2	100 V, 20 A	MJH6284G
PNP Darlington	60 V, 4 A	BD678
R1	1 Ω, 100 W	Ohmite TEH100M1R00FE
R2	10 Ω, 100 W	Ohmite TEH100M10R0FE
MSC	80 V, 120 A	PSMN2R8-80BS
MDISC	80 V, 120 A	PSMN2R8-80BS
DBYP	100 V, 30 A	VS-30CPQ100PBF
BT	-	LAIRD TECNOLOGIES BT740-SC
Battery	3.7 V, 2050 mAh, 7.59 Wh	-

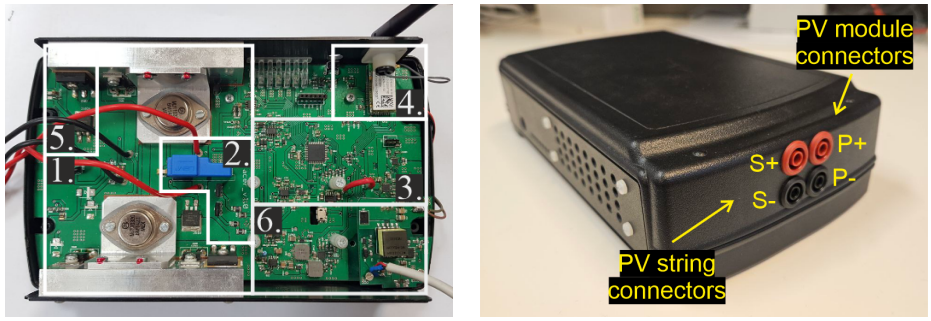

(a) **(b)**

Figure 4.10. Physical layout of the developed I–V curve tracer. **(a)** The prototype implemented on PCB. The following blocks are highlighted: 1. Variable load; 2. Sensors; 3. MCU; 4. Bluetooth module; 5. Disconnecting circuit; 6. Battery and power supply. Reproduced from my own work [9]. **(b)** IP67-rated enclosure and connectors to PV module and PV string. Reproduced from my own work [8].

4.3.5 Calibration

The calibration procedure of the I–V tracer consists of compensating the zero offset and the gain of the voltage and current sensors independently. During the procedure, the voltages V_{DAC1} and V_{DAC2} are set to 0. T_1 is deactivated during the calibration of the voltage sensor whereas it is activated during the calibration of the current sensor. For both sensors, the zero compensation requires the disconnection of the device from

Table 4.3. Economic assessment of the proposed I–V tracer against commercial devices

Device	Price (EUR)
Proposed I–V tracer	355.00
Amprobe Solar-600	2048.05
RS ISM 490A	1261.63
Seaward PV200	1720.80
DS-100C	5298.22

the PV module, thus ensuring that there is no input voltage or current applied to the sensors. The ADC readings are adjusted by a proper offset to ensure the device reads zero voltage and current. Conversely, the gain compensation consists of connecting the device input terminals to a stable source meter, such as Keithley 2000, and applying several samples within the sensors' operating range. The ADC readings are adjusted by a gain factor calculated as the slope of the calibration curve using the statistics of the least squares regression line. Due to the susceptibility of Hall-effect sensors to thermal stress [127], it is recommended to re-calibrate the instrument after a long exposure to extremely high ambient temperature.

4.4 Experimental results

In this section, the experimental validation of the proposed I–V tracer is presented. The experiments are conducted both indoor and outdoor on PV modules of distinguished technologies.

4.4.1 Performance assessment

The experiments are conducted on a c–Si 12 0Wp photovoltaic module PV-MF120EC3 [128] installed on the rooftop of the Department of Electronics at the University of Naples Federico II. The experiments have been conducted both in the case of uniform light irradiance and partial shading condition. The performance of the proposed I–V tracer is tested in terms of ability of evenly distributing the measured point along the I–V characteristics. The relative standard deviation (RSD) of the distance in voltage and current between two adjacent points is given as performance index.

Uniform irradiance condition

The first test is performed to evaluate the algorithm performance under uniform light irradiance. The experiments were repeated over the course of a day at different times in order to perform the measurement under different levels of irradiance. Additionally, the number of points N is set equal to 128 for all the acquisitions. In Figure 4.11, the results obtained under four different solar irradiance conditions are shown.

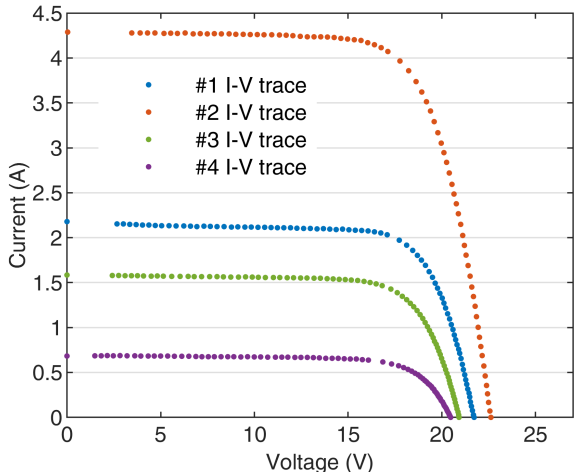

Figure 4.11. I–V characteristics measured under 4 different levels of irradiance. Reproduced from my own work [9].

All curves consist of a number of points between 75 and 81. In principle the number of points should be equal to N, which is true only in case of ideal square-shaped I–V curve. In reality, the I–V curve results in a rounded shape near the knee, causing the number of acquired data to be always less than N. Each data point shown in Figure 4.11 is the result of a mean moving average filter performed on 16 consecutive samples acquired by the ADC, aiming to increase the SNR. As preannounced, the implemented algorithm evenly distributes the measurement points on the vertical and horizontal branch. In order to understand such feature, the distances in current and voltage between adjacent samples of the I–V curve #2 are traced in Figure 4.12.

The total number of samples is 75. The red diamond points represent the distance between two adjacent current points while the black square points represent the voltage difference between two adjacent points. The I–V characteristic is acquired starting from the open circuit condition, hence the first 37 samples correspond to the vertical branch. If the red points are considered, the mean value and the standard deviation of the difference between two consecutive points is, respectively, equal to 0.11 A and 0.008 A in the yellow region, resulting in a relative standard deviation

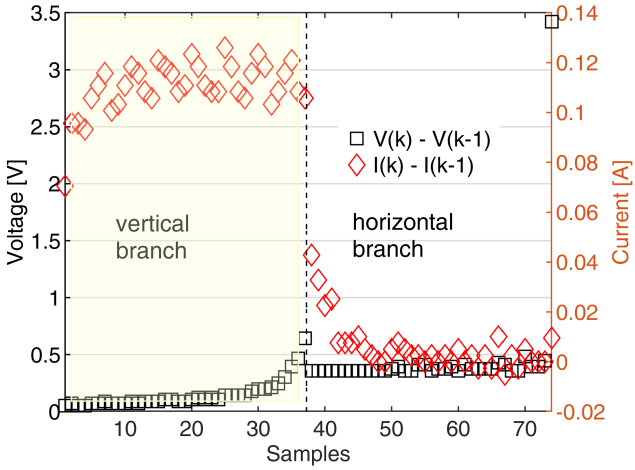

Figure 4.12. Distribution of the sampled points under uniform irradiance. The red points represent the difference between the *k-th* current sample and the *(k-1)-th* current sample, whereas the black points represent the difference between the *(k-1)-th* voltage sample and the *k-th* voltage sample, with $k = 1..N$. The light yellow region delimits the vertical branch of the I–V, whereas the white region delimits the horizontal branch of the I–V. Reproduced from my own work [9].

of less than 10%. Similar considerations can be applied to the black points lying in the white region. The mean value and the standard deviation of the distance in voltage between two adjacent samples is, respectively, 0.38 V and 0.029 V. Therefore, the RSD is roughly equal to 7%. The mean value μ and the standard deviation σ of the points depicted in Figure 4.12 are collected in Table 4.4 and Table 4.5. As it can be seen in Figure 4.11, the I–V curves are characterized by a lack of points near I_{SC}. In fact, given the value of the resistance R_2 in Figure 4.4, the minimum measured voltage V_{MIN} (*i.e.*, the nearest point towards I_{SC}) is given by the intersection between the load curve of equation $I = (V - V_{ce,sat})/R_2$ and the I–V curve (corresponding to $V_{MIN} = R_2 I_{SC} + V_{ce,sat}$). Nevertheless, such property does not lead to lack of information thanks to a linear trend of the I–V curve near I_{SC}. In Figure 4.11, the minimum voltage measured on the purple curve (curve #4) is closer to the short circuit point with respect

to the others due to its lower I_{SC}. In addition, the value of R_2 affects the minimum measurable slope on the horizontal branch and it should be chosen equal to the value that causes a current variation at least equal to the ADC resolution.

Table 4.4. Distribution of the current points along the I–V curve in uniform irradiance conditions.

I–V Branch	μ **[A]**	σ **[A]**
Vertical	0.11	0.008
Horizontal	0.0028	0.0039

Table 4.5. Distribution of the voltage points along the I–V curve in uniform irradiance conditions.

I–V Branch	μ **[V]**	σ **[V]**
Vertical	0.14	0.093
Horizontal	0.38	0.029

Partial shading condition

In Figure 4.13, an example of data measured under partial shading is plotted. This condition is obtained partially shading some cells of the PV module under test to create small and localized shadows. The patterns are compatible with those projected by environmental obstacles usually present on the rooftop of the buildings, such as chimneys and antennas. Small-area shadows are indeed considered to be the worst shading scenario, leading to marked yield reduction [129]. As it can be seen in Figure 4.13, due to the presence of the localized shadow, the current drastically drops from I_{SC} to 1.6 A when the voltage is around 10 V, corresponding to the point where the bypass diode is deactivated. Moreover, it can be easily induced from the shown I–V curve that the PV module is composed of two sub-modules, each protected by a bypass diode. Also under shaded conditions, the proposed algorithm is able to evenly distribute the measured points. As in the case of uniform condition, the data points are the re-

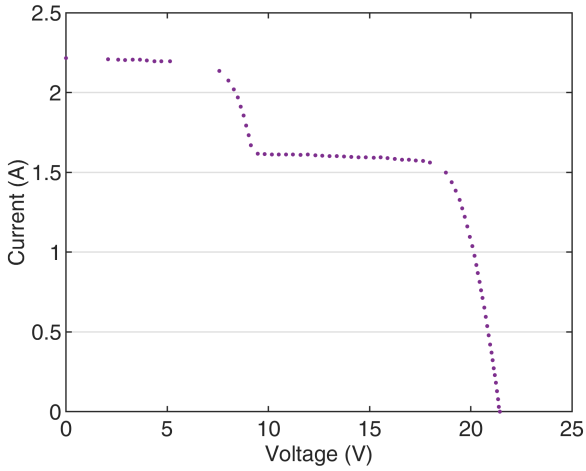

Figure 4.13. I–V acquisition under partial shadowing condition.

sults of a mean moving average filter performed on 16 consecutive samples acquired by the ADC. In Figure 4.14, the black square points represent the distance in voltage between two adjacent points and the red diamond points depict the distance in current between two consecutive measured points. The yellow zones highlight the regions corresponding to the vertical branches, while the white ones correspond to the horizontal branches.

As it shown in Figure 4.14, the points representing the distance in voltage are distributed around 0.35 V in both the white regions with a standard deviation equal to 0.019 V, whereas the mean value of the distance in current is 0.055 A in the yellow shaded regions, with a standard deviation equal to 0.0053 A. In both cases, as already proven under uniform irradiance conditions, the relative standard deviation is less than 10%. The mean values and the standard deviations evaluated in the vertical and horizontal branches are reported in Table 4.6 and Table 4.7. It is worth to observe the lack of points near the local MPP in Figure 4.13, corresponding to the range of voltage between 5 V and 7 V approximately. Such a feature is caused by the assumption that the slope of the I–V curve in the MPP is the same both in uniform and partial shading condition. Therefore, the value obtained from Equation (4.7) results in being underestimated in case of uniform light irradiance and over-estimated in case

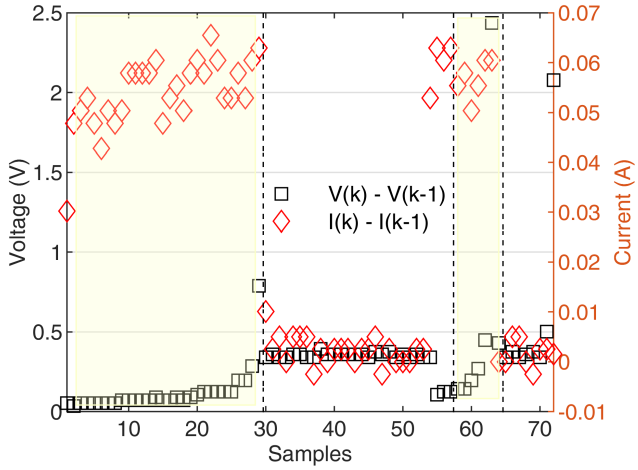

Figure 4.14. Distribution of the sampled points under partial shading. The red points represent the difference between the *k-th* current sample and the *(k-1)-th* current sample, whereas the black points represent the difference between the *(k-1)-th* voltage sample and the *k-th* voltage sample, with $k = 1..N$. The light yellow region delimits the vertical branch of the I–V, whereas the white region delimits the horizontal branch of the I–V. Reproduced from my own work [9].

of partial shading. Hence, in the latter condition, where only a limiting number of solar cells are responsible of the photo-generation, the knees in the I–V plane results to be sharper with respect to the uniform light condition, thus causing an inaccurate recognition of the I–V branch.

Table 4.6. Distribution of the current points along the I–V curve in partial shading conditions.

I–V Branch	μ **[A]**	σ **[A]**
Vertical	0.055	0.0053
Horizontal	0.0021	0.0027

Table 4.7. Distribution of the voltage points along the I–V curve in partial shading conditions.

I–V Branch	μ [V]	σ [V]
Vertical	0.12	0.082
Horizontal	0.35	0.019

Precision and reproducibility

To further assess the performance of the proposed I–V tracer, the precision of measurements across various levels of irradiance is also investigated. The irradiance levels spanned from 100 W/m^2 to 900 W/m^2, covering a range from low to high solar irradiance conditions. For each irradiance level, 10 samples of both V_{OC} and I_{SC} from the PV module have been collected. Figure 4.15 presents the collected samples, with each set centered around their μ. The black error bars indicate the σ, which serves as a measure of precision. The precision for the V_{OC} measurements was determined to be 0.08 V in the worst case, indicating a low degree of data dispersion around the mean value. For the I_{SC} measurements, the precision was 0.0046 A, reflecting a high level of consistency. Similarly, the reproducibility of the measurements, expressed as the coefficient of variation $CV = \sigma/\mu$, was found to be 0.36% for V_{OC}, while for I_{SC} it was 1.24%.

4.4.2 Comparison with benchmark

The main advantage provided by the proposed solution is the capability of accurately tracing the I–V curve under partial shading condition. To further demonstrate its efficacy, the I–V tracer is compared against the Seaward PV200 I–V curve testing kit. The comparative analysis has been performed at the Laboratory of Photovoltaics, University of York, UK, where a diverse array of PV modules with distinct technologies and configurations have been selected. This suite included both bifacial and mono-facial PV modules. The bifacial suite includes innovative HJT modules, notable for their hybrid structure combining mono–Si and a–Si layers, offering high efficiency and the ability to harness light from both sides of

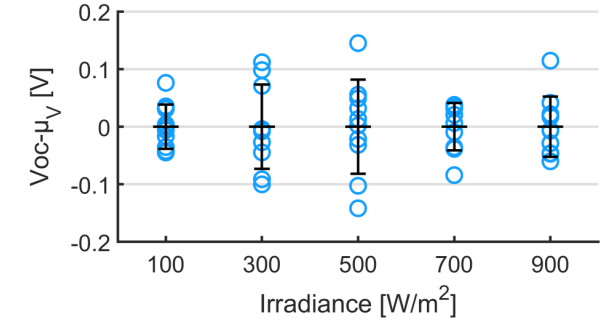

(a)

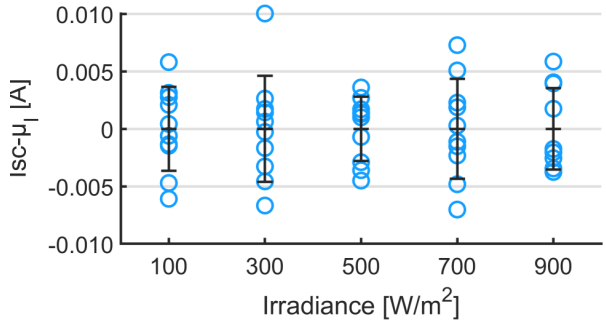

(b)

Figure 4.15. Precision measured as dispersion of the samples centered around their mean values (blue circles) at various irradiance levels for a) V_{OC} and b) I_{SC}. The black error bars indicate the standard deviation. Reproduced from my own work [1].

the module. Equally on the test bench were N-type mono–Si modules, revered for their pure crystalline structure and substantial power output, marking them as a standard for high-efficiency solar solutions, as well as flexible mono–Si modules, which defy the rigidity of traditional modules and open avenues for novel applications. a–Si thin film modules were also a subject of examination, challenging the common efficiency limitations of thin film PV technologies with their surprisingly high-performance metrics.

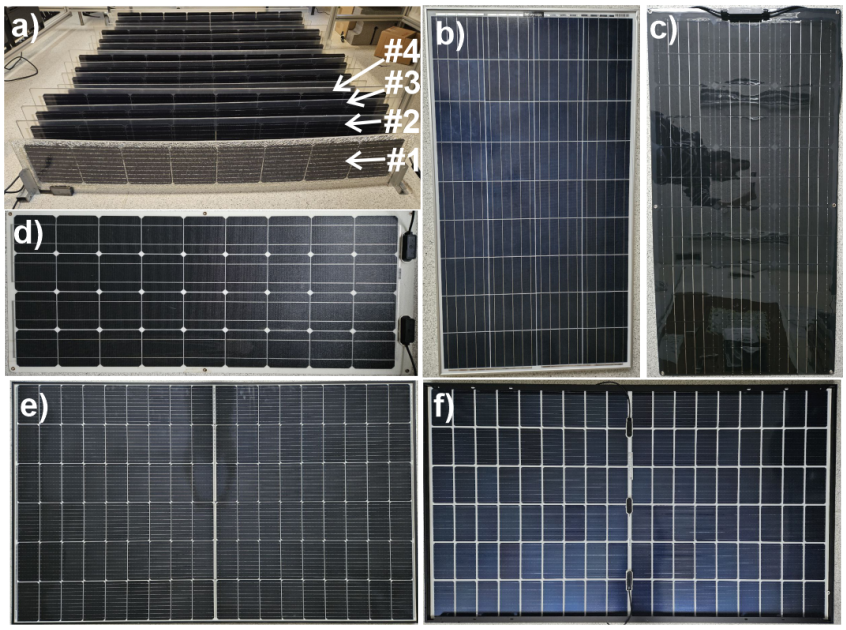

Figure 4.16. Tested modules. a) 4 HJT bifacial vertical frames numerically labelled from #1 to #4 stacked up on each other. Each frame comprises 4 rows, b) poly–Si PV module, c) a–Si thin film module, d) Flexible mono–Si module, e) front side, f) back side of the N-type mono–Si bifacial module. Reproduced from my own work [1].

Lastly, poly–Si modules were incorporated into the study to represent the most prevalent and economically accessible technology in the solar market. The tested PV modules are shown in Figure 4.16.

A total of 8 PV modules were evaluated, one for each technology mentioned in Table 4.8 except for the bifacial modules. In more details, for the vertical HJT bifacial technology, 4 frames were examined, comprising 4 rows per frame. 1 frame out of 4 (labelled as #1) has shattered glass on the front row, as shown in Figure 4.16(a). The fixed N-type mono–Si bifacial modules is tested twice to acquire the independent I–V curves for each side. Figure 4.16(e) and Figure 4.16(f) show, respectively, the front and the back side of the module.

The IVT is performed indoor by means of an effective solar simulator composed of 3 LED light sources (300 W and 42000 lm each) as shown in

Table 4.8. Summary of examined PV modules used to test the proposed I–V tracer. The reported electrical parameters refer to STC.

	HJT (mono–Si + a–Si)	**N-type mono–Si**	**mono–Si**	**a–Si Thin Film**	**poly–Si**
Module Configuration	Vertical	Fixed	Flexible	Flexible	Fixed
Monofacial vs Bifacial	Bifacial	Bifacial	Monofacial	Monofacial	Monofacial
Type	Glass/Glass	Glass/Backsheet	–	–	–
Backsheet Type	n/a	Polyethylene	–	–	–
$P_{\mathbf{MPP}}$ **[W]**	165	415	100	100	120
$V_{\mathbf{OC}}$ **[V]**	23.2	37.67	22.5	23.75	22
$I_{\mathbf{SC}}$ **[A]**	9.2	13.95	5.75	5.5	7.93
$V_{\mathbf{MPP}}$ **[V]**	19.4	31.81	18.9	19.8	17.5
$I_{\mathbf{MPP}}$ **[A]**	8.5	13.05	5.29	5.0	6.98
Module Efficiency [%]	22.3	21.3	19.2	23.0	17.0
Tier	Tier 1	Tier 1	Tier 1	Tier 1	Tier 1

the photograph of Figure 4.17. The PV modules under test are positioned vertically in front of the solar simulator to maximize the incident power density on the modules' surface. The indoor experiments are conducted in a controlled environment, thus ensuring the repeatability of the measurement. In fact, each experiment is replicated twice to capture the I–V characteristics from both the benchmark and the proposed I–V tracer (see red box in Figure 4.17) at the same irradiance and ambient temperature. By contrast, testing outdoor would introduce a higher degree of variability, thus affecting the consistency of the measurements. The developed I–V tracer receives the commands and send the data wirelessly to a laptop trough an ad-hoc Matlab script.

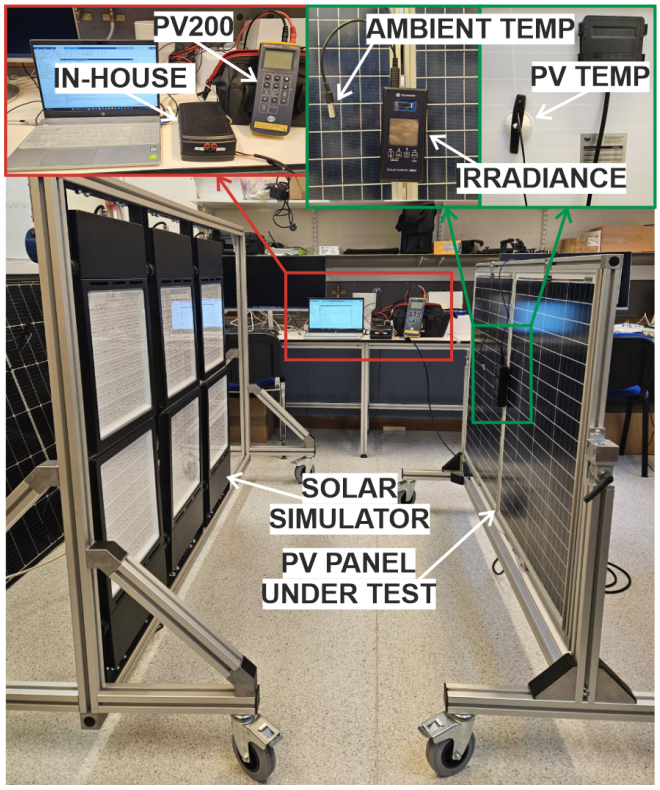

Figure 4.17. Setup of the indoor PV test. Reproduced from my own work [1].

As shown in the green boxes of Figure 4.17, the Solar Survey 200R is used as auxiliary tool to gauge the incident irradiance, ambient temperature, and PV module temperature. The experiments are conducted in non-uniformity for multiple reasons. Firstly, the PV modules installed in power plants usually experience non-uniformity because of environmental factors including soiling, bird droppings, and partial shadowing from other PV modules nearby. Secondly, the acquisition of the I–V characteristic of a non-uniformly irradiated PV module helps in showcasing the improvements in terms of quality of the measurement achieved by the developed I–V tracer in contrast with the benchmark. It is well-known that the I–V curve of a non-uniformly irradiated PV module exhibits multipleMPPs, thus representing the activation of the internal bypass diodes. If the quality of the measurement is inadequate, these events might be unobserved, thus resulting in an unreliable and misleading monitoring analysis. Consequently, the accuracy with which these events are detecting can be used as performance index. The I–V curves obtained from both the proposed I–V curve tracer and the benchmark are plotted at 1000 W/m^2 at 25 °C employing the correction procedure reported in [58]. In each I–V acquisition, the absolute MPP is highlighted, enabling easy identification and comparison of this critical parameter. In addition to visual comparison, the comparative analysis is quantified by analyzing the absolute relative error associated with key points on each I–V characteristic. Four significant points are considered for this evaluation: V_{OC}, I_{SC}, the voltage at MPP (V_{MPP}), and the current at MPP (I_{MPP}). Finally, the mean error value (ME), by means of Equation (4.8), is calculated accounting for all the measurements. The ME is a measure of errors between paired observation expressing the same quantity (*e.g.*, voltage or current). The ME gives an average of how large the errors are in a set of predictions, considering the direction of the errors (positive or negative).

$$ME = \frac{1}{n}\sum_{i=1}^{n}(y_i - x_i) \tag{4.8}$$

where n is the number of observations, y_i is the actual value (our I–V curve tracer) of the i-th observation and x_i is the predicted value (PV200) for the i-th observation.

The I–V curves from the proposed I–V tracer are depicted in blue

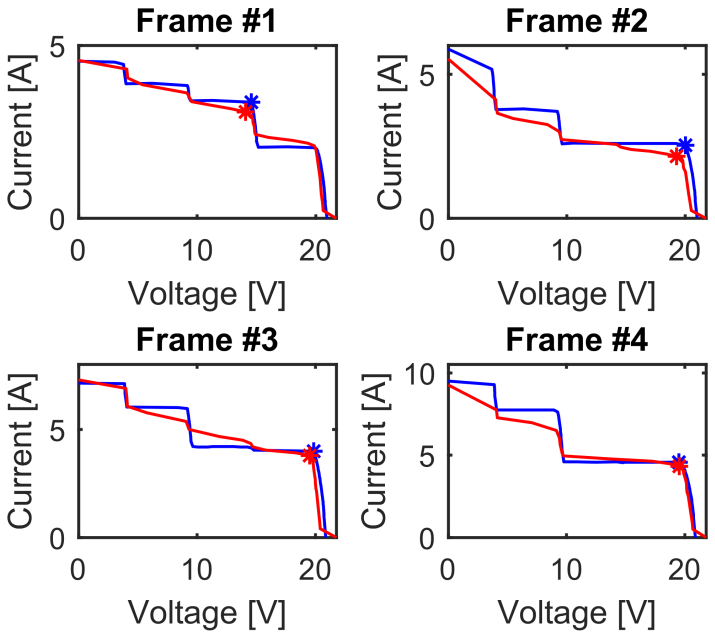

Figure 4.18. The I–V curves of the tested vertical HJT bifacial frames measured by the proposed I–V tracer (plotted in blue) and the PV200 (plotted in red). The absolute MPPs are highlighted by star markers of the corresponding colour. Reproduced from my own work [1].

whereas those from the PV200 are shown in red. In each plot, the absolute MPP is indicated by star markers of the corresponding colour. Figure 4.18 reports the I–V curves of the HJT bifacial vertical frames.

From a preliminary examination of the Figure 4.18, it can be observed that the curves taken from PV200, and the I–V tracer yield nearly identical values of V_{OC} and I_{SC} for all the frames with a relative error of less than 4% and 2.5%, respectively. On the other hand, the performance in capturing the MPPs is inconsistent among the frames. The discrepancy in the MPP is well significant in Frame #2 and Frame #3 in terms of I_{MPP}, with a relative error of almost 17%. This result can be explained in terms of quality of the measurement offered by both the instruments. The proposed I–V tracer accurately capture the steepness of the I–V curve around the

MPPs, facilitating clear detection of the current steps and, hence, the bypass diode activation events. Conversely, PV200's smoothing effect on the curves, likely due to fluctuating voltage across the capacitive load, results in loss of valuable information from the monitoring point of view, as well as an erroneous quantification of the MPP.

Figure 4.19 reports the I–V curves obtained by irradiating each side of the N-type mono–Si bifacial module independently. As in the previous technology, the I_{SC} values taken from both instruments show a perfect match with a relative error even less than 1% whereas the relative error in capturing the V_{OC} is around 1.5%.

Regarding the MPP, the proposed I–V tracer showcases that the PV module under test can yield a larger MPPs than the one measured by the PV200, with a discrepancy of up to 7% for the V_{MPP} and 5% for the I_{MPP}. This result is likely due to the capability of the proposed I–V tracer to accurately detect the steepness of the curve around the knees, without suffering from the smoothing effect as in the case of PV200. Additionally, it is worth noting that PV200 fails to properly detect the ladder-shape pattern in the I–V curves, displaying only a straight line in the horizontal region. By contrast, the proposed I–V tracer accurately identifies these steps, offering a clear depiction of the module operational condition.

The I–V curves of the remaining PV modules, namely flexible mono–Si, a–Si thin film module and poly–Si, are reported in Figure 4.20. To better visualize the comparative analysis between the proposed I–V tracer and the benchmark, the I–V curves are plotted in terms of the effective measurement points acquired by the two instruments, indicated by red dots for PV200 and blue dots for the I–V tracer. As it can be seen, the main advantage of the proposed I–V tracer is the capability of evenly distributing the OPs along the I–V curve, as discussed in the previous section.

The maximum resolutions, accounting for the maximum ratings ($V_{OC} = 50V$ and $I_{SC} = 10A$), of the proposed I–V tracer is 0.15 A for the current points and 0.62 V for the voltage points. Conversely, since the commercial devices are based on capacitive load, as PV200, they randomly distribute the measurement points with higher density closer to the MPPs and only a few points on the flat zone of the characteristics (see the red plots in Figure 4.20). Consequently, the effective current and voltage resolutions are unpredictable. The comparative analysis carried out

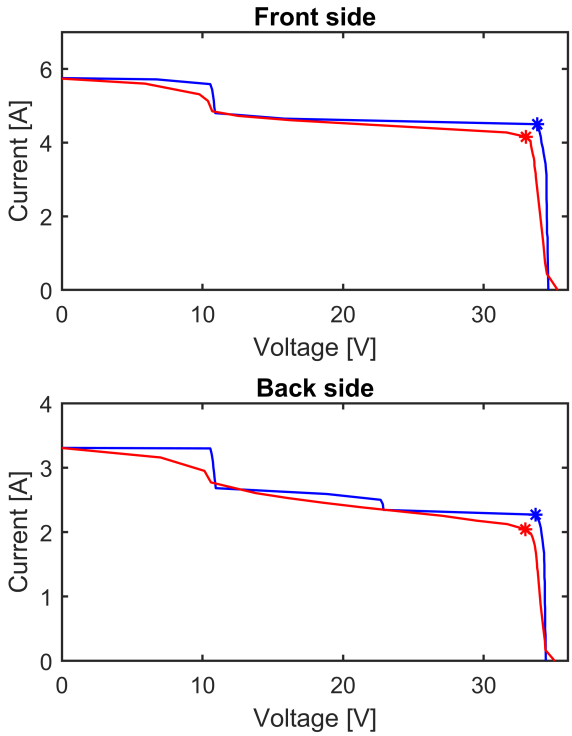

Figure 4.19. The I–V curves of the tested N-type Mono-Si bifacial module measured by the proposed I–V tracer (plotted in blue) and the PV200 (plotted in red). The absolute maximum power points are marked by star points of the corresponding colour. Reproduced from my own work [1].

in this section can be summarized considering the ME calculated as in Equation (4.8). Table 4.9 shows the obtained values in each key-point of the I–V curve.

Table 4.9 suggests that PV200 underestimate the absolute MPPs, exhibiting a positive ME both in current (0.21 A) and voltage (0.08 V). The ME on the V_{OC} and I_{SC} are also indication of the accuracy of our instrument, corresponding to 98.7% for the voltage measurement and 99.2% for the current measurement.

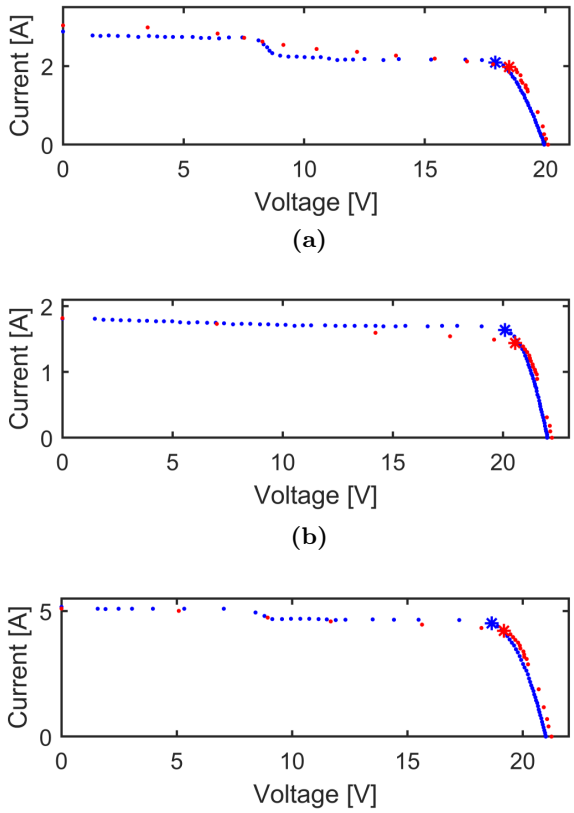

Figure 4.20. The I–V curves of the tested. **(a)** mono–Si module, **(b)** a–Si thin module, **(c)** poly–Si module, measured by the proposed I–V tracer (plotted in blue) and the PV200 (plotted in red). The absolute maximum power points are marked by star points of the corresponding colour. Reproduced from my own work [1].

4.4.3 Outdoor characterization

To further assess the performance of the proposed I–V tracer, the PV modules of Table 4.8 have been also tested in outdoor conditions, with the

Table 4.9. Mean error for each key point of the I–V curve.

Parameter	ME
V_{OC} [V]	−0.62
I_{SC} [A]	+0.04
V_{MPP} [V]	+0.08
I_{MPP} [A]	+0.21

solely exception of the HJT frames. The tested modules were mounted on the rooftop of the Laboratory of Photovoltaics, University of York, York, UK. Since the measurements have been carried out in different periods of the day, the level of irradiance varies slightly for each PV module and they can be grouped into three nominal values, namely 300 W/m^2, 500 W/m^2 and 700 W/m^2. For each curve, three main electric parameters are extracted (V_{OC}, I_{SC} and the power at MPP P_{MAX}), and the PV temperature as well as the environmental parameters are reported in Table 4.10. G_f indicates the irradiance received on the front side of the PV modules, whereas G_b represents the irradiance received on the back side of the bifacial PV modules.

Figure 4.21a reports the I–V curve measured on the bifacial irradiating the front side whereas Figure 4.21b reports the I–V curve obtained irradiating the back side. It is worth noting that all the experimental curves reported in this section are directly obtained from the I–V tracer and no curve approximation is performed [130].

At the same levels of irradiance, module #2 shows a reduction of almost 16% in I_{SC} due to the worse optical properties of the rear side compared to the front. The tested bifacial modules show, in fact, a bifaciality factor of 0.8, as reported by the manufacturer [87]. Additionally, the I–V curves of module #2 show the typical ladder-shape characteristic, due to the presence of the wires partially shadowing the exposed surface (the junction box is placed in the back side). As can be observed from Figure 4.21a and Figure 4.21b as well as from Table 4.10, the V_{OC} decreases whilst the level of irradiance decreases, except for the black curve. It is well known that the V_{OC} has a strong negative dependence on the temperature and only a fair positive dependence on the solar irradiation. Consequently, the black curve shows a higher V_{OC} compared to the red one due to the lower PV

Table 4.10. Outdoor experimental results of the different tested PV modules.

PV Module		G_f **[W/m²]**	G_b **[W/m²]**	T_{AMB} **[°C]**	T_{PV} **[°C]**	V_{OC} **[V]**	I_{SC} **[A]**	P_{MAX} **[W]**
N-type mono–Si	#1	710	120	26	38	36.35	9.76	283.5
		502	101	24	35	35.69	7.09	204.2
		303	80	21	28	36.01	4.18	121.76
	#2	709	119	26	38	36.01	8.13	208.2
		502	101	24	35	35.15	5.80	126.0
		320	82	21	28	35.60	3.48	60.2
mono–Si	A	711	–	26	39	19.94	0.24	2.95
		502	–	24	38	19.42	0.17	1.65
		299	–	21	31	18.49	0.10	0.59
	B	711	–	26	39	20.65	3.81	44.79
		510	–	24	37	20.29	2.71	30.09
		312	–	21	31	19.94	1.65	20.59
a–Si Thin Film		699	–	26	38	22.62	3.82	62.25
		510	–	24	35	22.45	2.82	45.58
		305	–	21	28	22.17	1.63	27.75
poly–Si		700	–	26	39	21.04	5.99	88.94
		510	–	24	35	20.67	4.32	63.05
		305	–	21	28	20.00	2.58	36.58

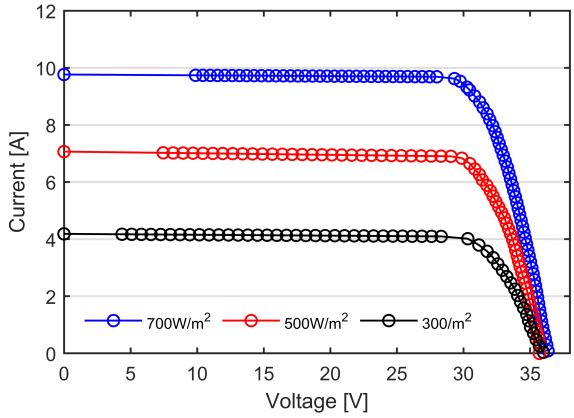

(a)

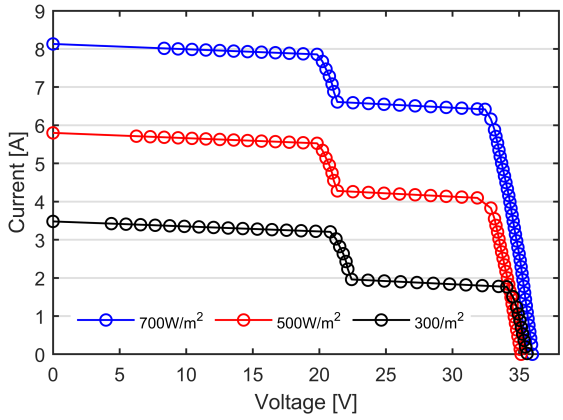

(b)

Figure 4.21. I–V curves of the N-type mono-Si bifacial PV modules under three nominal irradiance levels, namely 700 W/m^2 in blue, 500 W/m^2 in red and 300 W/m^2 in black, measured with the proposed I–V tracer. **(a)** Module #1 with the front side exposed to the sun; **(b)** module #2 with the back side exposed to the sun. The ladder-shape curves are caused by the wires partially shadowing the exposed surface. Reproduced from my own work [8].

temperature (28 °C and 35 °C, respectively, as reported in Table 4.10). The curves reported in Figure 4.22a and Figure 4.22b are those acquired

from the flexible mono-facial mono–Si PV modules rated, respectively, 20 Wp (indicated as mono–Si B in Table 4.10) and 100 Wp (mono–Si A in Table 4.10).

By comparing the measured values with those reported from Table 4.10, it is clear that both the PV modules are affected by a significant power loss. The shape of the measured I–V curve differ from the one of a healthy module. For example, in module #2, the extracted values of the saturation current ($I_0 = 0.3mA$) and shunt resistance ($R_{SH} = 30W$) indicate a reduction in the charge carriers' extraction at the contacts of the silicon cells, as well as a significant amount of leakage current through the shunted paths across the PV cells. The I–V curves obtained from the remaining tested technologies, namely a–Si thin film and poly–Si, are reported, respectively, in Figure 4.23a and Figure 4.23b.

The measured I–V curves are also compared to the theoretical I–V curves (reported in dashed line), obtained from the datasheet of the PV modules, employing the SDM (see Equation (3.1)) under matching solar irradiance and temperature conditions. The measured irradiance and PV temperature are reported in Table 4.10. The SDM is selected for its ease of implementation and lower computational resource requirements, while still providing sufficient accuracy and consistent results for the electrical modelling of the tested modules. It is well-known that a–Si technology experiences an initial degradation caused by light soaking, *i.e.*, the Staebler–Wronski effect, which reduces the power until it reaches a stabilized level, typically after few hundred hours of illumination. The degraded performance might be partially recovered from the effects of thermal annealing, such as during summertime after a long exposure to weather conditions [131]. To address the Staebler–Wronski effect, the IEC 61646 [36] standard requires that the electrical parameters provided by the manufacturer refer to the stabilized conditions. Since the sunlight exposure of the tested PV module was not permanent but limited to the time of the experiments, a good agreement between the nominal and testing conditions is assumed. As can be observed in Figure 4.23a and Figure 4.23b, the curves show the same trend with very scarce differences, in particular in the horizontal flat of the I–V curves. To better appreciate the discrepancy between the theoretical data and the ones measured with our I–V tracer, the mean value and the standard deviation of the relative percentage error is computed

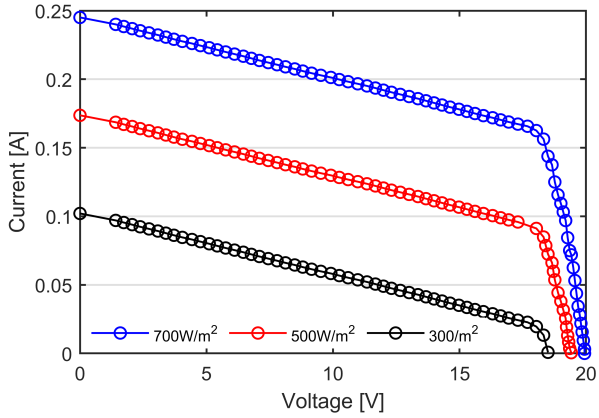

(a)

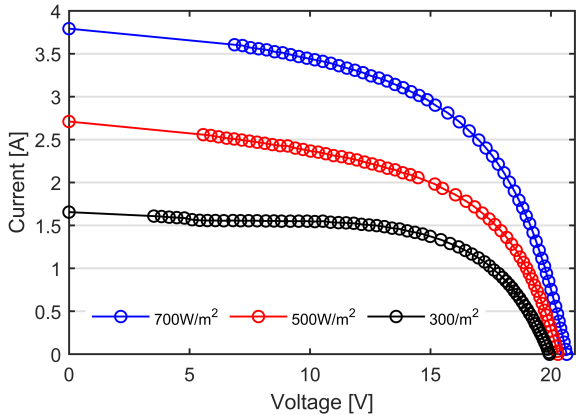

(b)

Figure 4.22. I–V curves of the mono-Si modules under three nominal irradiance levels, namely 700 W/m^2 in blue, 500 W/m^2 in red and 300 W/m^2 in black, measured with the proposed I–V tracer. **(a)** Module #1 with rated power 20 Wp; **(b)** module #2 with rated power 100 Wp. Reproduced from my own work [8].

for each tested PV module. The results are reported in Table 4.11.

The mean relative error is an indication of the accuracy of the instrument, exhibiting a maximum discrepancy of approximately 3% in the

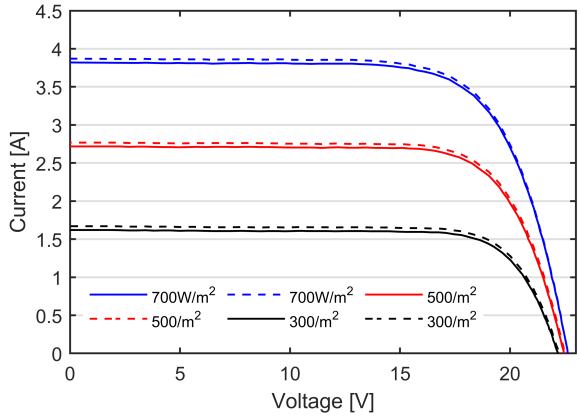

(a)

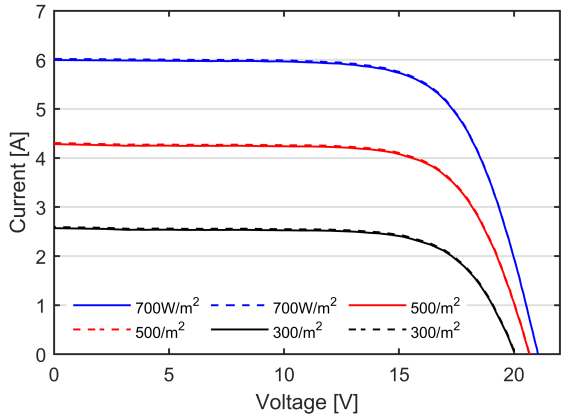

(b)

Figure 4.23. I–V curves under three nominal irradiance levels, namely 700 W/m2 in blue, 500 W/m2 in red and 300 W/m2 in black, measured with the proposed I–V tracer (solid lines) compared to the theoretical I–V curve in the same operating conditions (dashed lines). **(a)** a-Si thin film PV module; **(b)** Poly-Si PV module. Reproduced from my own work [8].

mono–Si technology. By contrast, the best performance is shown in the poly–Si technology, showing a good match between the measured data and the theoretic ones.

Table 4.11. Mean and standard deviation of the error computed between the measured I–V curves and the reference curves.

PV Module		Mean [%]	Standard Deviation [%]
Bifacial N-Type mono–Si	#1	0.94	<0.001
	#2	1.69	0.16
mono–Si	A	2.13	0.25
	B	3.04	0.41
a–Si Thin Film		1.28	0.15
poly–Si		0.38	0.045

4.5 Conclusions

In this chapter, my research activity on the design and development of an innovative I–V tracer based on Darlington transistors for on-field measurements is presented. This monitoring tool embeds powerful features, such as the ability of tracing the I–V characteristics on-line, meaning during the normal string operation by means of a novel disconnecting circuit. The tool is provided with a wireless and low power communication module, thus not requiring additional cabling. The implemented control algorithm is able to regularly distribute the working points along the I–V characteristic, thanks to the exploitation of two Darlington branches. The prototype of the I–V curve tracer has been designed and tested on PV modules of distinct technologies, with I_{SC} of up to 10A and V_{OC} of up to 50V. The effectiveness of the proposed monitoring tool is assessed by means of an extensive experimental campaign carried out both at the University of Naples Federico II, and University of York. The I–V characteristics are measured both under uniform light conditions and partial shading scenario. The data points are properly analyzed to prove the capability of evenly distributing the measured points along the I–V curve, guaranteeing a RSD less than 10%. The results clearly demonstrated that the proposed I–V tracer performs the measurement in less than 1 s and outperforms commercial devices, such Seaward PV200 in terms of measurement accuracy and resolution. Additional tests performed outdoor suggest that the proposed I–V tracer exhibits a measurement error of less than 3%.

Chapter 5

A Switch-mode Converter-based Impedance Analyzer

5.1 Introduction

Traditional impedance analyzers are laboratory-grade instruments that rely on precision sources and measurement circuitry. While they provide excellent accuracy, they are typically bulky, expensive, and unsuitable for on-field and on-line deployment in PV installations. To overcome these limitations, alternative solutions have been explored in the literature, among which switch-mode converters stand out for their efficiency and possibility of integration with existing PV facilities. In this approach, a DC–DC converter connected to the PV module is exploited not only as a variable load, according to the definition given in Chapter 4, but also as a means of injecting controlled small-signal perturbations over a broad frequency range. Nevertheless, the design of such a system must carefully address key several challenges, such as the accuracy of small-signal injection, the influence of the switching ripple, and the capability of the system to manage the energy generated by the PV module during the IS measurement.

In this chapter, the architecture and implementation of a portable switch-mode converter–based impedance analyzer for on-field IS measurement are presented. The chapter reviews the main circuital architecture

proposed for the implementation of impedance spectroscopy and outlines the design requirements of converter-based impedance analyzers, including the control loop design and the procedure adopted for performing IS impedance. Subsequently, the chapter presents the experimental validation of the circuit performed on a PV module mounted on the rooftop of the Department of Electric Engineering and Information Technology and eventually challenges and future directions are discussed.

The work presented in this chapter is the result of my research activity carried out in collaboration with the University of Naples "Federico II" within the framework of the PRIN 2020 and the PRIN2022 research projects. The outcomes of this work have been disseminated in the following publications [10, 11].

5.2 Background

This section reviews the main circuit architecture proposed for the implementation of IS. Most of these solutions have been originally developed in the context of battery systems, where IS has been extensively employed for characterization and diagnostics. Their design principles can be in principle transposed to PV modules, although their application in this domain entails specific challenges and constraints that need to be addressed.
In battery systems, impedance measurements can be performed either offline, with the battery disconnected from its operational environment or on-line, with the battery operating under load. For offline measurements, most state-of-the-art IS equipment relies on linear amplifier architectures [132, 133, 134]. These setups typically include a power amplifier for injecting the excitation signal, a low noise conditioning circuit for amplifying the battery signals, and a high resolution DAQ system. These solutions provide the best performance in terms of accuracy and therefore considerable effort has been invested in designing integrated solutions where both the analog excitation front end and high-resolution acquisition chain are embedded in a single chip [135, 136]. More advanced ICs, such as AD5940 by Analog devices [137], even integrate a dedicated discrete Fourier transform engine for real-time impedance computation. Despite their accuracy, linear solutions are not well suited for on-field measurements of PV modules. The limitation arises from the requirement to bias the PV module at its

MPP. In such a case, the linear amplifier should handle significant power dissipation, which introduces severe thermal issues. Large heat sinks would therefore be necessary to dissipate the excess energy, making the approach impractical for portable on-field applications. A potential workaround is to combine the linear amplifier with an external device, such as an electronic load, to provide the DC bias while the amplifier injects the small-signal perturbations. While this approach reduces some of the thermal burden, it remains impractical for on-field applications due to setup complexity and limited scalability. Power electronic converters, both DC-DC and AC-DC topologies, have emerged as highly attractive solutions for on-line IS testing in battery systems. These converters offer improved integration with existing facilities [138] because they can be used as excitation source for IS while providing their function of conversion stage. In [139], the authors designed a half-bridge converter with a dedicated low pass filter aiming to measure the impedance up to 2 kHz. Similarly, [140] proposed a full-bridge along with an LC filter capable of fulfilling design constraints in terms of maximum admissible current ripple injected in the battery and excitation frequency, while ensuring minimum volume and system power loss. Differently, in [141], an interleaved three-leg buck converter was employed to reduce high-frequency switching ripple and, consequently, to enhance the signal-to-noise ratio during IS acquisition. Extending converter-based approaches to PV modules is particularly promising thanks to the capability of providing superior thermal management with respect to the above-mentioned linear solutions. Additionally, switching solutions can be more easily integrated into existing power electronics infrastructures, such as MPPT circuits. However, it must be remarked that prior works on batteries cannot be directly used as setups for measuring PV modules. A key difference between IS for batteries and PV modules lies in the maximum excitation frequency. For battery cells, the impedance spectrum of interest typically spans from several millihertz up to only a few kilohertz [139] whereas in silicon PV modules it extends up to 50 kHz [71]. This significantly alters the circuit design constraints: DC/DC converters intended for PV-oriented IS must operate reliably at higher excitation frequencies, which demands a careful design to increase the system dynamics and to diminish parasitic effects.

The literature on IS circuits for PV modules is extremely sparse. To date,

only a handful of works have been reported, with the very first publication appearing in 2017 [94], where a boost converter with a variable duty cycle was used to inject a single sinusoidal perturbation. The prototype, however, was limited to a very small PV module (0.8 W, 3.4 V) and thus cannot be generalized to standard modules. An enhanced version was proposed in [142], implemented with Silicon Carbide mosfets, extended the frequency range up to 10 kHz, but measurements were only validated indoors under controlled irradiance and were confined to conditions near V_{OC}. Later, a quantitative feedback control theory approach to the design of the closed loop compensator of the above-mentioned boost converter is proposed in [143], to mitigate the effect of non-linearities in the system. None of the reported solutions are viable for on-field applications: they rely on external and bulky DAQ systems, and the accuracy of the measurement is proven only in laboratory setups.

5.3 Methodology and converter design

A portable impedance analyzer based on switch-mode converter for on-field IS measurements has been realized and tested. As also provided in Section 4, the circuit is tailored to typical PV specifications:

- Maximum $P_{\mathrm{MPP}} = 300$ W
- Maximum $V_{\mathrm{OC}} = 50$ V
- Maximum $I_{\mathrm{SC}} = 10$ A
- Maximum excitation frequency = 50 kHz

The block diagram of the proposed impedance analyzer is reported in Figure 5.1. The tool comprises the DC-DC converter, based on a non-isolated Ćuk converter, a DAQ comprising a signal conditioning circuit and a high-resolution ADC, a MCU and finally a Bluetooth module for the wireless communication. This latter enables communication between the tool and a remote controller. The remote controller (i) sends the start of measurement command, for each frequency point, it (ii) receives the measured data and (iii) compute the PV impedance. Finally, the impedance spectrum for the entire frequency range is available.

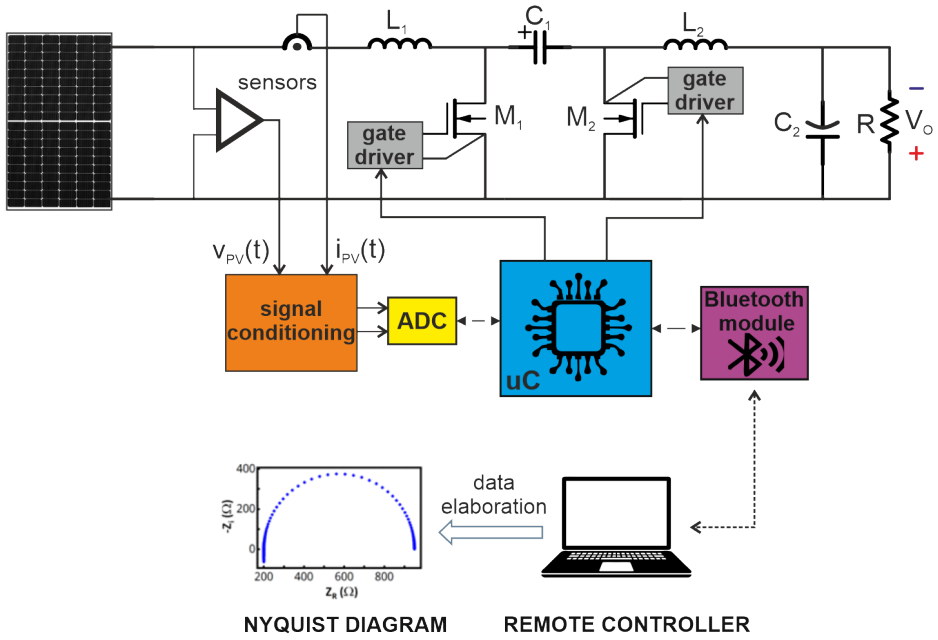

Figure 5.1. Schematic diagram of the proposed portable switch-mode impedance analyzer. The tool embeds the DC-DC converter in Ćuk topology, current and voltage sensors for measuring the PV current and PV voltage, a control unit based on MCU, a Bluetooth module, and a a power supply section. The PV current and PV voltage are amplified by a signal conditioning circuit and acquired by a high resolution ADC. The MCU communicates wirelessly to a remote controller, which computes the impedance spectrum and plots it on a Nyquist diagram.

The converter output is connected to a load that includes both capacitive and resistive components. The capacitive component consists of a supercapacitor bank C_2 (see Figure 5.1) acting as an energy storage system. One of the key features of the proposed tool is its capability to act as a source of excitation while biasing the PV module at a specific operating point, namely the MPP. Consequently, C_2 is sized to absorb a significant portion of the produced energy, charging up and varying its voltage within a well-defined range of output voltage $V_O \in [V_{O,min}, V_{O,max}]$. Simultaneously, the resistive load R (see Figure 5.1) dissipates the remaining portion of the energy as heat. At the end of the measurement, the energy stored in

C_2 is slowly dissipated through R, creating power spread. Further details on the sizing of C_2 and R are provided in the following sections.

The DC-DC converter is based on a Ćuk topology since it provides the following advantages:

1. continuous input current, favoring the injection of small perturbations without the need of additional input filters;

2. continuous output current, thereby lowering the power dissipation on the supercapacitor equivalent series resistance and mitigating thermal issues.

3. buck-boost capability; in other words, the input voltage can be either higher or lower than the output voltage, thus making the tool suitable for wide variety of PV modules. In addition, the buck-boost capability makes the tool suitable for I-V curve tracing [116].

In the following, a detailed description of the methodology adopted for the design of the Ćuk converter is given.

5.3.1 Impedance spectroscopy operation

To perform IS analysis, when the PV module is forced to operate at its MPP, namely (V_{MPP}, I_{MPP}), a sinusoidal perturbation is injected. By considering a galvano-static approach, the PV current can be expressed as

$$i_{PV}(t) = I_{MPP} + \tilde{i}_{PV}(t) + i_{SW}(t) \tag{5.1}$$

where $\tilde{i}_{PV}(t)$ is the AC current perturbation and $i_{SW}(t)$ is the high frequency switching component due to the Pulse Width Modulation (PWM) modulation. A qualitative illustration of Equation (5.1) is presented in Figure 5.2.

Assuming a small-signal sinusoidal stimulus, $\tilde{i}_{PV}(t)$ and the corresponding voltage response $\tilde{v}_{PV}(t)$ are the followings.

$$\tilde{i}_{PV}(t) = A_I sin(2\pi f_S t) \tag{5.2}$$

$$\tilde{v}_{PV}(t) = A_V sin(2\pi f_S t - \gamma) \tag{5.3}$$

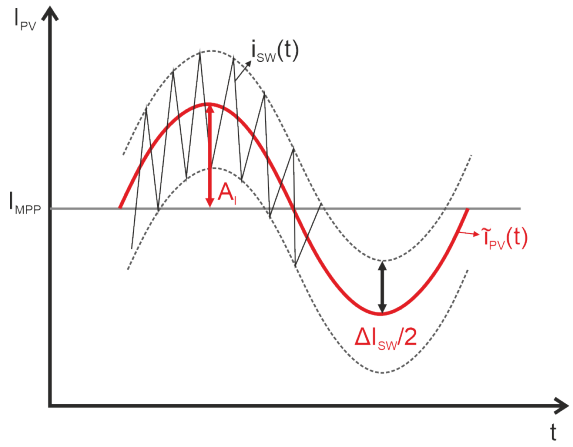

Figure 5.2. Illustration of Equation (5.1). The PV current is given as the sum of three components: the DC current, corresponding to the MPP I_{MPP}, the sinusoidal perturbation $i_{PV}(t)$ of amplitude A_I and the switching ripple $i_{SW}(t)$ of amplitude $\Delta I_{SW}/2$.

where A_V and A_I are, respectively, the amplitude of the voltage and current perturbation, f_S is the stimulation frequency and γ is the phase shift between the voltage and the current perturbation. In principle, to inject the AC stimulus, a small AC perturbation can be injected in the duty cycle signal:

$$d(t) = D + \tilde{d}(t) \tag{5.4}$$

$$\tilde{d}(t) = A_d sin(2\pi f_S t) \tag{5.5}$$

where D is the DC duty cycle, responsible of defining the MPP bias on the PV module, and A_d is the amplitude of the duty cycle perturbation. To ensure system stability and linearity as required by Kramer Kroning's condition, the amplitude of the A_I signal, and consequently A_d, should be chosen to be as small as possible and constant for all frequencies.

5.3.2 Design of the converter

In this section, the design constraints for the passive components of the Ćuk are defined, as function of the impedance spectrum to be measured.

Indeed, A_I and A_V vary with the frequency. Let us recall the relationship between the PV impedance and the voltage and current signals in the frequency domain, as already defined in Chapter 2.

$$\bar{Z}(f) = \frac{\bar{V}(f)}{\bar{I}(f)} = \frac{A_V}{A_I} e^{-j\gamma} \tag{5.6}$$

Considering the typical behavior of the impedance of a PV module represented in a Nyquist diagram, the maximum value of the impedance corresponds to the intersection of $\bar{Z}$ with the *x-axis* (real axis) at 0 Hz, as shown in Figure 5.3. The maximum value of the impedance is indicated as $R_{PV,max}$. The minimum current amplitude, $A_{I,min}$, is defined as the ratio between the minimum measurable voltage amplitude, $A_{V,min}$, and $R_{PV,max}$.

$$A_{I,min} = \frac{A_{V,min}}{R_{PV,max}} \tag{5.7}$$

Therefore, $A_{V,min}$, and $R_{PV,max}$ are input parameters for the converter sizing. Since the effect of the switching ripple must be taken into account, the maximum current ripple amplitude $\Delta I_{SW,max}$ must be evaluated. Since the IS measurement is assumed to be performed at MPP, from Figure 5.4,

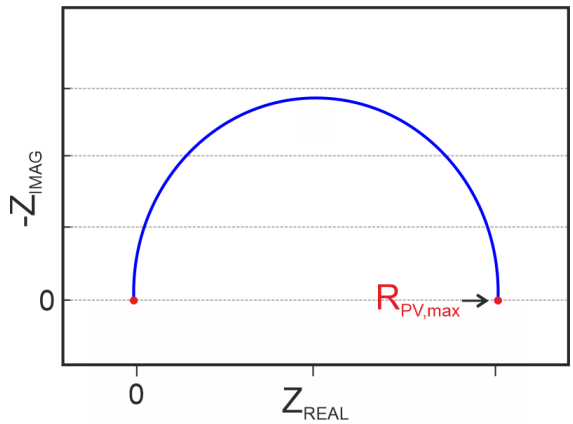

Figure 5.3. Illustration of the Nyquist spectrum of a typical PV module. The red marker highlight the maximum value of the real part of the impedance $R_{PV,max}$.

the following inequality must be imposed.

$$\Delta I_{SW,max} < 2[(I_{SC} - I_{MPP}) - A_{I,min}] \tag{5.8}$$

Equation (5.8) guarantees that the current ripple remains sufficiently smaller than the current perturbation, preventing distortion during IS measurements. To ensure a correct modulation of the current perturbation, f_{SW} must be selected according to the maximum excitation frequency $f_{S,max}$. A rigorous way to determine f_{SW} relies on comparing ΔI_{SW} with the rate of change of the sinusoidal signal. During each switching period, the variation of the sinusoidal current should be sufficiently larger than the amplitude of the superimposed ripple, so that the sinusoidal modulation is not distorted. In other words, the maximum rate of change of the inductor current, defined by the switching ripple, should be greater than the maximum rate of change of the perturbation current.

$$\frac{\Delta I_{SW}}{T_{SW}} > max\left[\frac{d\tilde{\imath}_{PV}(t)}{dt}\right] \tag{5.9}$$

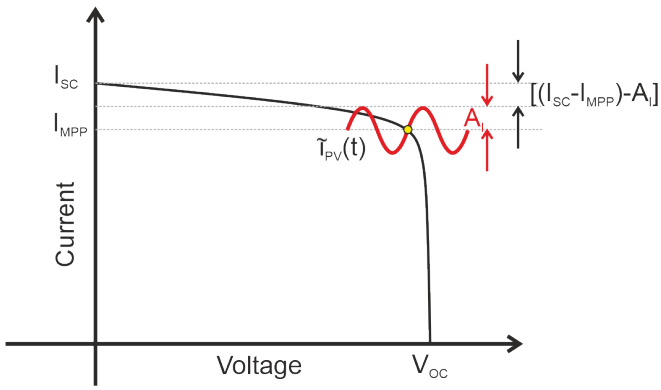

Figure 5.4. Illustration of Equation (5.8). The maximum admissible amplitude of the switching ripple is given as the difference between the short circuit current I_{SC}, the current in the maximum power point I_{MPP} and the amplitude of the current perturbation A_I.

From Equation 5.9, the following inequality is therefore derived.

$$f_{SW} > \frac{2\pi f_{S,max} A_{I,min}}{\Delta I_{SW,max}} \tag{5.10}$$

The current ripple ΔI_{SW} appears as a superimposed triangular wave on the inductor current.

$$\Delta I_{SW} = \frac{V_{PV} D}{f_{SW} L_1} \tag{5.11}$$

Assuming $V_{PV} = V_{MPP}$ and $D = 1$, Equation 5.11 defines the theoretical maximum amplitude of the current ripple $\Delta I_{SW,max}$ at MPP. Therefore, the following inequality is derived for sizing the inductor L_1.

$$L_1 \geq \frac{V_{MPP}}{f_{SW} \Delta I_{SW,max}} \tag{5.12}$$

The supercapacitor bank C_2 is sized to partially store the energy produced by the module during the measurement time interval T_{MEAS}. Considering the maximum measurement time interval $T_{MEAS,max}$, the following inequality is derived.

$$C_2 \leq \frac{2 P_{MPP} T_{MEAS,max}}{\Delta V_O^2} \tag{5.13}$$

where ΔV_O is the voltage variation across C_2, with $\Delta V_O = V_{O,max} - V_{O,min}$. As discussed in the previous section, the resistive load partially dissipates the energy produced as heat. The value R is a trade-off between the maximum power it can dissipate $P_{R,max}$, typically defined as a small percentage of P_{MPP} and the minimum power that the PV module must deliver $P_{PV,min}$ to guarantee the charge of C_2. Based on the above-mentioned consideration, the following design criterium is derived.

$$\frac{V_{O,min}^2}{P_{in,min}} \leq R \leq \frac{V_{O,max}^2}{P_{R,max}} \tag{5.14}$$

Moreover, it must be pointed out that R also affects the discharge rate of C_2, defining the time constant $\tau = RC_2$. Finally, the remaning passive components of the Ćuk converter, namely C_1 and L_2, are sized to meet the constraints in terms of maximum voltage ripple on the voltage across

C_1, ($r_{V_{C1}}$) and maximum current ripple on the current through L_2 ($r_{I_{L2}}$) [144]

$$C_1 = \frac{(1 - D_{MPP})^2 P_{MPP}}{2 f_{SW} r_{V_{C1}} V_{MPP}^2} \tag{5.15}$$

$$L_2 = \frac{D_{MPP}^2 P_{MPP}}{2 f_{SW} r_{I_{L2}} I_{MPP}^2 (1 - D_{MPP})} \tag{5.16}$$

where D_{MPP} is the steady-state duty cycle value corresponding to the MPP.

5.4 Dynamic analysis

In this section, the dynamic behavior of the Ćuk converter is presented by deriving a fast and straightforward discrete-time model implemented in Matlab/Simulink. The aim of the proposed model is to reduce the simulation time and to facilitate the development of a proper closed loop controller. To this regard, an extended electric model of the converter is considered (see Figure 5.5) which includes the parasitic components as equivalent series resistances, whereas the PV module is modeled according to the SDM defined in Chapter 3. Based on the design procedure outlined in the previous section, the Ćuk converter is sized imposing the following input design parameters.

- $f_{S,max} = 50\ kHz$,

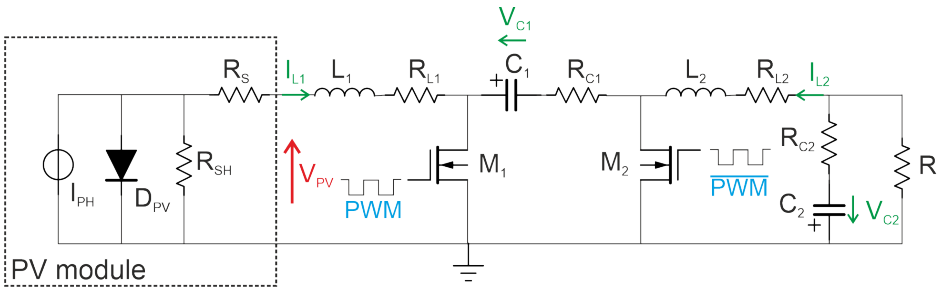

Figure 5.5. Schematic diagram of Ćuk converter including the passive components. The PV module is modeled according to the SDM.

- $R_{PV,max} = 100\ m\Omega$
- $A_{V,min} = 20\ mV$
- $I_{SC} = 10\ A$
- $T_{MEAS,max} = 1\ s$
- $V_{0,max} = 10\ V$ and $V_{0,min} = 5\ V$
- $P_{in,max} = 10\ W$
- $P_{R,max} = 5\ W$
- $D_{MPP} = 0.5$

The design of the Ćuk converter is reported in Table 5.1. It worth mentioning that the selected R value guarantees the discharge of the bank of supercapacitors in almost 20 s.

Table 5.1. Summary of the design parameters

Parameter	**Value**
Switching frequency f_{SW}	500 kHz
Input inductance L_1	580 μH
Input inductance series resistance R_{L1}	70 mΩ
Bridge capacitance C_1	10 μF
Bridge capacitance series resistance R_{C1}	45 mΩ
Output inductance L_2	174 μH
Output inductance series resistance R_{L2}	11 mΩ
Output capacitance C_2	1.5 F @ 10 V
Output capacitance series resistance R_{C2}	20 mΩ
Output resistance R	20 Ω

5.4.1 Continuous-time model

The converter behaves as a time-varying non-linear model, depending on the status of the two switches M_1 and M_2. Each power switch is described as an open circuit when it is OFF, while it behaves as a short circuit when is turned ON. Moreover, the converter operates as a synchronous switching power converter, and the two switches always operate in a opposite phase (*i.e.*, M_1 is ON, while M_2 is OFF, and vice versa). The dynamic model of the converter in the input-state-representation can be expressed as

$$F_i \dot{x} = g_i \tag{5.17}$$

where $x = [I_{L1}\ V_{C1}\ I_{L2}\ V_{C2}]$. If the switching status u is 1 (*i.e.*, M_1 is ON, while M_2 is OFF),

$$F_1 = \begin{bmatrix} L_1 & 0 & 0 & 0 \\ 0 & C_1 & 0 & 0 \\ 0 & 0 & 0 & (R_{C2}+R)C_2 \\ 0 & 0 & L_2 & R_{C2}C_2 \end{bmatrix} \tag{5.18}$$

and

$$g_1 = \begin{bmatrix} v_{PV} - R_{L1}x_1 \\ -x3 \\ -x_4 + Rx_3 \\ x_2 - (R_{C1}+R_{L2})x_3 - x_4 \end{bmatrix} \tag{5.19}$$

while if $u = 0$ (*i.e.*, M_1 is OFF while M_2 is ON),

$$F_2 = \begin{bmatrix} L_1 & 0 & 0 & 0 \\ 0 & C_1 & 0 & 0 \\ 0 & 0 & L_2 & R_{C2}C_2 \\ 0 & 0 & 0 & (R_{C2}+R)C_2 \end{bmatrix} \tag{5.20}$$

and

$$g_2 = \begin{bmatrix} v_{PV} - (R_{L1}+R_{C1})x_1 - x_2 \\ x_1 \\ -x_4 - R_{L2}x_3 \\ Rx_3 - x_4 \end{bmatrix} \tag{5.21}$$

The model was implemented in Matlab/Simulink. It provides very accurate behavior of the converter. Nevertheless, the model requires long simulation times, also requiring a variable step solver with a maximum time step lower of the switching period (*i.e.*, $T_{SW} = 2\ us$).

5.4.2 Discrete-time model

To obtain an accurate tool to support the Ćuk converter design without requiring long simulation times, a specific discrete-time model was developed from Equation (5.17). The adopted approach well describes power converters driven by PWM signals.

$$u = ds = \begin{cases} 1, & \text{if } t \in [kT_{SW}, kT_{SW} + T_{ON}) \\ 0, & \text{if } t \in [kT_{SW} + T_{ON}, (k+1)T_{SW}) \end{cases} \tag{5.22}$$

To reduce simulation times, the model in Equation (5.22) is linearized, by replacing the I–V curve of the PV module with the corresponding Thevenin equivalent.

$$v_{V_{PV}} = E_{PV} - R_{PV} i_{PV} = E_{PV} - R_{PV} x_1 \tag{5.23}$$

Substituting Equation (5.23) into Equation (5.19) and Equation (5.21), g_i becomes the following.

$$G_1 = \begin{bmatrix} E_{PV} - (R_P + R_{L1})x_1 \\ -x3 \\ -x_4 + Rx_3 \\ x_2 - (R_{C1} + R_{L2})x_3 - x_4 \end{bmatrix} \tag{5.24}$$

when $u = 1$, while

$$G_2 = \begin{bmatrix} E_{PV} - (R_P + R_{L1} + R_{C1})x_1 - x_2 \\ x_1 \\ -x_4 - R_{L2}x_3 \\ Rx_3 - x_4 \end{bmatrix} \tag{5.25}$$

when $u = 0$. Consequently, Equation (5.17) can be expressed as following.

$$\dot{x} = F_i^{-1} G_i = A_i x + B_i \begin{bmatrix} 1 \\ 0 \\ 0 \\ 0 \end{bmatrix} E_{PV} \tag{5.26}$$

The model in Equation (5.26) was discretized according to the discretization method Zero-Order Hold (ZOH). To this aim, the Matlab function *c2d* was employed. The discrete-time model describes the state vector $x(t)$ at the time instants $t = kT_{SW}$ as following.

$$x_{1k} = A_{1d} x_k + B_{1d} E_{PV} \tag{5.27}$$

while at $t = kT_{SW} + T_{ON}$ as following.

$$x_{2k} = x_{k+1} = A_{2d} x_{1k} + B_{2d} E_{PV} \tag{5.28}$$

The model describing the circuit in all the time instants can be computed as follows.

$$x_{k+1} = A_d x_k + B_d E_{PV} \tag{5.29}$$

where $A_d = A_{d1} A_{d2}$ and $B_d = A_{d2} B_{d1} + B_{d2}$ Moreover, a compact form of the state vector at the steady state, with $ds = cost$, can be provided.

$$x = (I - A_d)^{-1} B_d E_{PV} \tag{5.30}$$

5.4.3 Numerical results

Numerical simulations have been performed to verify the converter capability to force the PV module to operate close to the MPP and, at the same time, to inject a desired AC component in the PV current. The results obtained using the continuous-time and discrete-time models have been compared to the converter behavior obtained by a traditional circuit model implemented in Matlab/Simulink using the *Simscape Electrical* library and taken as reference. For all the three models, the initial conditions, which correspond to the Ćuk converter forcing the PV module to operate close to MPP, have been set. The initial conditions of the state variables are reported in Table 5.2.

Table 5.2. Initial conditions

State Variable	Initial Value
x_1	9.5 A
x_2	50 V
x_3	22 A
x_4	10 V

To determine if the converter is able to inject a sinusoidal perturbation on the PV current by forcing in input a sinusoidal perturbation on the duty cycle (according to Equation (5.5)), D is set 24.5% , corresponding to $I_{MPP} = 9.5$ A, A_d is set 0.1% and f_S spreads in the range [100 Hz, 50 kHz]. The transient analysis showing the behavior of the PV current over time at f_S =5 kHz and $f_S = 500$ Hz is shown, respectively, in Figure 5.6a and Figure 5.6b. The discrete-time model exhibits comparable results with those obtained using both the continuous-time and electrical model. The only discrepancy lies before the system reaching the steady-state, likely due to the effect of linearization of the PV module around the MPP.

As can be seen from Figure 5.6, the amplitude of the AC component of the inductor current decreases as the frequency increases. A complete frequency analysis obtained with the discrete-time model is reported in Figure 5.7. In open-loop configuration, *i.e.*, without a proper closed loop controller, the gain of the converter exhibits a peak at 1.630 kHz, and a decrease in the magnitude of $A_{I_{L1}}$ with increasing frequency. At $f_{S,max}$, in particular, the system significantly attenuates the current perturbation ($> 10\ dB$), thereby affecting the accuracy of IS analysis. As a consequence, a dedicated compensation controller must be design to extend the system's bandwidth up to 50 kHz.

To quantify the advantage of the discrete-time model in terms of simulation speed, the simulation time of the three models have been compared (see Figure 5.8). For each considered frequency value f_S, a transient analysis has been performed for a time equal to 10 ms + $2/f_S$. As expected, the three models exhibit different simulation times. As an example, to perform a simulation of about 10 ms (e.g., $f_S = 2$ kHz), the circuit model spends about 120 s, while the continuous-time model 55 s and the discrete-time

model less than 1 s.

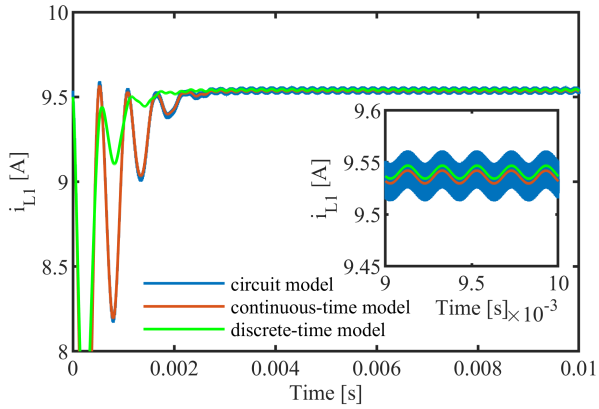

(a)

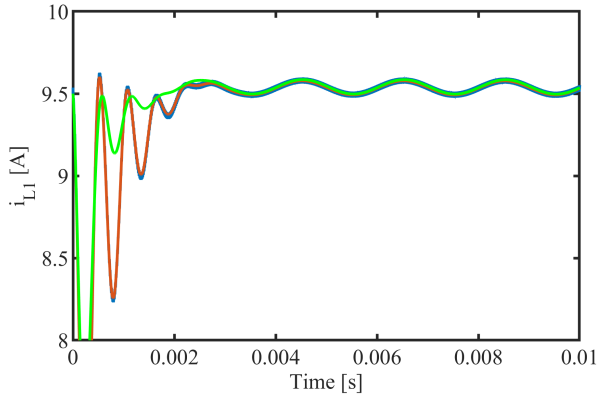

(b)

Figure 5.6. Validation of the discrete-time model: transient analysis corresponding to the injection of a sinusoidal stimulus at **(a)** $f_S = 5$ kHz and**(b)** $f_S = 500$ Hz. Reproduced from my own work [10].

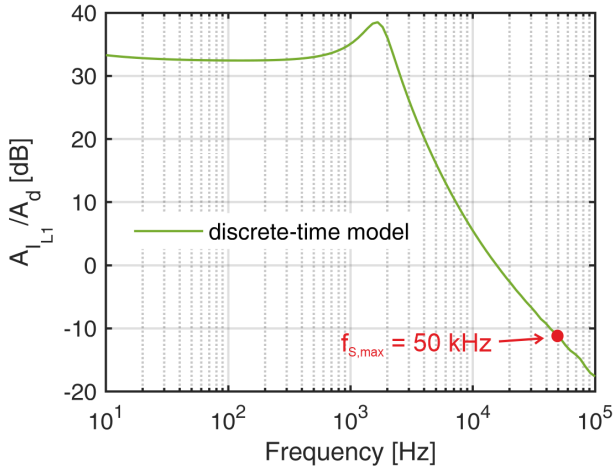

Figure 5.7. Gain of the open-loop frequency response of the converter, calculated as ratio between the amplitude of the inductor current $A_{I_{L1}}$ and the amplitude of the duty cycle perturbation A_d. The gain at $f_{S,max}$ is marked in red.

5.5 Control loop design

Based on the outcome of the dynamic analysis presented in the previous section, the open-loop control strategy cannot be adopted because the amplitude of the current perturbation is not constant over frequency. The amplitude variation significantly impacts the accuracy and even the validity of the IS measurements. A viable way to ensure constant perturbation is adopting a closed-loop control strategy based on a compensation controller. Since in Ćuk topology the PV current is controlled by the inductor current i_{L1}, the most straightforward control strategy is the single-loop current control, as shown in Figure 5.9. In this approach, the duty cycle is computed by the compensator G_C based on the error evaluated as the difference between the reference current and the inductor current. With reference to Figure 5.9, both the DC and AC components of the PV current are controlled by the same compensator G_C. For IS analysis, the compensation controller should meet the following requirements:

1. High open-loop gain at DC. The open-loop gain should be maximized

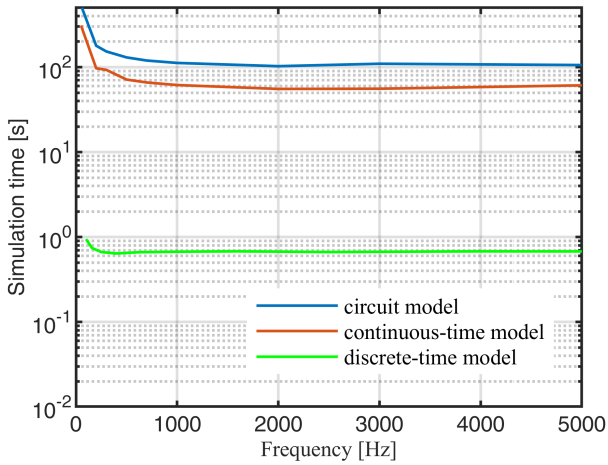

Figure 5.8. Simulation time analysis comparing the proposed discrete-time (in green), the continuous-time (in red) and converter (in blue) model. Reproduced from my own work [10].

at 0 Hz to guarantee stable operation of the PV module during IS measurements.

2. Large crossover frequency f_C. The control loop should exhibit a sufficiently high crossover frequency to provide a wide bandwidth for accurate injection of the perturbation current signals.

3. High tracking accuracy. The controller must track the perturbation signal reference with high fidelity to ensure that the OP remains within the linear region of the I–V characteristic during IS analysis.

4. Stable control system. The control system must maintain adequate stability margins, specifically a phase margin greater than 60°, and ensure that all poles of the closed-loop transfer function reside in the left-half of the complex plane.

For the purpose to fulfill all the requirements stated above, a Proportional-Integral (PI) controller has been selected as compensator controller. The

transfer function of the PI controller can be expressed as follows:

$$G_C(s) = K_{PI}\left(1 + \frac{\omega_{PI}}{s}\right) \tag{5.31}$$

where K_{PI} is the gain of the PI controller whereas ω_{PI} is the angular frequency when the phase angle of the PI controller is equal to -45°. The PI controller exhibits an infinite gain at DC and the system crossover frequency can be sufficiently extended by tuning the PI parameters. The crossover frequency represents the frequency at which the open-loop gain reaches the value 0 dB and must be selected greater than the maximum perturbation frequency $f_{S,max}$. Simultaneously, the crossover frequency should be set less than the switching frequency to mitigate the switching noise. A typical value of the crossover frequency is $1/5\ f_{SW}$. Therefore, the following design criterion must be satisfied:

$$f_{S,max} < f_C << f_{SW} \tag{5.32}$$

Assuming $f_{S,max} = 50kHz$ and $f_{SW} = 500kHz$, f_C is set 100kHz. By setting the crossover frequency and phase margin in the *pidtune* function in Matlab, the following PI parameters are sized:

- $K_{PI} = 12$
- $\omega_{PI} = 1360\ rad/s$

It must be remarked that the controller parameters identified above may need further tuning due to the influence of system parasitic components, such as those arising from the actual implementation of the prototype. Nevertheless, the theoretical values provide a reliable starting point for the experimental tuning procedure.

5.5.1 Digital implementation

The PI controller designed in the previous section has been implemented on a MCU. The continuous-time PI transfer function must be discretized to allow real-time execution within the firmware. Among possible discretization methods, the bilinear transformation offers a good trade-off

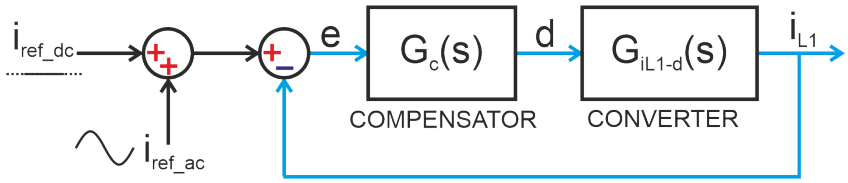

Figure 5.9. Closed-loop current control scheme of the converter. The compensator $G_C(s)$ computes the required duty cycle d to be given as input to the converter $G_{iL1-d}(s)$ based on the error between the reference current and the inductor current i_{L1}. In this approach, the reference current is given as the sum of the DC current (i_{ref_dc}) and the perturbation signal (i_{ref_ac}).

between numerical accuracy and closed-loop stability. By applying the following substitution on Equation (5.32):

$$s = \frac{2}{T_S}\frac{1-z^{-1}}{1+z^{-1}} \tag{5.33}$$

Where T_S is the sampling period, the PI function becomes the following:

$$G_{PI}(s) = K_{PI} + K_{PI}\omega_{PI}\frac{T_S}{2}\frac{1+z^{-1}}{1-z^{-1}} \tag{5.34}$$

This expression can be rearranged and converted into the following recursive form:

$$u(k) = u(k-1) + K_{PI}\left[e(k) - e(k-1)\right] + K_{PI}\omega_{PI}\frac{T_S}{2}\left[e(k) + e(k-1)\right] \tag{5.35}$$

Where $u(k)$ and $e(k)$ are, respectively, the output and the error computed at the *k-th* sampling instant whereas $u(k-1)$ and $e(k-1)$ are, respectively, the output and the error computed at the *(k-1)-th* sampling instant. In this context, the input error is computed as the difference between the reference current and the inductor current sampled at instant *k-th*:

$$e(k) = i_{REF} - i_{L1}(k) \tag{5.36}$$

Whereas the controller output $u(k)$ represents the actual duty cycle value. In order to prevent integrator windup, the controller output is limited within the range [0,1]. To validate the proposed control strategy, the

closed-loop transfer function of the system compensated by the discrete PI controller is illustrated in Figure 5.10. The controller implements the parameters derived in the previous section, while the converter's dynamics is simulated through the discrete-time model defined in Equation (5.29). Compared to the open-loop frequency response shown in Figure 5.7, the closed-loop system exhibits an extended bandwidth, with a unity gain at the target $f_{S,max}$. Figure 5.11 illustrates the waveforms of the inductor current i_{L1} and the reference current i_{ref} obtained for two excitation frequencies, namely 5 kHz (see Figure 5.11a) and 50 kHz (see Figure 5.11b). In this numerical analysis, the converter is simulated in Matlab/Simulink using the *Simscape Electrical* library to account for the effect of the switching ripple on i_{L1}. To evaluate the tracking accuracy of the designed discrete control loop, two performance metrics are defined:

$$\begin{aligned} TA_{DC} &= 1 - \frac{1}{N} \sum_{f_S=f_{S1}}^{f_{SN}} abs\left(\frac{i_{REF,DC} - i_{L1,DC}(f_S)}{i_{REF,DC}}\right) \\ TA_{AC} &= 1 - \frac{1}{N} \sum_{f_S=f_{S1}}^{f_{SN}} abs\left(\frac{A_{I_{REF}} - A_{I_{L1}}(f_S)}{A_{I_{REF}}}\right) \end{aligned} \tag{5.37}$$

where TA_{DC} represents the average tracking accuracy of the DC component of the reference current whereas TA_{AC} represents the average tracking accuracy of the AC component of the reference current. N is the number of frequency points, $i_{L1,DC}(f_S)$ is the DC component of the inductor current corresponding to the signal of excitation frequency f_S whereas $A_{I_{L1}}$ is the amplitude of the AC component of the inductor current corresponding to the signal of excitation frequency f_S. As can be seen from Figure 5.11, the inductor current follows the reference with negligible steady-state error even at 50 kHz, which represents a key design specification for the converter. Indeed, the simulative analysis demonstrates that $TA_{DC} = 99.9\%$ and $TA_{AC} = 96.8\%$, thereby proving the efficacy of the proposed discrete control loop.

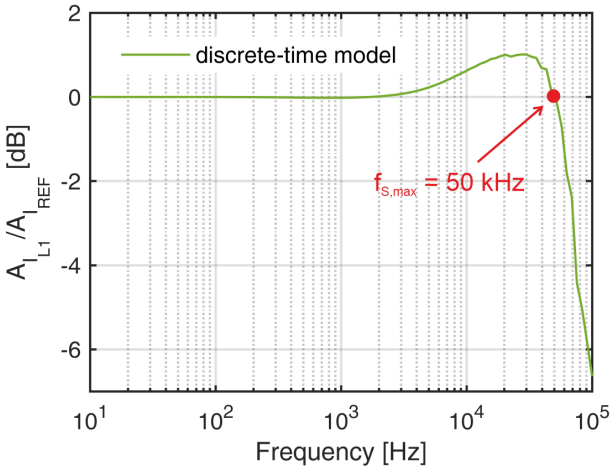

Figure 5.10. Gain of the closed-loop frequency response of the converter, calculated as ratio between the amplitude of the inductor current $A_{I_{L1}}$ and the amplitude of the reference current $A_{I_{REF}}$. The gain at $f_{S,max}$ is marked in red.

5.5.2 Control algorithm

The converter is controlled by a digital algorithm implemented in the MCU, which is in charge of identifying the DC operating point, *i.e.*, the MPP, and injecting the perturbation signals required for impedance spectroscopy analysis. The complete flowchart of the control algorithm is shown in Figure 5.12. As can be seen from the figure, the routine is organized in two main stages:

1. Maximum power point identification.

2. IS measurement.

A detailed description of the algorithm in Figure 5.12 is provided in the following subsections. It must be mentioned that during the measurement, the voltage across the bank of supercapacitor (C_2) is monitored. If V_O exceeds $V_{O,max}$, the MCU freezes the measurement meaning that it executes a routine to recover from the over-voltage condition. In this case, bank of

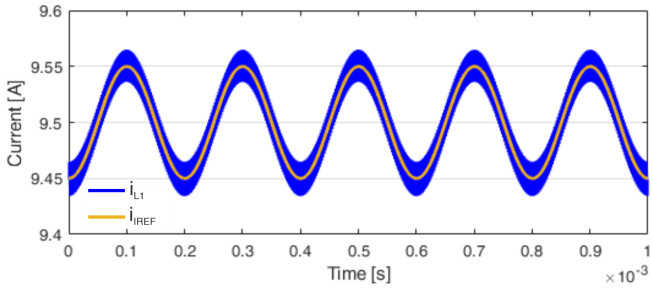

(a)

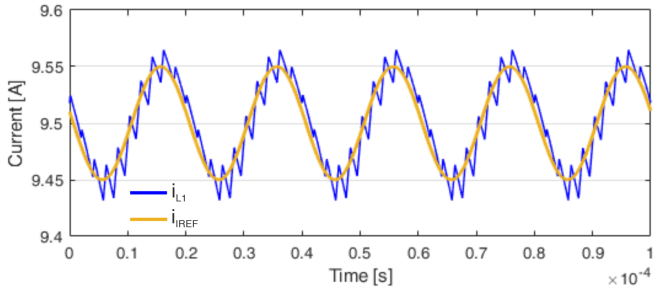

(b)

Figure 5.11. Transient analysis of the converter in closed-loop configuration, corresponding to the injection of sinusoidal current perturbations at **(a)** $f_S = 5$ kHz and**(b)** $f_S = 50$ kHz. The inductor current i_{L1} is depicted in blue, the reference current i_{REF} is shown in yellow.

supercapacitor is let to discharge through R. As soon as V_O reaches the lower threshold $V_{O,min}$, the measurement restarts.

Maximum power point identification

Before starting the IS procedure, the converter must identify the MPP under the current irradiance and temperature conditions. As sketched in Figure 5.12, the procedure begins by measuring V_{OC} and I_{SC} of the PV module:

- V_{OC} is obtained by imposing a D=0;
- I_{SC} is obtained by imposing a D=1.

The knee of the I–V curve, which indicates the region around the MPP, is calculated as:

$$knee = \frac{I_{SC}}{V_{OC}} \tag{5.38}$$

The current increment for the MPP search is defined as:

$$\Delta I = \frac{I_{SC}}{N/2} \tag{5.39}$$

where N is the number of I–V points set by the user. The MPP identification routine starts by imposing an initial reference current $i_{REF} = \Delta I$. At each iteration k, the corresponding voltage and current values, $V(k)$ and $I(k)$, are acquired and the local slope of the I–V curve is calculated as:

$$slope = \frac{I(k-1) - I(k)}{V(k) - V(k-1)} \tag{5.40}$$

The slope is then compared to the knee value:

- If $slope > knee$, the algorithm increases i_{REF} by one step ($i_{REF} = i_{REF} + \Delta I$) and repeats the measurement.
- If $slope < knee$, the MPP has been reached, which lies between $I(k-1)$ and $I(k)$.

To minimize waveform distortion during IS, the OP for the subsequent analysis is set slightly below the MPP, thus the DC reference current is defined as:

$$i_{REF,MPP} = I(k-1) \tag{5.41}$$

If the number of iterations k reaches N, the MPP has not been identified and the control algorithm stops the measurement.

Impedance spectroscopy measurement

Once the MPP has been identified, the converter performs the IS procedure by superimposing a small sinusoidal perturbation on the DC current

reference. The total reference current is therefore defined as:

$$i_{REF}(m) = i_{REF,MPP} + i_{ref,AC}(m) \tag{5.42}$$

where the AC perturbation term is expressed as:

$$i_{REF,AC}(m) = A_I sin\left(2\pi m \frac{f_S}{f_{SW}}\right) \tag{5.43}$$

where m is the discrete time index spanning from 0 to $M-1$. M represents the number of samples per period of the injected signal, and it is defined as $M = floor(f_{SW}/f_S)$. As depicted in Figure 5.12, M is dynamically computed considering the perturbation frequency. According to the Nyquist-Shannon criterium, the minimum value of M should be 2 to ensure a perfect reconstruction of the sinusoidal perturbation. In practical application, the minimum value of M has been identified as 10 for an adequate reconstruction of the sinusoidal perturbation. For each reference current sample, the MCU computes the necessary duty cycle by means of Equation (5.35) and Equation (5.36). The control routine executes the perturbation injection while simultaneously acquiring both the PV voltage and current. Moreover, N_P sinusoidal cycles per frequency are acquired to enhance SNR and this parameter can be set by the user. At the end of IS procedure, the sampled data are transmitted wirelessly to a remote controller, which performs the impedance calculation through Fourier analysis.

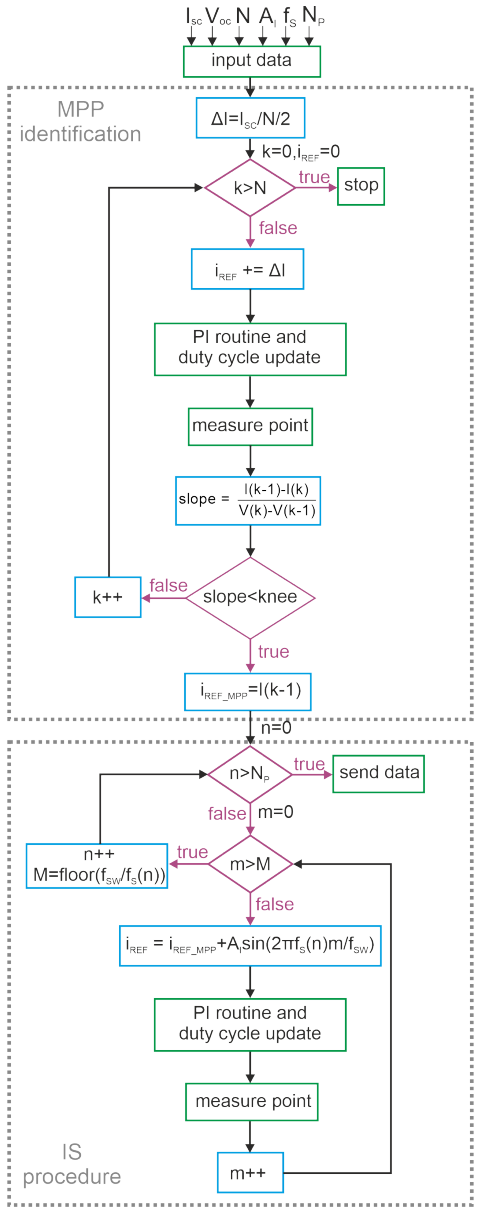

Figure 5.12. Control algorithm of the proposed switch-mode impedance analyzer.

5.6 Experimental validation

In this section, the experimental validation of the proposed switch-mode impedance analyzer is presented.

5.6.1 Prototype

The proposed impedance analyzer has been prototyped on a standard PCB, shown in Figure 5.13. As mentioned, the Ćuk converter implements a synchronous architecture, and it is realized in Gallium Nitride (GaN) technology to achieve a high switching frequency (500 kHz). Along with faster switching speed, GaN mosfets benefit from lower conduction losses compared to traditional silicon technology, thus increasing the overall converter efficiency, and reverse conduction capability, thereby avoiding the need for freewheeling diodes. The MCU employed in the prototype is 168 MHz clock-speed STM32F407 by STMicroelectronics. The MCU delivers 210 DMIPS and features a dedicated floating-point unit to accelerate arithmetic-intensive computations. These features have been used to implement the digital controller described in the previous section, with duty cycle values computed and updated twice every switching period, adopting

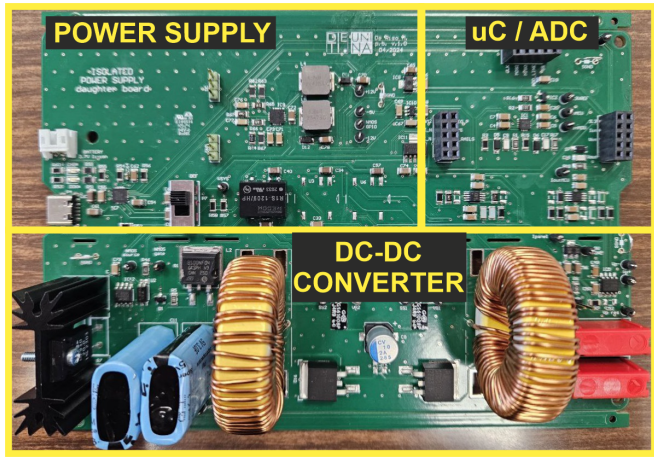

Figure 5.13. Prototype of the implemented switch-mode impedance analyzer realized on PCB. Adapted from my own work [11].

the double update PWM method proposed in [145] to reduce control delay and improve the system stability. The PV current is sensed by means of a Tunneling-Magneto Resistive (TMR)-effect sensor IC placed in series with the current path of the PV module. The TMR sensor has been selected among other current sensing topologies for the following advantages: with respect to Hall-effect sensor, (i) it provides larger bandwidth, up to 1 MHz, and (ii) lower noise level, whereas with respect to shunt-based solutions, (iii) it inherently provides galvanic isolation and (iv) it does not need an isolated power supply. The PV voltage is sensed by means of dedicated voltage divider coupled with an isolated amplifier. The sensed signals are acquired by a 4 Ms/s 16 bits ADC, communicating with the MCU via Serial Peripheral Interface (SPI). The prototype is battery-powered by a 3.7 V 2050 mAh Li-Ion battery. The main components used in the prototype are listed in Table 5.3.

Table 5.3. Key components used in the prototype of the proposed switch-mode impedance analyzer

Component	Description	Model
MCU	32-bit, 168 MHz clock speed	STM32F407VG
Current Sensor	TMR-sensor IC	CT427-HSN820DR
Voltage Sensor	Resistive voltage divider + isolated amplifier	SI8931B
ADC	16-bit 4 MS/s SAR	AD8510ARZ
M1, M2	GaN technology	GS61008P
Gate Drivers	Isolated driver	SI8271GB
L1	560 μH, 20 A	MCAP115018077A-561LU
C1	10 μF, 100 V	A767KS106M2ALAE045
L2	380 μH, 20 A	MCAP115018062A-381MU
C2	Supercapacitors 1.5 F, 10 V	PM-5R0V305
R	20 Ω, 100 W	–
BT	–	LAIRD TECNOLOGIES BT740-SC
Battery	3.7 V, 2050 mAh, 7.59 Wh	–

5.6.2 Experiment

To validate the operation of the converter, the PV module PV-MF120EC3 [128] has been tested in outdoor condition. The IS analysis is performed in 30 frequency points spanning in the range [5 Hz, 50 kHz]. The control unit detects the MPP (see Figure 5.14a) and then injects the perturbations with $A_I = 0.1A$ at various frequencies f_S. Figure 5.14b shows the current perturbation injected into the PV module and the corresponding voltage response at $f_S = 1kHz$. To validate the implemented control strategies, the performance metrics defined in Equation (5.37) are calculated considering the experimental waveforms. The following results have been obtained: $TA_{DC} = 99.18\%$ and $TA_{AC} = 93.54\%$, thereby confirming

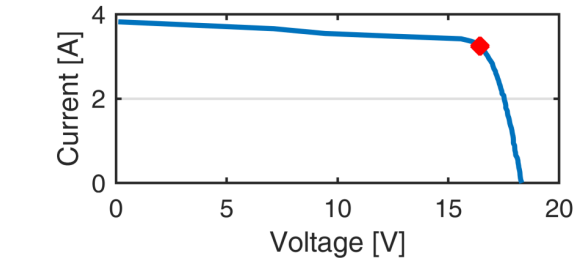

(a)

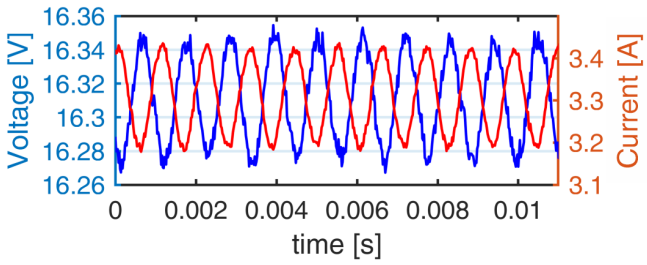

(b)

Figure 5.14. **(a)** I-V curve of the tested PV module and DC operating point corresponding to the MPP where the impedance spectrum is measured (red squared marker). **(b)** Measured voltage (in blue) and current waveforms (in red) at $f_S = 1$ kHz. Reproduced from my own work [10].

the simulative results presented in the previous section. The resulting PV impedance is marked in blue in Figure 5.15. As can be seen, the measured impedance points are benchmarked against the modeled spectrum of the PV module (depicted in red in Figure 5.15) obtained through the equivalent electric model proposed in Chapter 3. The extracted dynamic parameters for the tested module are summarized in Table 5.4. With respect to the reference, the measured PV spectrum exhibits an additional arc at high frequencies due to the parasitic effect of the setup cables and connectors. The experimental results demonstrate that the proposed approach exhibits an error in estimating the spectrum of, respectively, 1.26% for the real part of the impedance and less than 1% for the imaginary part. It is worth mentioning that the impedance spectrum shown in Figure 5.15 has been computed off-chip by implementing Equation 5.6 in a Matlab script. The voltage and current waveform parameters, namely A_V, A_I and γ, are estimated using the three-parameter sine fit algorithm [146].

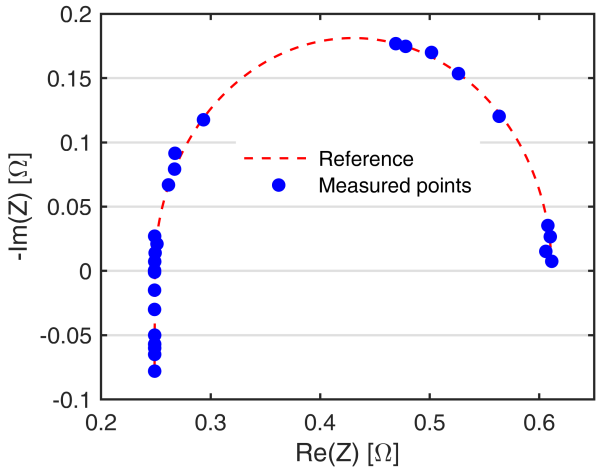

Figure 5.15. Nyquist spectrum measured by the proposed switch-mode impedance analyzer through on-field experiments.

Table 5.4. Extracted impedance parameters using the dynamic model defined in Equation (3.26).

Parameter	Value
Series Resistance R_S	0.2488 Ω
Parallel Resistance R_P	0.3624 Ω
Parallel Capacitance C_D	0.0054 F
Series Inductance L	0.12 μ H

5.7 Challenges and future directions

The development of the proposed switched-mode impedance analyzer represents an ongoing research activity that has already yielded encouraging preliminary results. The experiments carried out so far confirm the validity of the proposed methodology and its potential for on-field impedance characterization of photovoltaic modules. Nevertheless, several aspects still require further investigation and refinement to achieve a fully validated and optimized system. An essential step concerns the benchmarking of the proposed impedance analyzer against a calibrated laboratory-grade instrument, in order to quantitatively assess its accuracy and repeatability over a wide range of operating conditions, followed by an extensive experimental campaign on degraded modules aimed at validating the proposed instrument as an effective diagnostic tool. From a control perspective, the current control loop can be further enhanced by implementing separate control strategy for the DC and AC components of the reference current. In particular, the adoption of a Proportional–Resonant (PR) controller for the AC component tracking is expected to improve the overall system dynamic response and tracking accuracy of the AC component of the reference current [147]. The proposed control algorithm is based on single-sine injection, *i.e.*, one sinusoidal perturbation at a time. While this approach simplifies signal generation and analysis, it introduces some limitations. As discussed, the standards require measurement time windows lower than 1 s [103]. Consequently, the minimum excitation frequency cannot be chosen lower than 1 Hz. Moreover, the global duration of the measurement results in an inherent upper limit defined by the number of

frequency points. To tackle these issues, future work will explore alternative excitation strategies, such as multi-harmonic wave [148], white noise [149] and pseudo-Random Binary Sequence excitation algorithm [150]. In parallel, a second hardware revision of the converter is planned to improve the PCB layout, with the goal of minimizing parasitic effects and enhancing electromagnetic compatibility. This optimization is expected to significantly improve signal integrity, especially at higher frequencies.

5.8 Conclusions

In this chapter, a novel DC-DC converter design for on-field impedance spectroscopy on individual PV modules is proposed. The converter is realized as a synchronous Ćuk converter in GaN technology to achieve a high switching frequency of 500 kHz. The converter is designed according to the ratings of a standard Si-based PV module and it is capable of biasing the PV module in its MPP and injecting small AC current perturbations of frequency up to 50 kHz. To ensure safe and stable operation, the converter is provided with a bank of supercapacitors for absorbing the energy produced during the measurement. The system dynamics is modelled according to a specific discrete-time representation aiming to reduce the simulation time of less than 1 s. A closed-loop control strategy based on a PI controller has been specifically developed to guarantee the required bandwidth and tracking accuracy. This control algorithm dynamically identifies the MPP and automatically initiates the IS procedure. The proposed converter has been experimentally validated through IS measurements performed on a PV module operating under real outdoor conditions. Preliminary results confirm the high accuracy and reliability of the system: the converter achieves an AC injection tracking accuracy greater than 93%, with a measurement error below 2% across the investigated frequency range. The preliminary results highlight the potential of this approach to bridge the gap between laboratory-based impedance analysis and practical field applications.

Chapter 6

Conclusions

This dissertation addresses the challenge of developing portable, cost-effective and non-intrusive monitoring approaches for PV modules, focusing on both hardware design and electric modeling.

The first part of the thesis establishes the state of the art in PV monitoring techniques, analyzing both imaging and electric methods. Imaging approaches, such as visual inspection and IRT, allow rapid fault localization without interrupting plant operation, but they are unable to quantify energy losses or identify degradation mechanisms. Conversely, electric methods, such as IVT and IS, offer deeper diagnostic insight and allow to quantify energy losses, although the fault can only be localized when the method is applied at module level. This approach, however, becomes impracticable and expensive in large PV installation, where the number of modules are thousands. To address this trade-off, a hybrid monitoring strategy is proposed, combining UAV-based imaging inspection for large-scale fault detection and localization with module-level electrical inspection for performing the remaining steps of the diagnosis, namely fault classification and energy loss quantification. In this approach, the faulty module must be equipped with a portable instrument capable of performing either IVT or IS measurements while ensuring the normal operation of the string. However, the literature suggests that existing solutions suffer from several limitations, making them unsuitable for on-field and on-line monitoring. The outcome of analysis presented in Chapter 2 represents the foundation of this work, which proposes the design and realization of innovative hard-

ware platforms enabling on-field and on-line electric monitoring through IVT and IS measurements.

The dissertation introduces and validates two main modeling tools for the electrical characterization of PV modules in Chapter 3. The first is an enhanced circuit-based tool comprising a DC model for reproducing the I–V curves under various operating conditions. Beyond diagnostic purposes, the proposed tool aims to predict the energy yield of bifacial PV installations thanks to a detailed 3D cell-level numerical irradiance model. The proposed model accounts for the albedo-induced nonuniformities on the rear surface, a phenomenon often neglected by conventional view-factor-based methods. Simulation results demonstrate that neglecting these effects can lead to an overestimation of the energy yield by up to 8% under high-albedo conditions, particularly in the summer months. The proposed model is experimentally validated, confirming its ability to provide realistic energy yield estimations and highlighting its potential for both diagnostic and predictive applications.

Complementing the DC analysis, an AC model was developed to describe the frequency-domain behavior of c–Si PV modules. The dynamic model, derived from the SDM and supported by TCAD simulations, is used to analyze impedance spectra and extract key parameters associated with different degradation mechanisms. The simulative analysis identifies the MPP as the most suitable OP for IS measurements. Experiments conducted on-field using laboratory-grade impedance analyzer confirmed that the dynamic response of the module can be accurately represented by a double RC-loop equivalent circuit, providing a strong foundation for IS-based diagnostics.

The second major contribution of this research lies in the design and realization of two innovative hardware platforms enabling on-field electrical monitoring. The first is an I–V tracer based on Darlington transistors, specifically designed to perform on-line measurements, *i.e.*, the IVT is conducted during the normal PV operation. By integrating a novel disconnecting circuit, the system maintains current flow through the string while tracing the I–V curve, thus avoiding the need for plant shutdown. The prototype also incorporates wireless communication capabilities for flexible and low-power data acquisition. Experimental campaigns conducted at the University of Naples Federico II and the University of York demon-

strate that the tracer achieves a relative standard deviation below 10%, performs measurements in less than 1 s (fulfilling the requirements set by the standard [103]), and outperforms commercial instruments such as the Seaward PV200 in terms of accuracy and resolution. The results of this analysis are presented in Chapter 4.

The second hardware platform developed in this work is a DC–DC converter for on-field IS measurements, implemented as a synchronous Ćuk converter using GaN technology. Operating at a switching frequency of 500 kHz, the converter is capable of biasing the module at its MPP and injecting controlled AC perturbations up to 50 kHz. The system integrates a bank of supercapacitors for energy buffering and employs a closed-loop PI control loop strategy for high-precision tracking and stability. Experimental validation under real outdoor conditions demonstrates an AC tracking accuracy above 93% and a measurement error below 2%, confirming the feasibility of performing IS directly on PV modules mounted on-field. The work presented in Chapter 5 represents a significant step toward bridging the gap between laboratory-based IS and field-deployable diagnostic solutions.

Overall, the work presented in this dissertation contributes to advancing the state of the art in PV diagnostics by demonstrating that accurate and cost-effective module-level monitoring can be achieved under real operating conditions. The integration of advanced modeling and embedded hardware enables a new generation of smart diagnostic tools, capable of supporting predictive maintenance, improving reliability, and extending the lifetime of PV systems.

Bibliography

[1] M. De Riso, S. Hassan, P. Guerriero, M. Dhimish, and S. Daliento. "Enhanced Photovoltaic Panel Diagnostics: Advancing a High-Precision and Low-Cost I–V Curve Tracer". *IEEE Transactions on Instrumentation and Measurement*, 73:1–10, October 2024. Art. no. 9006110.

[2] K. Anderson, C. Hansen, W. Holmgren, A. Jensen, M. Mikofski, and A. Driesse. "pvlib python: 2023 project update". *Journal of Open Source Software*, 8(92):5994, 2023.

[3] V. d'Alessandro, S. Daliento, M. Dhimish, and P. Guerriero. "Albedo reflection modeling in bifacial photovoltaic modules". *Solar*, 4(4):660–673, 2024.

[4] V. d'Alessandro, S. Daliento, M. Dhimish, and P. Guerriero. "A tool for a fast and accurate evaluation of the energy production of bifacial photovoltaic modules". *Solar*, 5(1):2, 2025.

[5] M. De Riso, I. Matacena, S. Daliento, and P. Guerriero. "Impedance Spectroscopy as On-Field Monitoring Technique for PV Modules". In *2024 19th Conference on Ph.D Research in Microelectronics and Electronics (PRIME)*, pages 1–4, Larnaca, Cyprus, 2024.

[6] M. De Riso, P. Guerriero, I. Matacena, and S. Daliento. "A Tool Providing I-V Curve and IS Analysis of a PV Module Embedded in a String". In *2023 8th International Conference on Smart and Sustainable Technologies (SpliTech)*, pages 1–6, Split/Bol, Croatia, 2023.

[7] M. De Riso, I. Matacena, P. Guerriero, S. Daliento, L. E. Garcia Marrero, and G. Petrone. "Dynamic Modeling of Si-based Photovoltaic Modules using Impedance Spectroscopy Technique". In *2023 International Conference on Clean Electrical Power (ICCEP)*, pages 430–435, Terrasini, Italy, 2023.

[8] M. De Riso, M. Dhimish, P. Guerriero, and S. Daliento. "Design of a Portable Low-Cost I-V Curve Tracer for On-Line and In Situ Inspection of PV Modules". *Micromachines*, 15(7):896, July 2024.

[9] M. De Riso, I. Matacena, P. Guerriero, and S. Daliento. "A Wireless Self-Powered I-V Curve Tracer for On-Line Characterization of Individual PV Panels". *IEEE Transactions on Industrial Electronics*, 71(9):11508–11518, September 2024.

[10] L. Celentano, M. De Riso, R. Di Palo, M. Coppola, P. Guerriero, and S. Daliento. "A New Modelling Approach for a Cuk Converter for On-Field Diagnostics of PV Modules". In *2024 International Symposium on Power Electronics, Electrical Drives, Automation and Motion (SPEEDAM)*, pages 1236–1241, Napoli, Italy, 2024.

[11] M. De Riso, G. Saggese, P. Guerriero, and S. Daliento. "A Novel DC-DC Converter Design for On-Field Impedance Spectroscopy on Individual Photovoltaic Modules". In *2025 IEEE 53rd Photovoltaic Specialists Conference (PVSC)*, pages 1501–1503, Montreal, Canada, 2025.

[12] European Commission. "EU Solar Energy Strategy". Brussels, 18 May 2022, 2022. Available at: https://eur-lex.europa.eu.

[13] D. C. Jordan, K. Anderson, K. Perry, M. Muller, M. Deceglie, R. White, and C. Deline. "Photovoltaic fleet degradation insights". *Progress in Photovoltaics: Research and Applications"*.

[14] A. Bouraoui et al. "Experimental investigation of observed defects in crystalline silicon PV modules under outdoor hot dry climatic conditions in Algeria". *Solar Energy*, 159:475–487, 2018.

[15] A. El Hammoumi, S. Motahhir, A. Chalh, et al. "Low-cost virtual instrumentation of PV panel characteristics using Excel and Arduino in comparison with traditional instrumentation". *Renewables*, 5(3), 2018.

[16] R. Anand, R. K. Pachauri, A. Gupta, and Y. K. Chauhan. "Design and analysis of a low cost PV analyzer using Arduino UNO". In *2016 IEEE 1st International Conference on Power Electronics, Intelligent Control and Energy Systems (ICPEICES)*, pages 1–4, Delhi, India, 2016.

[17] V. Gupta, M. Sharma, R. K. Pachauri, and K. N. D. Babu. "A Low-Cost Real-Time IoT Enabled Data Acquisition System for Monitoring of PV System". *Energy Sources, Part A: Recovery, Utilization, and Environmental Effects*, 43(20):2529–2543, 2020.

[18] A. Rivai and N. A. Rahim. "A low-cost photovoltaic (PV) array monitoring system". In *2013 IEEE Conference on Clean Energy and Technology (CEAT)*, pages 169–174, Langkawi, Malaysia, 2013.

[19] U. A. Yusufoglu, T. H. Lee, T. M. Pletzer, A. Halm, L. J. Koduvelikulathu, C. Comparotto, et al. "Simulation of energy production by bifacial modules with revision of ground reflection". In *Energy Procedia*, volume 55, pages 389–395, 2014.

[20] W. Gu, T. Ma, M. Li, L. Shen, and Y. Zhang. "A coupled optical-electrical-thermal model of the bifacial photovoltaic module". *Applied Energy*, 258:114075, 2020.

[21] C. Deline, S. Ayala Pelaez, S. MacAlpine, and C. Olalla. "Estimating and parameterizing mismatch power loss in bifacial photovoltaic systems". *Progress in Photovoltaics: Research and Applications*, 28(7):691–703, 2020.

[22] N. Katayama, S. Osawa, S. Matsumoto, T. Nakano, and M. Sugiyama. "Degradation and fault diagnosis of photovoltaic cells using impedance spectroscopy". *Solar Energy Materials and Solar Cells*, 194:130–136, 2019.

[23] M. Liu, L. Wang, X. Cao, W. Zhang, Y. Yang, Y. Yan, and Z. Zhang. "Diagnosis of faults in photovoltaic modules via full-bias EIS scanning and dynamic parameter analysis". *Solar Energy Materials and Solar Cells*, 290:113731, 2025.

[24] S. Iqbal, S. M. Hasan, Y. Ayaz, E. U. Din, A. Waqas, and M. Sajid. "Condition Monitoring of Photovoltaic Panels through Electrical Impedance Spectroscopy and Machine Learning Focusing on Temperature, Dust and Microcracks". *IEEE Access*, Mar 2025.

[25] B. Taghezouit, F. Harrou, Y. Sun, and W. Merrouche. "Model-based fault detection in photovoltaic systems: A comprehensive review and avenues for enhancement". *Results in Engineering*, 21:101835, 2024.

[26] T. Niewelt, J. Schön, W. Warta, S. W. Glunz, and M. C. Schubert. "Degradation of Crystalline Silicon Due to Boron–Oxygen Defects". *IEEE Journal of Photovoltaics*, 7(1):383–398, 2017.

[27] M. Köntges et al. "Review of failures of photovoltaic modules". pages 1–140, 2014.

[28] D. DeGraaff, R. Lacerda, and Z. Campeau. "Degradation mechanisms in Si module technologies observed in the field; their analysis and statistics". *REL 2011 Photovoltaic Module Reliability Workshop*, 20:517–522, 2011.

[29] S. Spataru, P. Hacke, and D. Sera. "Automatic Detection of Inactive Solar Cell Cracks in Electroluminescence Images". In *Proceedings of the 2017 IEEE 44th Photovoltaic Specialist Conference (PVSC)*, 2017.

[30] Y.-Y. Hong and R. A. Pula. "Methods of photovoltaic fault detection and classification: A review". *Energy Reports*, 8:5898–5929, 2022.

[31] I. Polymeropoulos, S. Bezyrgiannidis, E. Vrochidou, and G. A. Papakostas. "Enhancing Solar Plant Efficiency: A Review of Vision-Based Monitoring and Fault Detection Techniques". *Technologies*, 12(10):175, 2024.

[32] M. Primorac H. Glavaš, M. Vukobratović and D. Muštran. "Infrared thermography in inspection of photovoltaic panels". In *2017 International Conference on Smart Systems and Technologies (SST)*, pages 63–68, 2017.

[33] S. Daliento, A. Chouder, P. Guerriero, A. Massi Pavan, A. Mellit, R. Moeini, and P. Tricoli. "Monitoring, Diagnosis, and Power Forecasting for Photovoltaic Fields: A Review". *International Journal of Photoenergy*, (1356851), 2017.

[34] N. Muhammad, N.Z. Zakaria, S. Shaari, and A.M. Omar. "System Performance and Detectable Faults of a 10-Year Old 1.1 kWp GCPV System in Malaysia". *Science Letters (ScL)*, 11(1):10–17, 2017.

[35] International Electrotechnical Commission. "IEC 61215: Crystalline silicon terrestrial photovoltaic (PV) modules – Design qualification and type approval, 2nd Edition", 2005. Edition 2.0, April 2005.

[36] International Electrotechnical Commission. "IEC 61646: Thin-film terrestrial photovoltaic (PV) modules – Design qualification and type approval, 2nd Edition", 2008. Edition 2.0, May 2008.

[37] Y. Zefri, A. El Kettani, I. Sebari, and S. Ait Lamallam. "Thermal Infrared and Visual Inspection of Photovoltaic Installations by UAV Photogrammetry—Application Case: Morocco". *Drones*, 2(4):41, 2018.

[38] L. Morando, C.T. Recchiuto, J. Calla, P. Scuteri, and A. Sgorbissa. "Thermal and Visual Tracking of Photovoltaic Plants for Autonomous UAV Inspection". *Drones*, 6(11):347, 2022.

[39] M. Alsafasfeh, I. Abdel-Qader, B. Bazuin, Q. Alsafasfeh, and W. Su. "Unsupervised Fault Detection and Analysis for Large Photovoltaic Systems Using Drones and Machine Vision". *Energies*, 11(9):2252, 2018.

[40] A. P. Catalano et al. "Using EMPHASIS for the Thermography-Based Fault Detection in Photovoltaic Plants". *Energies*, 14(6):1559, 2021.

[41] Inc. FLIR Systems. "FLIR E96 Advanced Thermal Imaging Camera". Technical Report Publ. No. 90202-0101 / 90203-0101, Teledyne FLIR, 2020.

[42] C. Henry, S. Poudel, S.-W. Lee, and H. Jeong. "Automatic Detection System of Deteriorated PV Modules Using Drone with Thermal Camera". *Applied Sciences*, 10(11):3802, 2020.

[43] M. Cubukcu and A. Akanalci. "Real-time Inspection and Determination Methods of Faults on Photovoltaic Power Systems by Thermal Imaging in Turkey". *Renewable Energy*, 147:1231–1238, 2020. Part 1.

[44] A. Sohani et al. "An In-depth Thermo-Electrical Evaluation of a Rooftop PV Technology for a Residential Building Using Advanced Infrared Thermography". *Engineering Analysis with Boundary Elements*, 152:243–258, 2023.

[45] K. Choi and J. Suh. "Fault Detection and Power Loss Assessment for Rooftop Photovoltaics Installed in a University Campus, by Use of UAV-Based Infrared Thermography". *Energies*, 16(11):4513, 2023.

[46] M. Dhimish, V. d'Alessandro, and S. Daliento. "Investigating the Impact of Cracks on Solar Cells Performance: Analysis Based on Nonuniform and Uniform Crack Distributions". *IEEE Transactions on Industrial Informatics*, 18(3):1684–1693, March 2022.

[47] K. G. Bedrich et al. "Quantitative Electroluminescence Imaging Analysis for Performance Estimation of PID-Influenced PV Modules". *IEEE Journal of Photovoltaics*, 8(5):1281–1288, September 2018.

[48] L. Stoicescu, M. Reuter, and J. Werner. "DaySy: Luminescence Imaging of PV Modules in Daylight". In *Proceedings of the 29th European Photovoltaic Solar Energy Conference and Exhibition (EU PVSEC)*, pages 2553–2554, 2014.

[49] G. Alves dos Reis Benatto et al. "Drone-Based Daylight Electroluminescence Imaging of PV Modules". *IEEE Journal of Photovoltaics*, 10(3):872–877, May 2020.

[50] International Electrotechnical Commission (IEC). "Photovoltaic System Performance—Part 3: Energy Evaluation Method". IEC TS 61724-3, Edition 1.0, July 2016.

[51] M. Dhimish and V. Holmes. "Fault Detection Algorithm for Grid-Connected Photovoltaic Plants". *Solar Energy*, 137:236–245, 2016.

[52] S. Silvestre, A. Chouder, and E. Karatepe. "Automatic Fault Detection in Grid Connected PV Systems". *Solar Energy*, 94:119–127, 2013.

[53] L. Chen and X. Wang. "Adaptive Fault Localization in Photovoltaic Systems". *IEEE Transactions on Smart Grid*, 9(6):6752–6763, November 2018.

[54] P. Guerriero, F. Di Napoli, and S. Daliento. "Real-Time Monitoring of Solar Fields with Cost/Revenue Analysis of Fault Fixing". In *2016 IEEE 16th International Conference on Environment and Electrical Engineering (EEEIC)*, pages 1–6, Florence, Italy, 2016.

[55] P. Guerriero, F. Di Napoli, G. Vallone, V. d'Alessandro, and S. Daliento. "Monitoring and Diagnostics of PV Plants by a Wireless Self-Powered Sensor for Individual Panels". *IEEE Journal of Photovoltaics*, 6(1):286–294, January 2016.

[56] M. Gargiulo, P. Guerriero, S. Daliento, A. Irace, V. d'Alessandro, M. Crisci, A. Smarrelli, and M. Smarrelli. "A Novel Wireless Self-Powered Microcontroller-Based Monitoring Circuit for Photovoltaic Panels in Grid-Connected Systems". In *Proceedings of the 2010 International Symposium on Power Electronics, Electrical Drives, Automation and Motion (SPEEDAM '10)*, pages 164–168, Pisa, Italy, June 2010.

[57] International Electrotechnical Commission (IEC), Geneva, Switzerland. *"IEC 60904-9:2020 Photovoltaic devices – Part 9: Classification of solar simulator characteristics"*, 2020. Edition 3.0.

[58] International Electrotechnical Commission (IEC), Geneva, Switzerland. *"IEC 60891:2021 Photovoltaic devices – Procedures for temperature and irradiance corrections to measured I–V characteristics"*, 2021. Edition 3.0.

[59] S. Spataru, D. Sera, T. Kerekes, and R. Teodorescu. "Diagnostic method for photovoltaic systems based on light I–V measurements". *Solar Energy*, 119:29–44, 2015.

[60] X. Zhang, Y. Ma, H. Ma, L. Zhang, and T. Whang. "A data-driven photovoltaic string current mismatch fault diagnosis method based on I–V curve". *Microelectronics Reliability*, 138:114705, 2022.

[61] M. M. Badr, M. S. Hamad, A. S. Abdel-Khalik, R. A. Hamdy, S. Ahmed, and E. Hamdan. "Fault Identification of Photovoltaic Array Based on Machine Learning Classifiers". *IEEE Access*, 9:159113–159132, 2021.

[62] M. W. Hopwood, J. S. Stein, J. L. Braid, and H. P. Seigneur. "Physics-Based Method for Generating Fully Synthetic I–V Curve Training Datasets for Machine Learning Classification of PV Failures". *Energies*, 15(14):5085, 2022.

[63] K. Lappalainen, M. Piliougine, S. Valkealahti, and G. Spagnuolo. "Photovoltaic module series resistance identification at its maximum power production". *Mathematics and Computers in Simulation*, 224:50–62, 2024.

[64] S. Fadhel, C. Delpha, D. Diallo, I. Bahri, A. Migan, M. Trabelsi, and M. F. Mimouni. "PV shading fault detection and classification based on I–V curve using principal component analysis: Application to isolated PV system". *Solar Energy*, 179:1–10, 2019.

[65] C. Schill, A. Brachmann, and M. Koehl. "Impact of soiling on I–V curves and efficiency of PV modules". *Solar Energy*, 112:259–262, 2015.

[66] S. Osawa, T. Nakano, S. Matsumoto, N. Katayama, Y. Saka, and H. Sato. "Fault diagnosis of photovoltaic modules using AC impedance spectroscopy". In *2016 IEEE International Conference on Renewable Energy Research and Applications (ICRERA)*, pages 210–215, Birmingham, UK, 2016.

[67] T. Yeow, J. Sun, Z. Yao, J.-N. Jaubert, and K. P. Musselman. "Evaluation of impedance spectroscopy as a tool to characterize degradation mechanisms in silicon photovoltaics". *Solar Energy*, 184:52–58, 2019.

[68] A. El-Tayeb, F. Li, A. Kumar, and G. Tamizhmani. "Electrical Impedance Spectroscopy: A Complementary Approach Differentiating PID Mechanisms in Photovoltaics". *Electronics*, 14(5):1021, 2025.

[69] T. Finsterle, L. Černá, P. Hrzina, D. Rokusek, and V. Benda. "Diagnostics of PID Early Stage in PV Systems". *Energies*, 14(8):2155, 2021.

[70] M. I. Oprea et al. "Detection of potential induced degradation in c-Si PV panels using electrical impedance spectroscopy". In *2016 IEEE 43rd Photovoltaic Specialists Conference (PVSC)*, pages 1575–1579, Portland, OR, USA, 2016.

[71] R. A. Guejia-Burbano, G. Petrone, and M. Piliougine. "Impedance Spectroscopy for Diagnosis of Photovoltaic Modules Under Outdoor Conditions". *IEEE Journal of Photovoltaics*, 12(6):1503–1512, 2022.

[72] A. C. Lazaroiu, M. Gmal Osman, C. V. Strejoiu, and G. Lazaroiu. "A Comprehensive Overview of Photovoltaic Technologies and Their Efficiency for Climate Neutrality". *Sustainability*, 15(23):16297, Nov 2023.

[73] A. P. Dobos. "PVWatts Version 5 Manual". Technical Report NREL/TP-6A20-62641, National Renewable Energy Laboratory (NREL), Golden, CO, USA, 2014.

[74] David L. King, Jay A. Kratochvil, and William E. Boyson. "Photovoltaic Array Performance Model". Technical report, United States Department of Energy, Albuquerque, NM, USA, 2004.

[75] M. J. Heredia-Rios, L. Hernandez-Martinez, M. Linares-Aranda, M. Moreno-Moreno, and J. F. Méndez. "Analysis of Losses Associated with Series Resistance (Rs) in Simple-Structured c-Si Solar Cells". *Energies*, 17(7):1520, 2024.

[76] D. S. H. Chan and J. C. H. Phang. "Analytical Methods for the Extraction of Solar-Cell Single and Double Diode Model Parameters from I–V Characteristics". *IEEE Transactions on Electron Devices*, 34(2):286–293, Feb 1987.

[77] M. H. Qais, H. M. Hasanien, S. Alghuwainem, K. H. Loo, M. A. Elgendy, and R. A. Turky. "Accurate Three-Diode Model Estimation of Photovoltaic Modules Using a Novel Circle Search Algorithm". *Ain Shams Engineering Journal*, 13(3):101824, 2022.

[78] E. I. Batzelis. "Non-Iterative Methods for the Extraction of the Single-Diode Model Parameters of Photovoltaic Modules: A Review and Comparative Assessment". *Energies*, 12(3):358, 2019.

[79] B. Durusoy, T. Ozden, and B. G. Akinoglu. "Solar irradiation on the rear surface of bifacial solar modules: a modeling approach". *Scientific Reports*, 10:13300, 2020.

[80] M. Ernst, X. Liu, C.-A. Asselineau, D. Chen, C. Huang, and A. Lennon. "Accurate modelling of the bifacial gain potential of rooftop solar photovoltaic systems". *Energy Conversion and Management*, 300:117947, 2024.

[81] K. R. McIntosh, M. D. Abbott, B. A. Sudbury, and J. Meydbray. "Mismatch loss in bifacial modules due to nonuniform illumination in 1-D tracking systems". *IEEE Journal of Photovoltaics*, 9(6):1504–1512, 2019.

[82] S. Tsuchida, Y. Tsuno, D. Sato, T. Oozeki, and N. Yamada. "Albedo-dependent bifacial gain losses in photovoltaic modules with rear-side support structures". *IEEE Journal of Photovoltaics*, 13(6):938–944, 2023.

[83] The MathWorks Inc. "MATLAB version: 9.13.0 (R2022b)", 2022.

[84] Analog Devices, Inc., Norwood, MA, USA. *"LTspice XVII—SPICE Simulation Software"*, 2017. Available at: https://www.analog.com/ltspice.

[85] PVGIS. "PVGIS, online tool". https://joint-research-centre.ec.europa.eu/, 2025.

[86] B. Y. H. Liu and R. C. Jordan. "A rational procedure for predicting the long-term average performance of flat-plate solar-energy collectors – With design data for the U.S., its outlying possessions and Canada". *Solar Energy*, 7(2):53–74, Apr.-Jun. 1963.

[87] Suntech Power. "STP430S-C54/Nmhm+ Datasheet". https://www.suntech-power.com. Accessed: Oct. 2025.

[88] J. Appelbaum. "Bifacial photovoltaic modules field". *Renewable Energy*, 85:338–343, 2016.

[89] M. A. Anoma, D. Jacob, B. C. Bourne, J. A. Scholl, D. M. Riley, and C. W. Hansen. "View factor model and validation for bifacial PV and diffuse shade on single-axis trackers". In *Proceedings of the IEEE 44th Photovoltaic Specialist Conference (PVSC)*, Washington, DC, USA, 2017.

[90] S. Daliento, M. De Riso, P. Guerriero, I. Matacena, M. Dhimish, and V. d'Alessandro".

[91] ET-Solar. "ET-M54050 Datasheet". https://www.etsolar.com. Accessed: 2025-10-15.

[92] V. d'Alessandro, P. Guerriero, S. Daliento, and M. Gargiulo. "A straightforward method to extract the shunt resistance of photovoltaic cells from current–voltage characteristics of mounted arrays". *Solid-State Electronics*, 63(1):130–136, Sep 2011.

[93] J. Panigrahi, Vandana, R. Singh, N. Batra, J. Gope, M. Sharma, P. Pathi, S. Srivastava, C. Rauthan, and P. Singh. "Impedance spectroscopy of crystalline silicon solar cell: Observation of negative capacitance". *Solar Energy*, 136:412–420, 2016.

[94] M. A. Varnosfaderani and D. Strickland. "Online Electrochemical Impedance Spectroscopy (EIS) estimation of a solar panel". *Vacuum*, 139:185–195, 2017.

[95] O. I. Olayiwola and P. S. Barendse. "Photovoltaic Cell/Module Equivalent Electric Circuit Modeling Using Impedance Spectroscopy". *IEEE Transactions on Industry Applications*, 56(2):1690–1701, 2020.

[96] J. Bisquert. "Theory of the impedance of electron diffusion and recombination in a thin layer". *The Journal of Physical Chemistry B*, 106(2):325–333, 2002.

[97] I. Mora-Sero et al. "Impedance spectroscopy characterisation of highly efficient silicon solar cells under different light illumination intensities". *Energy & Environmental Science*, 2(6):678–686, 2009.

[98] Synopsys Inc., Mountain View, CA, USA. *"Sentaurus Device User Guide, Release K-2015.06"*, 2015.

[99] O. Breitenstein, J.P. Rakotoniaina, M.H. Al Rifai, and M. Werner. "Shunt types in crystalline silicon solar cells". *Progress in Photovoltaics: Research and Applications*, 12(7):529–538, 2004.

[100] Solbian. "SP Series Solar Panel, FLEXSP50L Datasheet". https://www.solbian.eu. Accessed: 2025-10-16.

[101] L. E. Garcia-Marrero, M. Piliougine, G. Petrone, M. De Riso, P. Guerriero, and E. Monmasson. "Challenges in Photovoltaic Parameter Identification under Mismatching Conditions". In *2023 International Conference on Clean Electrical Power (ICCEP)*, pages 436–444, Terrasini, Italy, 2023.

[102] Q. Gao et al. "Effects of I–V Measurement Parameters on the Hysteresis Effect and Optimization in High-Capacitance PV Module Testing". *IEEE Journal of Photovoltaics*, 8(3):710–718, May 2018.

[103] "Photovoltaic Devices - Part 1: Measurement Of Photovoltaic Current-Voltage Characteristics". Technical report, International Electrotechnical Commission, 2006.

[104] E. E. van Dyk et al. "Monitoring current–voltage characteristics and energy output of silicon photovoltaic modules". *Renewable Energy*, 30(3):399–411, March 2005.

[105] H. Amiry et al. "Design and implementation of a photovoltaic IV curve tracer: Solar modules characterization under real operating conditions". *Energy Conversion and Management*, 169:206–216, August 2018.

[106] A. A. Willoughby et al. "A simple resistive load I-V curve tracer for monitoring photovoltaic module characteristics". In *2014 5th International Renewable Energy Congress (IREC)*, pages 1–6, March 25–27 2014.

[107] F. Spertino, A. Ciocia, P. Di Leo, A. Massi Pavan, D. Rosato, and F. Vergura. "Capacitor charging method for I–V curve tracer and MPPT in photovoltaic systems". *Solar Energy*, 119:461–473, 2015.

[108] M. Cáceres, J. M. Blanes, F. P. Blanes, and J. A. Carrasco. "Low-cost I–V tracer for PV modules under real operating conditions". *Energies*, 13(17):4320, 2020.

[109] J. Sayyad and P. Nasikkar. "Design and development of low cost, portable, on-field IV curve tracer based on capacitor loading for high power rated solar photovoltaic modules". *IEEE Access*, 9:70715–70731, 2021.

[110] A. V. Joglekar and B. Hegde. "Online IV Tracer for per string monitoring and maintenance of PV panels". In *Proceedings of the IECON 2018 – 44th Annual Conference of the IEEE Industrial Electronics Society*, pages 1890–1894, 2018.

[111] Inc. Daystar. "DS-100C I–V Curve Tracer". http://www.daystarpv.com. Accessed: 2025-10-14.

[112] Seaward Electronic Ltd. "PV200 Solar Module Tester". https://www.seaward.com/gb/products/solar-testing/pv200/. Accessed: 2025-10-14.

[113] K. K. Tse, M. T. Ho, H. S. H. Chung, and S. Y. R. Hui. "A comparative study of maximum-power-point trackers for photovoltaic panels using switching-frequency modulation scheme". *IEEE Transactions on Industrial Electronics*, 51(2):410–418, 2004.

[114] T. Khatib, A. Mohamed, and K. Sopian. "Simplified IV characteristic tester for photovoltaic modules using a DC-DC boost converter". *Sustainability*, 9(4):657, 2017.

[115] E. Durán, J. Galán, M. Sidrach de Cardona, and J. M. Andújar. "Determination of PV generator IV/PV characteristic curves using a DC-DC converter controlled by a virtual instrument". *International Journal of Photoenergy*, 2012:1–9, 2012.

[116] T. A. Pereira, A. P. Grilo, D. S. Oliveira, and F. J. T. Filho. "Design of a Portable Photovoltaic I–V Curve Tracer Based on the DC–DC Converter Method". *IEEE Journal of Photovoltaics*, 11(2):552–560, 2021.

[117] S. Spataru, H. Sera, J. M. Guerrero, and R. Teodorescu. "Diagnostic method for photovoltaic systems based on light I–V measurements". *Solar Energy*, 119:29–44, 2015.

[118] S. Spataru, H. Sera, J. M. Guerrero, and R. Teodorescu. "Monitoring and fault detection in photovoltaic systems based on inverter measured string IV curves". In *Proceedings of the 31st European Photovoltaic Solar Energy Conference and Exhibition (EU PVSEC)*, pages 1667–1674. WIP Wirtschaft und Infrastruktur GmbH & Co Planungs KG, 2015.

[119] C. M. A. da Luz, R. B. Godoy, J. P. Bonaldo, and L. Michels. "Maximum power point tracking technique based on sweeping the characteristic curve of the photovoltaic module". *Sustainable Computing: Informatics and Systems*, 33:100638, 2022.

[120] S. Salima, M. Zegrar, A. Asbayou, H. Belmili, and F. Cheknane. "Implementation of a plug and play I-V curve tracer dedicated to characterization and diagnosis of PV modules under real operating conditions". *Energy Conversion and Management*, 209, 2020.

[121] Y. Kuai and S. Yuvarajan. "An electronic load for testing photovoltaic panels". *Journal of Power Sources*, 154(1):308–313, 2006.

[122] M. Zegrar, S. Salima, H. Belmili, and F. Cheknane. "Design and implementation of an IV curve tracer dedicated to characterize PV panels". *International Journal of Electrical and Computer Engineering*, 11(3):2011–2018, 2021.

[123] A. Asbayou, M. Zegrar, S. Salima, H. Belmili, and F. Cheknane. "Utilization of MOSFET transistor as an electronic load to trace IV and PV curve of a solar panel". In *E3S Web of Conferences*, volume 229, page 01021. EDP Sciences, 2021.

[124] A. Vega, R. Alonso, J. Marcos, and E. Lorenzo. "Double sweep tracer for IV curves characterization and continuous monitoring of photovoltaic facilities". *Solar Energy*, 190:622–629, 2019.

[125] Laird Connectivity. "BT740-SC Datasheet". Datasheet, July 2013, Rev. Aug. 2020, 2020. Accessed: 2025-10-14.

[126] D. Sera, T. Kerekes, R. Teodorescu, and F. Blaabjerg. "On the Perturb-and-Observe and Incremental Conductance MPPT Methods for PV Systems". *IEEE Journal of Photovoltaics*, 3(3):1070–1078, July 2013.

[127] H. S. Alpert et al. "Sensitivity of 2DEG-based Hall-effect sensors at high temperatures". *Review of Scientific Instruments*, 91(2):025003, Feb 2020.

[128] Mitsubishi Electric. "Mitsubishi 120-Watt Solar Panel, PV-MF120EC3, Datasheet", n.d. Accessed: 2025-10-17.

[129] V. D'Alessandro, F. Di Napoli, P. Guerriero, and S. Daliento. "An automated high-granularity tool for a fast evaluation of the yield of PV plants accounting for shading effects". *Renewable Energy*, 83:294–304, 2015.

[130] M. Louzazni and S. Al-Dahidi. "Approximation of photovoltaic characteristics curves using Bézier Curve". *Renewable Energy*, 174:715–732, 2021.

[131] N. Wang, F. Meng, L. Zhang, Z. Liu, and W. Liu. "Light soaking of hydrogenated amorphous silicon: A short review". *Carbon Neutrality*, 3:18, 2024.

[132] U. Troeltzsch and O. Kanoun. "Miniaturized impedance measurement system for battery diagnosis". In *Proceedings SENSOR 2009, Volume I*, pages 251–256, 2009.

[133] S. Peng, Q. Ling, M. Yang, C. Bao, X. Zhong, and P. Wang. "A High-Precision and Fast Measurement Method for Li-Ion Battery EIS". *IEEE Transactions on Instrumentation and Measurement*, 74:1–13, 2025.

[134] A. De Angelis, E. Buchicchio, F. Santoni, A. Moschitta, and P. Carbone. "Uncertainty Characterization of a Practical System for Broadband Measurement of Battery EIS". *IEEE Transactions on Instrumentation and Measurement*, 71:1–9, 2022.

[135] A. Ria, G. Manfredini, F. Gagliardi, M. Vitelli, P. Bruschi, and M. Piotto. "Online High-Resolution EIS of Lithium-Ion Batteries by Means of Compact and Low Power ASIC". *Batteries*, 9(5):239, 2023.

[136] P. Carbone, A. De Angelis, J. Schoukens, A. Moschitta, and F. Santoni. "Low-Complexity Electrochemical-Impedance Spectroscopy for Battery Monitoring". *IEEE Transactions on Instrumentation and Measurement*, 72:1–9, 2023.

[137] Analog Devices. *"AD5940: High Precision, Impedance and Electrochemical Front End, note = Datasheet available at: https://www.analog.com/en/products/ad5940.html"*, Accessed 2025.

[138] M. Abedi Varnosfaderani and D. Strickland. "A Comparison of Online Electrochemical Spectroscopy Impedance Estimation of Batteries". *IEEE Access*, 6:23668–23677, 2018.

[139] R. Koch, R. Kuhn, I. Zilberman, and A. Jossen. "Electrochemical impedance spectroscopy for online battery monitoring — power electronics control". In *16th European Conference on Power Electronics and Applications (EPE)*, pages 1–10, Lappeenranta, Finland, 2014.

[140] F. Díaz-González, D. Heredero-Peris, and S. Galceran-Arellano. "Design Methodology for a DC–DC Power Conversion System with EIS Capability for Battery Packs". *Unpublished manuscript or institutional report*, 2023. Serra Húnter Fellow.

[141] H. Huisman, M. Uchan, and G. Tibola. "Using an Interleaved Buck Converter for Battery-Pack Electrochemical Impedance Spectroscopy". In *2024 Energy Conversion Congress & Expo Europe (ECCE Europe)*, pages 1–6. IEEE, September 2024.

[142] O. I. Olayiwola and P. S. Barendse. "Power Electronic Implementation of Electrochemical Impedance Spectroscopy on Photovoltaic Modules". In *IEEE Energy Conversion Congress and Exposition (ECCE)*, pages 3654–3661, 2020.

[143] L. Shelembe and P. Barendse. "A Quantitative Feedback Theory Approach to Converter-Based Broadband Impedance Spectroscopy for Online Condition Monitoring of Photovoltaic Modules". In *IEEE Energy Conversion Congress and Exposition (ECCE)*, pages 451–458, Vancouver, BC, Canada, 2021.

[144] G. Gámez E, C. A. Palafox S., H. M. C., J. A. Beristáin J, and J. P. R. "Contribution to the Analysis and Design of the Cuk Converter for the Transfer of Photovoltaic Solar Energy to Batteries". In *2019 IEEE International Autumn Meeting on Power, Electronics and Computing (ROPEC)*, pages 1–6, Ixtapa, Mexico, 2019.

[145] Ling Yang and et al. "A double update PWM method to improve robustness for the deadbeat current controller in three-phase grid-connected system". *Journal of Electrical and Computer Engineering*, 2018:2972379, 2018.

[146] M. Martino, R. Losito, and A. Masi. "Analytical metrological characterization of the three-parameter sine fit algorithm". *ISA transactions*, 51(2):262–270, 2012.

[147] Xin Wang and et al. "Control strategies of converter-based online impedance spectroscopy for photovoltaic panels". *IEEE Transactions on Industry Applications*, 60(4):6524–6538, 2024.

[148] G. S. Popkirov and et al. "A new impedance spectrometer for the investigation of electrochemical systems". *Review of Scientific Instruments*, 63(11):5366–5372, November 1992.

[149] C. Gabrielli and et al. "Measurement time versus accuracy trade-off analyzed for electrochemical impedance measurements by means of sine, white noise and step signals". *Journal of Electroanalytical Chemistry and Interfacial Electrochemistry*, 138(1):201–208, August 1982.

[150] Edoardo Locorotondo and et al. "Development of a battery real-time state of health diagnosis based on fast impedance measurements". *Journal of Energy Storage*, 38:102566, 2021.

[151] S. Chattopadhyay, R. Dubey, S. Bhaduri, S. Zachariah, H. K. Singh, and C. S. Solanki. "Correlating Infrared Thermography With Electrical Degradation of PV Modules Inspected in All-India Survey of Photovoltaic Module Reliability 2016". *IEEE Journal of Photovoltaics*, 8(6):1800–1808, 2018.

[152] J. A. A. Qahouq and Z. Xia. "Single-Perturbation-Cycle Online Battery Impedance Spectrum Measurement Method With Closed-Loop Control of Power Converter". *IEEE Transactions on Industrial Electronics*, 64(9):7019–7029, 2017.

Author's Publications

Journal Papers

1.j M. De Riso, I. Matacena, P. Guerriero and S. Daliento, "A Wireless Self-Powered I-V Curve Tracer for On-Line Characterization of Individual PV Panels," *IEEE Transactions on Industrial Electronics*, vol. 71, no. 9, p. 11508-11518, Sep. 2024, doi: 10.1109/TIE.2023.3344843.

2.j M. De Riso, M. Dhimish, P. Guerriero and S. Daliento, "Design of a Portable Low-Cost I-V Curve Tracer for On-Line and In Situ Inspection of PV Modules," *Micromachines*, vol. 15, no. 7, p. 896, July 2024, doi: 10.3390/mi15070896.

3.j M. De Riso, S. Hassan, P. Guerriero, M. Dhimish and S. Daliento, "Enhanced Photovoltaic Panel Diagnostics: Advancing a High-Precision and Low-Cost I – V Curve Tracer," *IEEE Transactions on Instrumentation and Measurement*, vol. 73, Art no. 9006110, p. 1-10, Oct. 2024, doi: 10.1109/TIM.2024.3484517.

Conference Papers

1.c M. De Riso, I. Matacena, P. Guerriero, S. Daliento, L. E. Garcia Marrero and G. Petrone, "Dynamic Modeling of Si-based Photovoltaic Modules using Impedance Spectroscopy Technique," *2023 International Conference on Clean Electrical Power (ICCEP)*, Terrasini, Italy, 2023, pp. 430-435, doi: 10.1109/ICCEP57914.2023.10247369.

2.c L. E. Garcia-Marrero, M. Piliougine, G. Petrone, M. De Riso, P. Guerriero and E. Monmasson, "Challenges in photovoltaic parameter identifi-

cation under mismatching conditions," *2023 International Conference on Clean Electrical Power (ICCEP)*, Terrasini, Italy, 2023, pp. 436-444, doi: 10.1109/ICCEP57914.2023.10247445.

3.c M. De Riso, P. Guerriero, I. Matacena and S. Daliento, "A tool providing I-V curve and IS analysis of a PV module embedded in a string," *2023 8th International Conference on Smart and Sustainable Technologies (SpliTech)*, Split/Bol, Croatia, 2023, pp. 1-6, doi: 10.23919/SpliTech58164.2023.10193293.

4.c M. De Riso, I. Matacena, S. Daliento and P. Guerriero, "Impedance Spectroscopy as On-Field Monitoring Technique for PV Modules," *2024 19th Conference on Ph.D Research in Microelectronics and Electronics (PRIME)*, Larnaca, Cyprus, 2024, pp. 1-4, doi: 10.1109/PRIME61930.2024.10559699.

5.c L. Celentano, M. De Riso, R. Di Palo, M. Coppola, P. Guerriero and S. Daliento, "A new modelling approach for a Cuk converter for on-field diagnostics of PV modules," *2024 International Symposium on Power Electronics, Electrical Drives, Automation and Motion (SPEEDAM)*, Napoli, Italy, 2024, pp. 1236-1241, doi: 10.1109/SPEEDAM61530.2024.10609170.

6.c S. Daliento, M. De Riso, P. Guerriero, I. Matacena, M. Dhimish and V. d'Alessandro, "On the Optimal Orientation of Bifacial Solar Modules," *2024 International Symposium on Power Electronics, Electrical Drives, Automation and Motion (SPEEDAM)*, Napoli, Italy, 2024, pp. 396-400, doi: 10.1109/SPEEDAM61530.2024.10609062.

7.c M. De Riso, G. Saggese, P. Guerriero, S. Daliento, "A Novel DC-DC Converter Design for On-Field Impedance Spectroscopy on Individual Photovoltaic Modules," *2025 IEEE 53rd Photovoltaic Specialists Conference (PVSC)*, Montreal, Canada, 2025, pp. 1501-1503, doi: 10.1109/PVSC59419.2025.11132519.